Dissertation

Radiation Studies with FLUKA for the ATLAS detector

Ausgeführt zum Zweck der Erlangung des akademischen Grades eines Doktors der technischen Wissenschaften unter der Leitung von

Mika Huhtinen (CERN)
Albert Hirtl (TU Wien)

am
CERN - European Organisation for Nuclear Research
und dem Atominstitut der Technischen Universität Wien

eingereicht an der
Technischen Universität Wien
Fakultät für Physik

von:
Michael Bauer
Matrikelnummer: 01555320
Rue des Coulemelles 115
01710 Thoiry
France

Geneve, 1. Juli 2024

Unterschrift M. Bauer

Michael Bauer

Zusammenfassung

In dieser Arbeit wird eine umfassende Untersuchung der Strahlenabschirmung und von Strahlenschäden im ATLAS-Detektor am Large Hadron Collider (LHC) präsentiert. Die Forschung umfasst mehrere Aspekte, darunter die Implementierung einer räumlichen Binning-Technik in FLUKA für effektive Studien des Strahlungshintergrunds, die Erforschung unterschiedlicher Konfigurationen von Neutronenmoderatoren neben anderen Abschirmungskonzepten, sowie die Neubewertung der Gewichtungsfaktoren für negative Pionen basierend auf einem neuen Ansatz.

Die Implementierung einer räumlichen Binning-Technik in FLUKA ermöglicht die Einbindung von Simulationsergebnissen in interaktive Webseiten,wodurch eine effektive Darstellung von Materialzusammensetzung, relevanter Fluenzen und zeitabhängiger Spektren absorbierter Energiedosis innerhalb des Detektors ermöglicht wird.

Um die Abschirmung empfindlicher Detektorkomponenten zu optimieren, ergänzt ein einfaches Modell für effektive Moderatorstudien detaillierte Untersuchungen zum Strahlungstransport innerhalb der komplexen ATLAS-Geometrie. Die Neutronenproduktion im elektromagnetischen Kalorimeter wird untersucht, um einen Maßstab für die Effizienz des Moderators festzulegen. Simulationen mit unterschiedlichem Bor-Inhalt werden durchgeführt, um den Einfluss auf die thermische Neutronenfluenz zu bewerten. Potenzielle Wechselwirkungen zwischen verschiedenen Regionen des Detektors werden anhand einer Analyse des Neutronentransports untersucht. Es wird analysiert wie sich die Reduktion der Wasserstoffdichte in Moderatoren im Inneren Detektor auf die Neutronenfluenz auswirkt, sowie der Effekt des Wasserstoffverlustes aufgrund von Bor-Dotierung.

Ein wesentlicher Teil der Forschung konzentriert sich auf die Neubewertung der Gewichtungsfaktoren von Strahlenschäden negativer Pionen. Die Studie nutzt einen in der Literatur vorhandenen Formalismus, um diese Faktoren neu zu bewerten, was zu einem besseren Verständnis der Schadensmechanismen führt. Die neuen Gewichtungsfaktoren berücksichtigen den Beitrag von Teilchen, die innerhalb des Materials vollständig abgebremst werden, ein bis dato unberücksichtigter Aspekt. Basierend darauf ist ein langjähriges Mysterium der Diskrepanz zwischen Daten von Strahlungssensoren und Simulationsergebnissen im ATLAS-Detektor nun wesentlich besser verstanden.

Abstract

This work presents a comprehensive investigation of radiation shielding and radiation damage in the ATLAS detector at the Large Hadron Collider (LHC). The research covers several aspects, including the implementation of a spatial binning technique in FLUKA for effective studies of radiation background, the exploration of different configurations of neutron moderators alongside other shielding concepts, and the re-evaluation of weighting factors for negative pions based on a new approach.

The implemented spatial binning technique in FLUKA enables the integration of simulation results into interactive web pages, allowing for effective representation of material composition, relevant fluences, and time-dependent spectra of absorbed energy dose within the detector.

To optimise the shielding of sensitive detector components, a simple model for effective moderator studies complements detailed investigations of radiation transport within the complex ATLAS geometry. The neutron production in the electromagnetic calorimeter is studied to establish a benchmark for the moderator's efficiency. Simulations with varying boron content are conducted to evaluate the impact on thermal neutron fluence. Potential interactions between different regions of the detector are examined through an analysis of neutron transport. The effects of reducing hydrogen density of moderators in the Inner Detector on neutron fluence and the impact of hydrogen loss due to boron doping are analysed.

A significant part of the research focuses on re-evaluating the weighting factors of radiation damage from negative pions. The study utilises a formalism found in the literature to reassess these factors, leading to a better understanding of the damage mechanisms. The new weighting factors take into account the contribution of particles that are completely stopped within the material, an aspect previously neglected. Based on this, a long-standing mystery regarding the discrepancy between data from radiation sensors and simulation results in the ATLAS detector is now better understood.

Acknowledgements

First and foremost, I want to thank Mika Huhtinen for his proficient guidance, enduring patience, and encouraging feedback throughout my time at CERN.

Further, I want to thank Sven Menke for his technical assistance and valuable input.

Thanks to Ian Dawson, Robert Froeschl, and Vincent Hedberg for their support on various projects and for fostering scientific discussions at the Radiation Simulation Working Group meetings.

I am grateful to Albert Hirtl for his supervision and assistance with university matters, and for the trust and freedom he has given me in my research.

I want to express my appreciation to Andreas Salzburger and Armin Nairz for their confident and relaxed leadership and for the encouraging environment they have created within the team.

Finally, I thank Laura for her support beyond the scope of this thesis.

Contents

List of Abbreviations

HEP High Energy Physics

SM Standard Model

IP Interaction Point

Missing Transverse Energy MET

Level 1 L1

MPV Most Probable Value

ITk Inner Tracker of ATLAS' Phase 2 upgrade

LHC Large Hadron Collider

CERN European Organization for Nuclear Research

HL-LHC High Luminosity upgrade of the Large Hadron Collider

ID Inner Detector

IBL Insertable B-Layer

Pix Pixel Layer 1-3

SCT SemiConductor Tracker

TRT Transition Radiation Tracker

LS1 first long shutdown of the LHC

LS2 second long shutdown of the LHC

ECAL Electromagnetic Calorimeter

HCAL Hadronic Calorimeter

FCAL Forward Calorimeter

LAr Liquid Argon

MS Muon Spectrometer

DAQ Data Acquisition

RoI Region of Interest

HGTD High-Granularity Timing Detector

VAX Vacuum Assembly for eXperimental area

NIEL Non-Ionising Energy Loss

TID Total Ionising Dose

SEE Single Event Effect

SEU Single Event Upsets

SEL Single Event Latch-up

SEGR Single Event Gate Rupture

SEB Single Event Burnout

MOS Metal Oxide Semiconductor

CMOS Complementary Metal Oxide Semiconductor

LDMOS Laterally Diffused MOS

LET Linear Energy Transfer

1. Introduction

High-Energy Physics (HEP), with its quest to understand the fundamental constituents of matter, relies heavily on sophisticated detectors to observe and measure particle interactions. The ATLAS experiment [1] at the Large Hadron Collider (LHC) [2], plays a pivotal role in these investigations. Notably, ATLAS played a key role in the 2012 discovery of the Higgs boson, providing crucial data that confirmed the particle's existence [3].

With particles colliding at nearly the speed of light at a rate of 10^9 collisions per second in the LHC, these interactions produce a significant radiation background. This presents major challenges for detector components, especially silicon sensors. This thesis addresses two critical aspects of maintaining and enhancing the performance of the ATLAS detector: effective radiation shielding and the accurate assessment of displacement damage in silicon detectors.

The extreme radiation environment of the LHC necessitates robust shielding strategies to protect sensitive detector elements. Particles generated from proton-proton collisions and particle showers, including hadrons and various forms of electromagnetic radiation, can degrade detector performance and longevity [4]. Shielding materials and configurations must be meticulously designed to minimize these effects without compromising the detector's functionality. Based on FLUKA [5–7] simulations, this thesis investigates various shielding techniques, including the performance of neutron moderators and boron-doped materials, to optimize protection for the ATLAS detector's critical components.

For the High-Luminosity LHC (HL-LHC), the future upgrade of the LHC, more than 10 times higher radiation levels are expected [8]. Some of the shielding investigations in this thesis serve as guideline for the design of the upcoming ATLAS detector upgrade phase 2. In particular, a study of neutron moderators in the upgraded Inner Detector [9] and an investigation of the luminosity detector upgrade [10].

Developing effective shielding strategies for detector components heavily relies on accurate estimates of radiation damage effects. Silicon detectors, vital for tracking particle paths and measuring their properties, can be significantly affected by non-ionising energy loss (NIEL). The NIEL quantifies the energy lost by a traversing particle that does not contribute to ionisation but instead causes displacement damage [11].

However, only a fraction of the NIEL results in displacements, with the remaining energy dissipating as phonons. This fraction is dependent on the energy of the incident particle

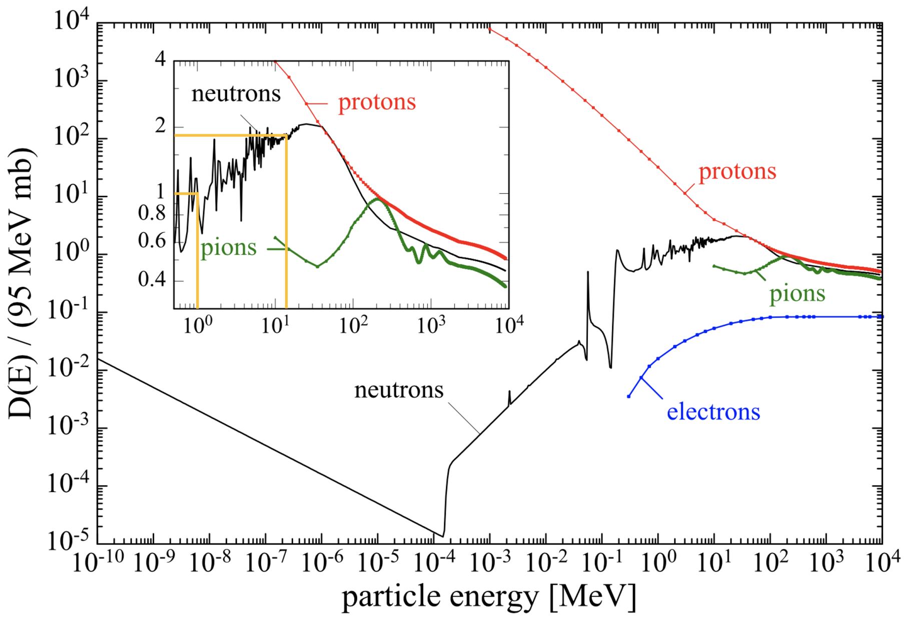

Figure 1.1.: NIEL cross sections normalised to 95 MeV·mb. Data collected by A. Vasilescu and G. Lindstroem [11] and based on [12–15].

[16]. Displacement damage occurs when incoming particles displace silicon atoms from their lattice sites, creating defects that can degrade the detector's performance over time. The NIEL can be given in units of MeV $\cdot$ cm^2/g or as the NIEL cross section (displacement damage function D) in units of MeV $\cdot$ mb. The reference value for a 1-MeV neutron equivalent (neq) is set at 95 MeV $\cdot$ mb [17]. Fig. 1.1 displays the calculated NIEL cross sections for various particles.

The displacement damage caused by particles of varying types and energies can be described using the NIEL scaling hypothesis [18]. This hypothesis assumes that radiation damage effects scale linearly with NIEL, regardless of the particle type or energy involved. Using the displacement damage function, it is possible to calculate the Si 1-MeV neutron-equivalent fluence $\Phi^{\mathrm{Si}}_{\mathrm{n_{eq}}}$ for different radiation fields.

A significant focus of this thesis is the reevaluation of the displacement damage curve of pions, shown in Fig. 1.1 in green. More than 30 years ago the hardness factors for pions were estimated by a simplistic rescaling of proton induced damage [13]. Despite the approximative nature of the method, those damage factors have been included in a compilation [11] by the RD50 collaboration [1] and are in wide use within the particle physics community ever since. Those old factors are not based on any detailed modeling of the pion-nucleus interaction or of the recoil ion transport in silicon. In addition, they were evaluated only between 15 MeV and 10 GeV.

[1] Team of scientists at CERN for the development of radiation-resistant semiconductor devices.

Discrepancies between simulation results and data from pixel sensors [19] in the ATLAS detector have puzzled the ATLAS community for over five years [20]. This issue prompted the revision of the pion factors presented in [11]. This research aims to provide a more accurate assessment of the damage mechanisms affecting silicon detectors. This involves detailed simulations and comparisons with experimental data to identify discrepancies and propose a new approach of assessing damage factors. The goal is to enhance the predictive accuracy for silicon sensor longevity and performance. By accurately predicting when sensors are likely to fail, timely replacements and maintenance can be scheduled.

In summary, this thesis seeks to advance the instrumentation in HEP by improving radiation shielding strategies and refining the understanding of displacement damage in silicon detectors. These efforts are crucial for maintaining the performance of the ATLAS detector and thereby supporting the broader mission of the LHC.

2. The ATLAS experiment at the Large Hadron Collider

2.1. The Large Hadron Collider

The Large Hadron Collider (LHC) [2], situated at the European Organization for Nuclear Research (CERN) near Geneva, Switzerland, currently holds the distinction of being the world's largest and most powerful particle accelerator. It operates by accelerating two counter-rotating beams of protons, and in specific runs, beams of various ions, to nearly the speed of light. These particles traverse the 27 km ring and collide within four interaction regions, each hosting dedicated experiments aimed at detecting, reconstructing, and analyzing collision events.

2.1.1. Motivation for the LHC

The LHC was built with two main goals: to either discover or dismiss the existence of the Higgs boson and to investigate physics that goes beyond the Standard Model (SM). The confirmation of the Higgs boson's existence in 2012 [3, 21] by ATLAS and CMS represented the conclusive evidence needed to validate the SM. The Higgs boson is remarkable as it is the only known elementary particle with a spin of 0. Its associated field is responsible for imparting mass to other fundamental particles. All particles interacting with this field acquire mass, with stronger interactions observed in more massive particles. The necessity of designing a particle accelerator as the LHC for the discovery of the Higgs boson, is outlined in the following.

A crucial aspect in the design of a particle accelerator, such as the LHC, is the detection rate of events in experiments aimed at exploring various physics processes. The probability of these processes is quantified by a production cross-section denoted as σ depending on the type and energy of the colliding particles and reaction considered. Particles like W and Z bosons at the LHC exhibit considerable production cross sections, resulting in more frequent observations. In contrast, the production of a Higgs boson involves a notably lower cross section [22], making its generation rarer. Cross sections are given in a unit called barn, with $1\ \mathrm{b} = 10^{-28}\ \mathrm{m}^2$. Given that LHC experiments aim to detect rare physics events, it is essential to generate enough events so that the signal is statistically significant with respect to fluctuations of the, usually, large background. The rate of events generated in experiments for a specific physics process is determined by

$$\frac{dN}{dt} = \mathcal{L}_{\text{inst}} \times \sigma, \tag{2.1}$$

with the cross section σ and the instantaneous luminosity $\mathcal{L}_{\text{inst}}$ that quantifies the density of particles within a defined spatial region, such as the proton beam in the LHC. Higher luminosity indicates a greater probability of particle collisions, facilitating the occurrence of desired interactions [23], it is usually expressed in $\text{cm}^{-2}\text{s}^{-1}$. The total production cross section of a 125 GeV Higgs boson is $\sigma = 50$ pb.

	Run 1	Run 2	HL Baseline	HL Ultimate
Instantaneous Lumi [$\text{cm}^{-2}\text{s}^{-1}$]	$1 \cdot 10^{34}$	$2 \cdot 10^{34}$	$5 \cdot 10^{34}$	$7.5 \cdot 10^{34}$
Higgs production rate [s^{-1}]	0.5	1	2.5	3.75
Integrated Lumi [fb^{-1}]	30	140	3000	4000
Higgs produced	$1.5 \cdot 10^{6}$	$7 \cdot 10^{6}$	$150 \cdot 10^{6}$	$250 \cdot 10^{6}$

Table 2.1.: Higgs production rate and total production number calculated with Eq. (2.1) and Eq. (2.3) for some instantaneous and integrated luminosity values taken from [24]. HL Baseline and HL Ultimate represent estimations for the high luminosity upgrade.

In the context of a circular accelerator where two beams collide head-on and possess identical Gaussian beam profiles, the expression for instantaneous luminosity is as follows [23]

$$\mathcal{L}_{\text{inst}} = \frac{N_1 N_2 f N_b}{4\pi\sigma_x\sigma_y}. \tag{2.2}$$

N_1 and N_2 represent the number of protons in the two colliding particle bunches, f is the revolution frequency of the collider, N_b is the number of bunches per beam, and σ_x and σ_y represent the widths of the beam density distributions in the x- and y-directions, respectively.

The integrated luminosity is given as

$$\mathcal{L}_{\text{int}} = \int \mathcal{L}_{\text{inst}}\, dt. \tag{2.3}$$

It is used as a measure how much data an experiment has recorded and can be given in inverse femtobarn fb^{-1}. Tab. 2.1 lists luminosity values of the LHC and the number of produced Higgs bosons calculated with Eq. (2.1) and Eq. (2.3). Fig. 2.1 shows the total integrated luminosity delivered by the LHC and collected by the ATLAS experiment during run 2, from 2015 to 2018.

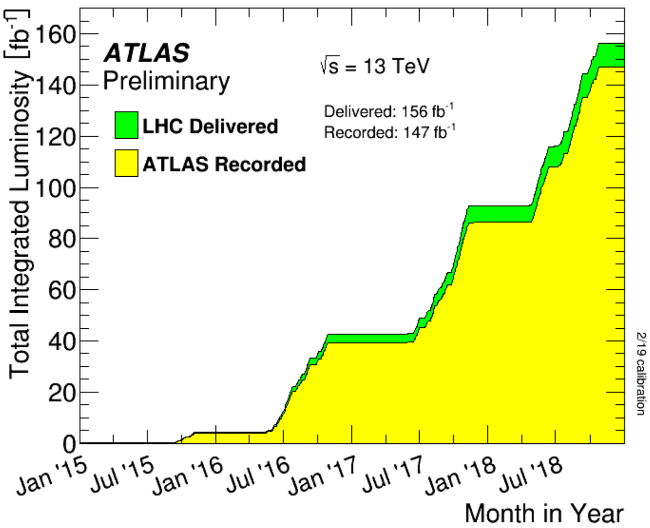

Figure 2.1.: Cumulative luminosity versus time delivered from the LHC to ATLAS (green) and recorded by ATLAS (yellow) for pp collisions at 13 TeV centre-of-mass energy in LHC Run 2. From [25]

Although high instantaneous luminosities are clearly advantageous for investigating low cross-section processes, they result in a notable presence of multiple simultaneous proton-proton interactions during a single bunch crossing. This phenomenon is referred to as pile-up and causes challenges in identifying interesting results. An additional crucial quantity in LHC operations is the center-of-mass energy denoted by $\sqrt{s}$. In the initial LHC run, collision data was gathered at $\sqrt{s} = 7$ TeV and 8 TeV and in the following run 2 $\sqrt{s}$ reached 13 TeV.

Considering the relatively low Higgs production rates outlined in Tab. 2.1, one can appreciate the scale of collisions required to advance our understanding of the Higgs and potentially discover new physics. However, such a high number of collisions also generates significant radiation levels. Before delving into the impact of radiation on silicon components of the detector, the primary focus of this thesis, some fundamental aspects of the LHC and ATLAS are reviewed.

2.1.2. Accelerator Chain and Experiments at the LHC

The LHC, illustrated in Fig. 2.2, forms an integral part of CERN's accelerator complex and represents the final stage within a series of smaller accelerators designed to gradually elevate particles to their final energies. Protons, originating from ionised hydrogen atoms, commence their journey in the LHC injection chain by entering a linear accelerator. LINAC2 [26], which was in service during LHC Run 1 (2010-2013) and Run 2 (2015-2018), played the role of the initial link in CERN's accelerator chain until recently. This position has now been taken over by LINAC4 [27], CERN's latest accelerator.

Within LINAC4, protons attain an energy of 160 MeV before their injection into three subsequent synchrotron systems: the Proton Synchrotron Booster (BOOSTER) [28], the Proton Synchrotron (PS) [29], and the Super Proton Synchrotron (SPS) [30] These synchrotrons progressively accelerate the particles to energies of 1.4 GeV, 25 GeV, and 450 GeV, respectively [31]. Ultimately, the protons are introduced into the LHC as dual beams, coursing through distinct beam pipes in opposing directions.

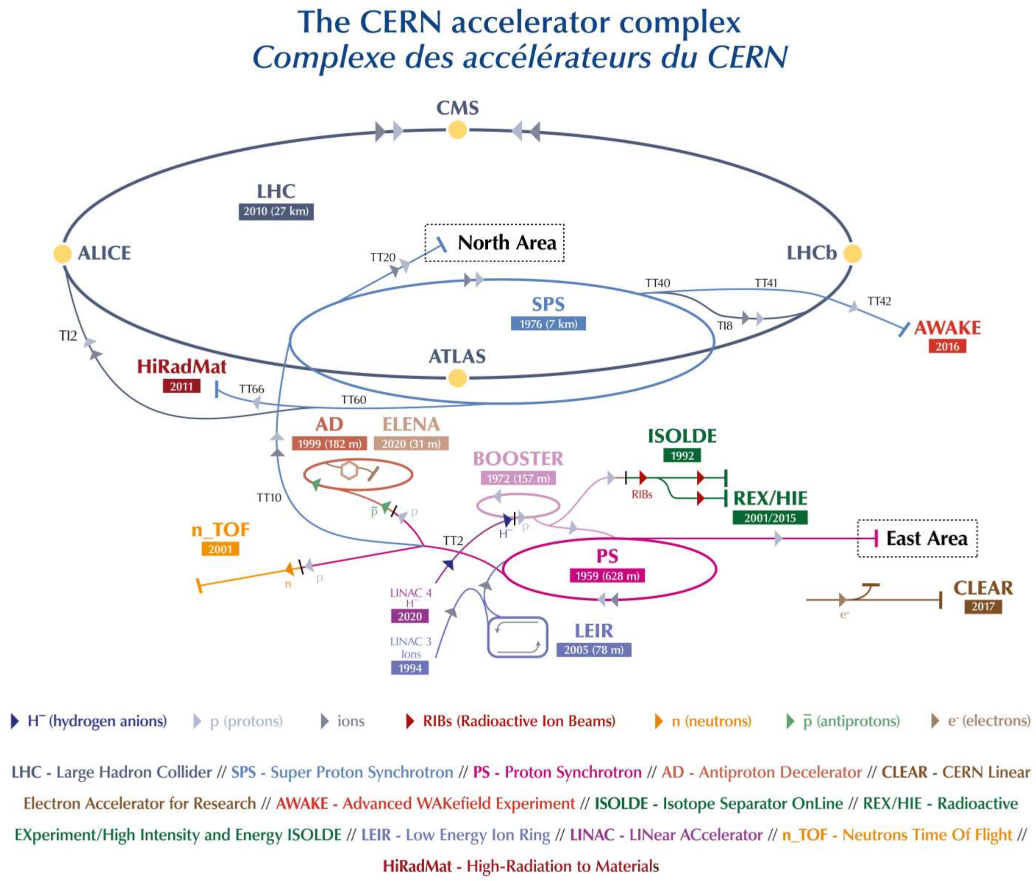

Figure 2.2.: Sketch of the LHC accelerator complex. From [32]

The LHC comprises 1232 superconducting dipole magnets, each extending 15 meters in length and maintained at a temperature of 1.9 K. These magnets facilitate the essential lateral acceleration to keep the charged particles following their circular trajectory within the accelerator ring. The longitudinal acceleration is carried out by superconducting radio-frequency cavities, which drive the particles towards a final proton energy of 6.8 TeV, leading to a center-of-mass energy $\sqrt{s} = 13.6$ TeV. The design values of the dual particle beams comprise 2808 bunches, each containing around 10^{11} protons, separated by intervals of 25 ns. This arrangement results in a bunch-crossing frequency of 40 MHz within the primary LHC experiments, namely ALICE, [33] ATLAS, [1] CMS [34], and LHCb [35].

Each of the four experiments is located within a large underground cavern along the particle collider. The configurations of the detectors are meticulously tailored to match the specific physics objectives of each experiment. These are briefly described in the following:

- At the ALICE experiment [33] the physics of strongly interacting matter at extreme energy densities is investigated, in which a phase of matter called quark-gluon plasma is formed.
- ATLAS [1] serves as one of the two general-purpose detectors at the LHC. It explores a diverse spectrum of physics, spanning from the Higgs boson to potential extra dimensions and particles that could constitute dark matter.
- CMS [34] shares similar scientific objectives with the ATLAS experiment, but employs distinct technical approaches and a different magnet-system design.
- The LHCb experiment [35] is dedicated to scrutinizing the subtle distinctions between matter and antimatter through the analysis of a specific particle, namely the bottom (b) quark.

2.1.3. Operational History and High-Luminosity Upgrade

In the 2020s, the LHC is scheduled for a significant upgrade to enhance and expand its potential for discoveries. This upgrade aims to increase the instantaneous luminosity by 3 - 4 times beyond the original design. Given the intricate and highly optimised nature of the LHC, this upgrade requires meticulous planning and a roughly ten-year implementation timeline [36]. The luminosity increase results in a significantly higher level of radiation within the detector. This poses a significant challenge to the ATLAS Phase 2 detector systems. Consequently, it is imperative to conduct radiation studies to comprehend the radiation distribution within ATLAS and determine the anticipated radiation levels experienced by the detector components.

2.2. The ATLAS Experiment

The overall design of the ATLAS experiment [1], illustrated in Fig. 2.3, aligns with its general-purpose concept. It aims to explore a wide spectrum of physical phenomena, thus covering nearly the entire solid angle. Given the 25 ns bunch structure of the LHC and the need to handle large datasets, the various detector components are equipped with fast, radiation-hard sensors and readout electronics. Moreover, a high spatial resolution is essential to distinguish multiple events occurring simultaneously. The ATLAS detector spans a total length of 44 m, has a height of 25 m, and weighs 7000 t [1]. The arrangement comprises a set of sub-detector systems structured in cylindrical layers, with each system specifically tailored to accurately measure unique properties of particles arising from the Interaction Point (IP) within the detector. The innermost system, known as the Inner Detector (ID) [37, 38] is utilised to reconstruct charged particle trajectories. The ID is surrounded by the solenoid magnet system, as well as electromagnetic and hadronic calorimeters designed for precise energy measurements. The outermost layer of the ATLAS detector is the muon tracking system, situated within a magnetic field generated by toroid magnets [1].

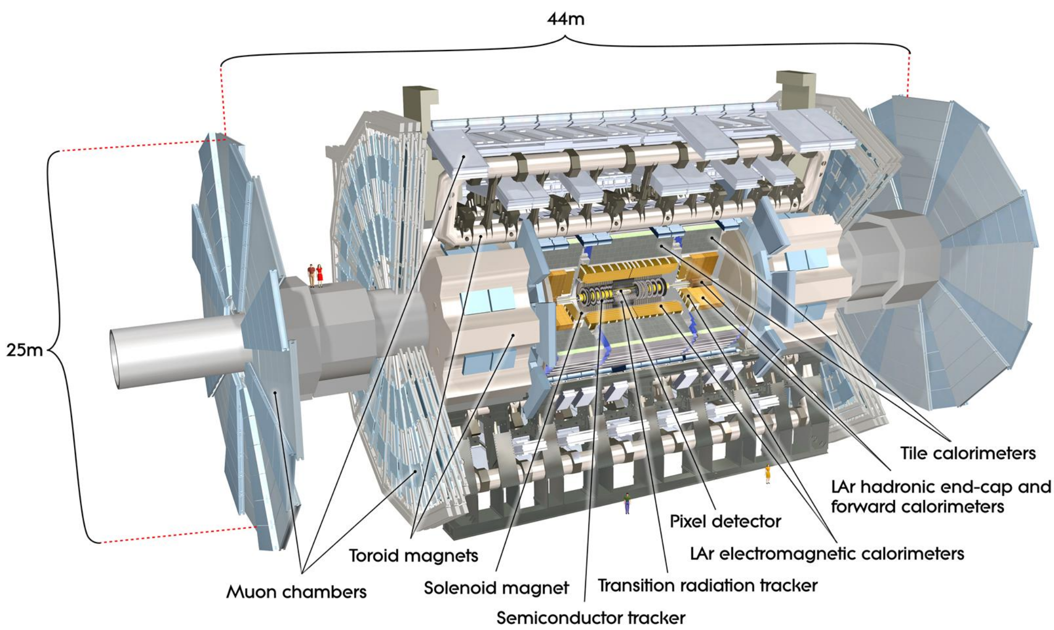

Figure 2.3.: Schematic illustration of the ATLAS detector at the LHC at CERN. From [1]

2.2.1. Relevant Parameters

The ATLAS coordinate system is defined as a right-handed coordinate system, with its origin situated at the nominal collision point within the detector's center. As depicted in Fig. 2.4 the z-axis is aligned with the counter-clockwise LHC beam, the positive x-axis extends towards the center of the LHC ring, and the positive y-axis points upward, perpendicular to the LHC plane. The x-y plane is referred to as the transverse plane, wherein the azimuthal angle ϕ is defined with respect to the x-axis. Additionally, the polar angle θ is defined as the angle measured from the positive z-axis within the y-z plane [1].

In place of the polar angle θ, a measure called pseudorapidity η, is commonly used. It is defined as

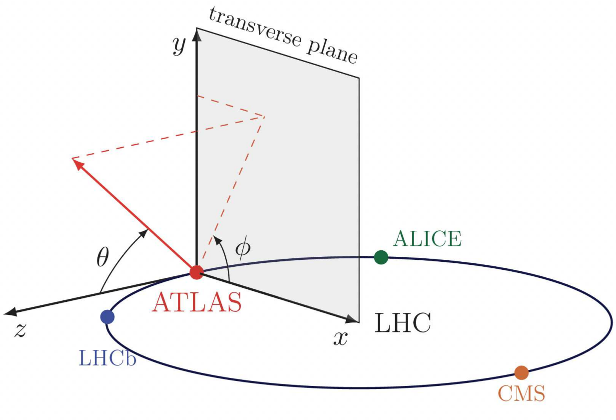

Figure 2.4.: The ATLAS coordinate system [1].

$$\eta = -\ln\left(\tan\frac{\theta}{2}\right).$$

The concept of pseudorapidity is useful as the differential cross sections governing jet production in hadron–hadron collisions exhibit a pseudorapidity-independent trend. This suggests a nearly equal number of jets detected within each pseudorapidity interval [39].

The transverse momentum

$$p_T = \sqrt{p_x^2 + p_y^2} \tag{2.4}$$

and transverse energy

$$E_T = \sqrt{m^2 + p_T^2} \tag{2.5}$$

are significant measures, enabling the identification of particles that escape detection within the detector. Protons, like all hadrons, consist of partons, each of them carrying a random amount of the total proton momentum. The transverse momentum is a crucial quantity because the initial state colliding partons possess nearly zero momentum in the transverse plane. As a consequence of momentum conservation the total sum of transverse momentum among all particles in the final state must be zero. Deviations significantly away from zero indicate particles that have evaded detection by the detector [1]. As the partons carry an unknown fraction of the proton momenta, the conservation of p_z cannot be employed. The concept of Missing Transverse Energy (MET) is crucial in particle physics experiments, especially in the context of trigger systems like the Level 1 (L1) trigger. Missing energy can be attributed to particles such as neutrinos or hypothetical particles like dark matter.

In experiments at the Large Hadron Collider (LHC), the detection of MET is a key criterion for identifying potentially interesting events, such as those involving the production of new, massive particles that decay into undetectable or weakly interacting particles. The L1 trigger, being the first stage of the trigger system, relies on fast, hardware-based algorithms to quickly identify such events based on basic information, including MET, in order to efficiently select data for further analysis.

2.2.2. Magnet System

A crucial particle property to measure is the mass, and this can be achieved through two distinct approaches, either with

$$E^2 = m^2c^4 + p^2c^2 \tag{2.6}$$

by measuring particle energy E and momentum p; or with

$$p = mv\gamma \tag{2.7}$$

by measuring momentum and velocity v. With the Lorentz factor

$$\gamma = \frac{1}{\sqrt{1-\beta^2}} \tag{2.8}$$

with

$$\beta = \frac{v}{c}. \tag{2.9}$$

In the context of this thesis only Eq. (2.6) is relevant, meaning that p and E have to be measured. The measurement of E is discussed in Section 2.2.5. The measurement of p is accomplished through the utilisation of a magnetic field. A particle of charge q travelling perpendicular to a magnetic field B with a velocity v experiences a force $B \cdot q \cdot v$ perpendicular to its motion. This causes the particle to follow a circular path of radius R, and the motion is described by

$$B \cdot q \cdot v = \frac{m \cdot v^2}{R}. \tag{2.10}$$

This can be rewritten as

$$p = B \cdot q \cdot R \tag{2.11}$$

to illustrate that for a fixed field and charge, the momentum is proportional to the radius of the curvature.

The ATLAS experiment employs an intricate magnet system consisting of one solenoid and three toroids, which define the magnetic field within both the inner detector and the muon spectrometer. The central solenoid generates a 2 T magnetic field along the z-axis, causing particle deflections in the ϕ-direction. Additionally, the barrel and endcap toroids in the muon detector establish a magnetic field ranging between 0.5 and 1 T, effectively deflecting muons in the η-direction to enable accurate momentum measurements [40].

2.2.3. Beam Vacuum System

The beam-vacuum system in the ATLAS experimental area comprises seven beam-pipe sections with a total length of 38 m. These pipes are joined using flanges to create an ultra-high vacuum system. The central chamber, known as the VI (vacuum inner detector), is positioned at the interaction point and has a diameter of 58 mm, constructed from beryllium metal [1]. The six remaining chambers are symmetrically installed on both sides of the interaction point and are named according to the supporting detector: VA (vacuum argon end-cap), VT (vacuum toroid end-cap), and VJ (vacuum forward shielding). They are built from thin-walled stainless steel tubes with diameters gradually increasing from 60 mm to 80 mm and finally to 120 mm. These diameters strike a balance between allowing detectors to approach the beam axis and maximizing diameter to minimize interactions between the beam pipe and particles from interactions. [41].

2.2.4. Inner Detector

The core component of ATLAS is the Inner Detector (ID) [37, 38], designed to track charged particles from the interaction point to the calorimeter and determining their momentum by analyzing the curvature of their trajectories within the magnetic field. The ID encompasses a region with a pseudorapidity of $|\eta| < 2.5$ and a radius spanning from 3 cm to 1 m. The ID operates in an environment characterised by a high density of particle tracks, demanding a detector with fast response and resistance to radiation, as well as high granularity for precise reconstruction of tracks, from which momenta and vertices are derived. It comprises three distinct sub-systems: the Pixel Detector, the

[1] Beryllium is favored for constructing beam vacuum chambers near collision points in particle colliders due to its transparency to particles, high specific stiffness, and compatibility with ultra-high vacuum conditions.

SemiConductor Tracker (SCT) [42], and the Transition Radiation Tracker (TRT) [43]. The ID and its subsystems are illustrated in Fig. 2.5.

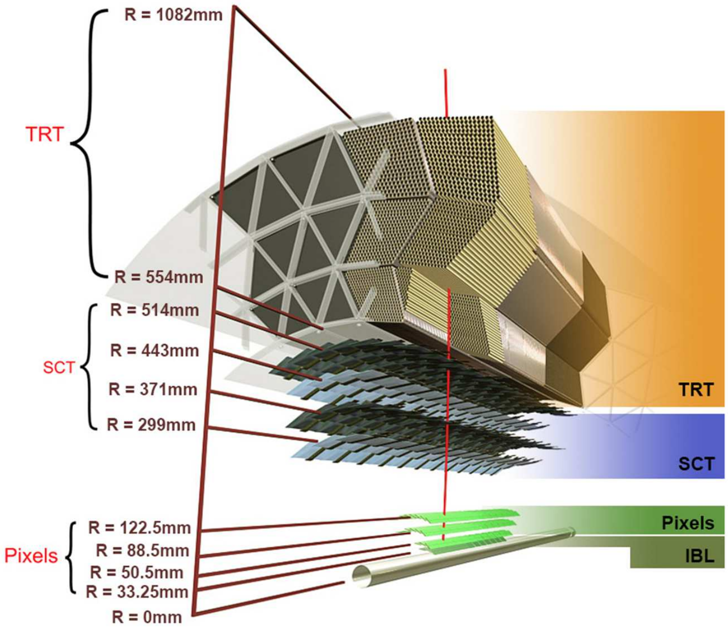

Figure 2.5.: Sketch of the ATLAS inner detector showing all its components, including the insertable B-layer (IBL), the pixel layers, the SemiConductor Tracker (SCT) and the Transition Radiation Tracker (TRT). From [44]

Pixel Detector

The innermost component, known as the silicon pixel detector [19], is structured with three layers in the barrel region and three layers in the endcap region. This system comprises a total of 1744 pixel modules, collectively housing 80 million pixels. The individual modules feature a pixel pitch of 50x400 μm^2 and a sensor thickness of 250 μm. A notable enhancement was introduced during the first extended shutdown of the LHC (LS1) with the installation of the Insertable B-Layer (IBL) [45]. Positioned at a distance of 33 mm from the beamline, the IBL incorporates 12 million pixels, each with a pitch of 50x250 μm^2. The introduction of the IBL was aimed to significantly advance the tracking robustness and precision.

SemiConductor Tracker (SCT)

The subsequent layer in the ID setup is the SCT, which employs silicon microstrip modules. These modules are structured into four concentric barrel layers and two endcaps, each consisting of nine disks [42]. The strips have a pitch of 80 μm, and the detectors themselves have a thickness of 285 μm. Each module combines two strip detectors, configured with a stereo angle of 40 mrad, allowing for hit reconstruction in two dimensions. The SCT modules provide a resolution of 17 μm in the $R - \phi$ plane and 580 μm in the longitudinal z direction [46].

Transition Radiation Tracker (TRT)

The outermost component of the ID is the TRT; a straw-tube tracker consisting of approximately 300.000 cylindrical drift tubes (straws) with a diameter of 4 mm. Thus, in contrast to the Pixel and SCT sub-detector systems, its particle detection is not based on silicon but gas. Each straw has a gold-plated anode wire and is filled with a gas mixture primarily based on Xenon. When a charged particle passes through the tube, it ionises the gas. The resulting electrons drift towards the anode wire, creating an avalanche of further electrons that amplify the signal. This detectable signal can be compared against adjustable thresholds. In addition, the spaces between individual straws are filled with specialised materials, such as polymer fiber. These materials cause incident particles to generate extra transition radiation photons, which, in turn, ionise the gas within the straws, resulting in larger signals in the anode wire. The energy of transition radiation photons, and consequently the induced signals, scales proportionally with γ of the traversing particle. As a result, the size of the read-out pulse can be utilised to discriminate electrons (which generally possess higher γ due to their lower mass) from heavier particles like pions or muons. This complements the electron identification carried out in the calorimeter system [43].

By integrating all three components of the ID, it becomes possible to reconstruct the trajectory of a charged particle within the detector. The curvature of this trajectory provides the means to determine the particle's momentum. The performance goal of the ID according to [1] in terms of momentum resolution σ_{p_T} is

$$\frac{\sigma_{p_T}}{p_T} = 0.05\%\ p_T \oplus 1\% \tag{2.12}$$

where p_T represents the transverse momentum and $\oplus$ indicates a quadratic sum.

2.2.5. Calorimeter System

The ATLAS calorimeter system, comprising both an electromagnetic and a hadronic calorimeter, measures the energy of particles that interact electromagnetically and hadronically. It plays a crucial role in determining missing transverse momentum. The calorimeters are surrounding the ID as shown in Fig. 2.6. Each of these components is meticulously designed to induce interactions between the particles passing through the dense detector material, thereby generating electromagnetic and hadronic particle showers that deposit their energies in the respective parts of the calorimeter [47]. According to [48] the relative energy resolution $\Delta E/E$ of a calorimeter system can be expressed as

$$\left(\frac{\Delta E}{E}\right)^2 = \left(\frac{c_s}{\sqrt{E}}\right)^2 + \left(\frac{c_n}{E}\right)^2 + c_c^2. \tag{2.13}$$

The first term with the coefficient c_s is the stochastic term, encompassing fluctuations associated with Poisson statistics, such as shower or sampling variations. The second component with the coefficient c_n represents the noise term, accounting for electronic noise in the detector readout. Lastly, the constant term with the coefficient c_c characterizes instrumental effects, including inefficiencies in signal collection. The stochastic term scales inversely with the square root of the particle's energy, since the number of shower particles grows with higher energies. Since the first two terms decrease with energy, the constant term becomes dominant, encompassing uncertainties in the tails of showers that may not be entirely captured by the detector [49].

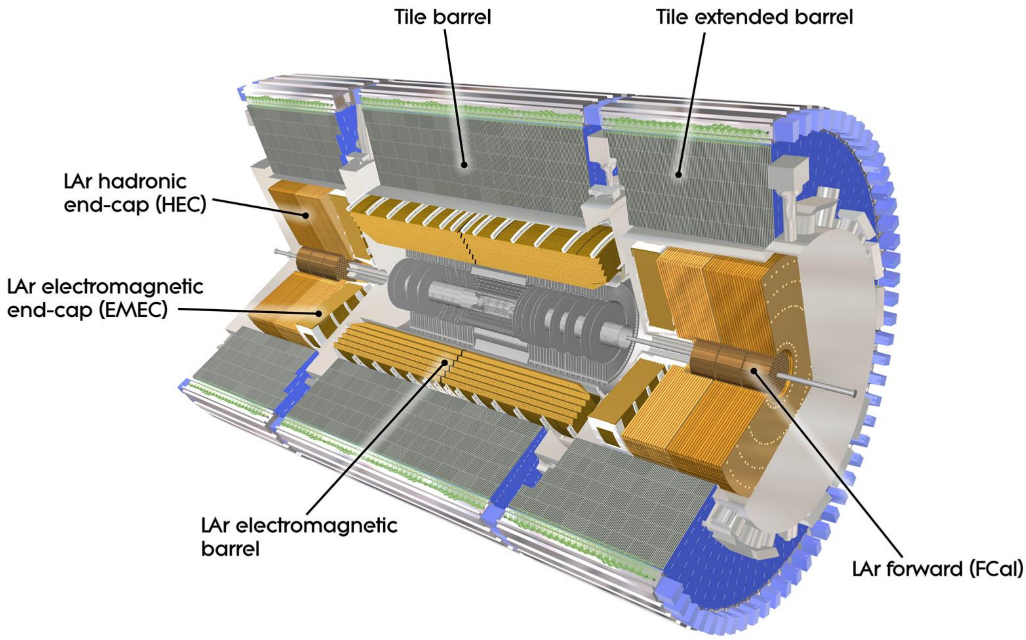

Figure 2.6.: Schematic of the ATLAS calorimeter system. From [50]

In the following a brief summary of the design and operational principles of the calorimeter sub-detector components is provided.

Electromagnetic Calorimeter (ECAL)

The ECAL serves the precise measurement of electromagnetic showers initiated by electrons and photons. It consists of both a barrel and an end-cap system, employing a configuration of alternating layers of dense absorber material, responsible for generating the particle showers, and active material, used to quantify the deposited energies. The ATLAS ECAL uses lead as absorber material and liquid argon (LAr) as active material. This type of calorimeter design, using alternating layers of absorber and active materials, is commonly known as a "sampling calorimeter". Electromagnetic showers are characterised by the radiation length X_0, representing the average distance over which the energy of a high-energy electron diminishes to $1/e$ of its initial value. The electromagnetic calorimeters within ATLAS are designed with a minimum depth of 22 X_0 [47].

Hadronic Calorimeter (HCAL)

The role of the HCAL is to measure the energy of hadrons originating from quark or gluon-induced particle jets, as well as the decays of τ leptons or other hadronic decays. Much like the electromagnetic calorimeter, the HCAL is constructed as a sampling calorimeter, with both a barrel and an end-cap configuration. In the barrel section, the detector material comprises steel and specialised scintillators, whereas the hadronic end-cap utilizes a combination of LAr and copper. Hadron showers are characterised by a quantity called the nuclear interaction length λ_I which signifies the average distance a hadron travels before undergoing an inelastic interaction with a nucleus. The depth of the ATLAS hadronic calorimeters corresponds to approximately 10 λ_I. The nuclear interaction length should not be confused with the mean free path or the nuclear collision length. While the mean free path and the nuclear collision length are equivalent and include all types of interactions, the nuclear interaction length focuses on significant nuclear interactions, excluding elastic ones. Thus, each quantity can be derived from the same equation with different cross sections

$$\lambda_i = \frac{A}{N_A \sigma_i \rho}, \tag{2.14}$$

with the atomic weight A, Avogadro's number N_A, density ρ and the total cross section σ_i for the mean free path λ_i. For the collision length λ_C only the nuclear interactions are considered in the cross section σ_C and for the interaction length λ_I the sum of elastic and quasi-elastic cross sections is further subtracted from σ_C to derive σ_I.

Values of radiation length, nuclear interaction - and collision length for different detector materials are given in Tab. 2.2. The listed data reflects the choice of materials for the ECAL and HCAL. Due to the higher density of Pb it might seem surprising that λ_I is smaller for Cu than for Pb. This, however, can be explained with Eq. (2.14). σ approximately increases like $A^{2/3}$ [51], hence, the numerator increases faster than the denominator and λ_I for Pb with higher A is larger.

Material	Radiation Length X_0 (cm)	Nuclear Interaction Length λ_I (cm)	Nuclear Collision Length λ_C (cm)
Si	9.37	46.52	30.16
LAr	14.00	85.77	54.25
Cu	1.436	15.32	9.394
W	0.3504	9.946	5.719
Pb	0.5612	17.59	10.05

Table 2.2.: Nuclear properties of detector materials. Data taken from [52].

Forward Calorimeter (FCAL)

The FCAL, a three-layered hybrid of electromagnetic and hadronic calorimeters, covers the range of $3.1 < |\eta| < 4.9$. Its initial layer is tailored for precise electromagnetic energy measurements, while the subsequent two layers are specialised for capturing hadronic interactions. The absorber materials are composed of W and Cu, while the active material is LAr.

2.2.6. Muon Spectrometer (MS)

The muon spectrometer (MS) forms the outermost and largest detector system in ATLAS, extending to a radius of up to $r = 11$ m, illustrated in Fig. 2.3. It is designed to measure the trajectory and momentum of muons in a pseudorapidity region of $|\eta| \leq 2.7$. It comprises four gas-based sub-detector systems, with two located in the central barrel and two in the forward region. Within each region, one system is dedicated to precision momentum measurements, employing monitored drift tubes covering $|\eta| < 2.0$ in the barrel and cathode strip chambers covering $2.0 < |\eta| < 2.7$ in the forward region. The other system, used for the ATLAS trigger system, features fast response times with coarser granularity.

Muon trigger chambers are composed of resistive-plate chambers in the barrel and thin-gap chambers in the forward region. A superconducting toroid magnet system provides strong magnetic fields to bend muon trajectories, enabling precise momentum measurements. This system, situated outside the calorimeter and within the ATLAS muon system, generates magnetic fields of up to 4 T. It consists of eight barrel coils, each weighing approximately 100 tons, and two end-cap systems, operated at a nominal temperature of 4.7 K.

While muon spectrometers can operate independently for muon reconstruction and identification, additional tracking information from the ID is usually incorporated, significantly enhancing the overall performance of the sub-detector [53].

2.2.7. Trigger and Data Acquisition (DAQ)

At the LHC bunch-crossings occur every 25 ns, amounting to a rate of 40 MHz. However, due to computing constraints, only a subset of events can be stored. To efficiently select relevant physics processes while discarding unimportant events, ATLAS utilises a trigger system [54].

The ATLAS trigger system employs a two-tier approach to reduce the data rate to 1 kHz. The hardware-based Level-1 trigger quickly identifies high-momentum objects using basic information from the calorimeters and muon spectrometer. This narrows down the data to 100 kHz by focusing on Regions of Interest (RoIs) with intriguing features. Subsequently, the software-based high-level trigger integrates RoI data with full detector information to perform detailed event reconstruction. Advanced trigger algorithms then make event selection decisions, accommodating complex signatures like leptons, missing transverse energy and b-jets. This multistage process efficiently optimizes data collection while preserving significant physics events.

2.2.8. ATLAS Phase-2 Upgrade for the High Luminosity LHC upgrade

To adapt to the demanding conditions of the HL-LHC, which will introduce considerable pile-up effects (see Section 2.1.3), various ATLAS sub-detector systems and key software components require substantial upgrades referred to as ATLAS Phase 2 upgrade. This section briefly addresses the upcoming hardware enhancements, of the new Inner Tracker (ITk), the High-Granularity Timing Detector (HGTD) and the LUCID detector.

Inner Tracker (ITk)

During the ATLAS Phase-2 upgrade for HL-LHC, the entire ID will be replaced by the new, all-silicon ITk [9] schematically illustrated in Fig. 2.7. It is designed to improve the resolution and radiation hardness of the ATLAS tracker to cope with the severe upcoming pile-up conditions, by exploiting new sensor and read-out electronics technologies as well as a novel dedicated detector design, as schematically illustrated in Fig. 2.7. Its layout consists of a silicon pixel detector, the innermost part of the ITk, instrumented with high-granularity silicon pixels with the size of $25\,\mu\text{m} \times 100\,\mu\text{m}$ and $50\,\mu\text{m} \times 50\,\mu\text{m}$ for the barrel and disks respectively. The pixel detector is enclosed by a silicon strip detector system with strip lengths of 24.1 mm in the innermost layers and 48.2 mm in the outermost layers where the expected occupancy will be lower. The pixel subsystem comprises five flat barrel layers as well as five layers of inclined or vertical rings which together provide a coverage of up to $|\eta| = 4$. The strip sub-detector system consists of four strip module layers in the barrel region as well as six disks in the end-caps, resulting in a $|\eta| < 2.7$ pseudo-rapidity coverage.

The considerable high-granularity extension of tracking coverage in the forward region compared to the ATLAS ID will, in addition to providing a significantly better efficiency and acceptance in the forward region, also cover a large part of the forward calorimeter systems and therefore enables an enhanced reconstruction of forward physics objects.

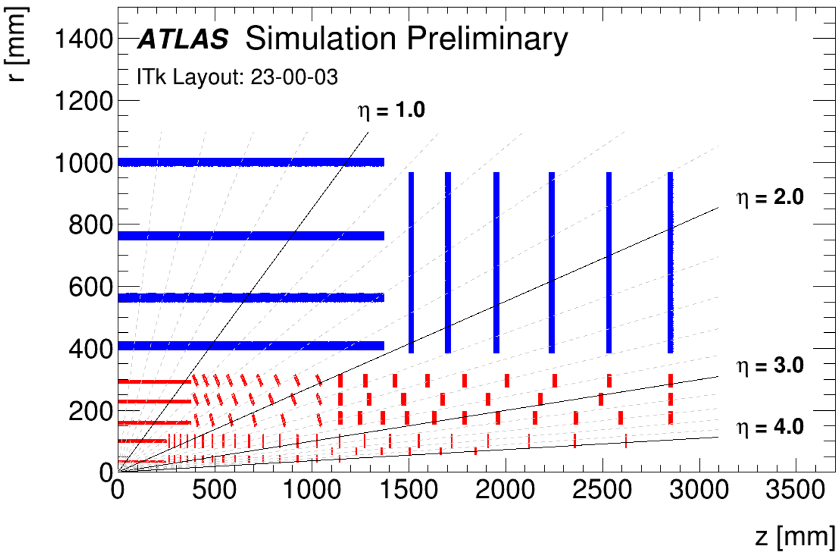

Figure 2.7.: Schematic representation of the ITk detector layout, highlighting the active components of the pixel sub-detector system in red and those of the strip sub-detector system in blue. The pseudorapidity η intervals relative to the beam axis z are illustrated as well. From [55].

High-Granularity Timing Detector (HGTD)

The anticipated high luminosity conditions at HL-LHC are projected to result in pile-up densities of up to 4 primary vertices per millimeter along the beam axis. In such an environment, accurately identifying the hard-scatter vertex and correctly associating tracks and physics objects with it will pose a significant challenge.To address this challenge, the HGTD is being introduced to the Phase 2 upgrade. It enhances the capabilities of the ITk detector by enabling the measurement of charged particle tracks not only in space but also in time, achieving a timing resolution of less than 50 ps [56].

Luminosity Detector

The luminosity detector (LUCID) operates as a counting experiment to measure luminosity at the LHC. The present Run 3 detector is LUCID-2, consisting of 16 + 16 photomultipliers, located 17 m away from the interaction point at a distance of 125 mm from the proton beams and on both side of the experiment. The detector assesses the probability of it being hit per bunch crossing. In its simplest form, LUCID employs event counting, i.e. registers how often it is hit per bunch crossing. The luminosity is then derived from the ratio of observed hits to the total number of bunch crossings. However, at high collision rates, if LUCID detects signals in every single bunch crossing, it becomes saturated, rendering the luminosity measurement unreliable. This saturation occurs due to the detector's broad acceptance, which leads to an increased likelihood of detecting signals. For this reason a detector with lower acceptance is required for the HL-LHC upgrade.

Two primary detector options are currently being investigated. The first option employs photomultipliers positioned at a greater distance from the beamline than LUCID-2 and features a smaller active area. This configuration aims to decrease the detector's acceptance in order to prevent saturation of the luminosity algorithms. In the baseline proposal the photomultipliers of LUCID-3 are attached to the centre hole in the forward muon shielding. This proposed so-called JF detector is one meter closer to the IP and the distance to the beamline can be increased from 126 mm to 291 mm. The second option utilizes optical fibers that serve as both Cherenkov radiators and light guides, directing the generated light to the readout photomultipliers, attached around the beampipe instead of the forward muon shielding. Location of LUCID-2 and the options for LUCID-3, within ATLAS, are indicated in Appendix B in Fig. B.1.

A significant modification in the Phase 2 geometry is the new positioning of the Vacuum Assembly for eXperimental area (VAX). It will be moved from its current Run 3 position around $z \approx 22$ m to a proposed position close to the location of the present LUCID-2 detector. Its change in position is illustrated in Appendix B in Fig. B.2. This change aims to reduce the need to access the high radiation area in case of failure of the VAX [57]. For the purpose of this thesis, the geometry changes have been incorporated into the FLUKA geometry of ATLAS. An exploration of simulation outcomes in Section 6.4 investigates differences in radiation effects between the two LUCID-3 options and the repositioning of the VAX.

3. Theoretical Background

3.1. Interactions of Particles with Matter

Particle physics experiments aim to detect and identify particles generated in high-energy collisions. Among the produced particles, only the stable ones, such as the electron, proton, photon and neutrinos, can persist. Unstable particles, on the other hand, decay after travelling a distance approximately determined by $\gamma v \tau$ [39]. Here, τ represents the mean lifetime of the particle in its rest frame. If the lifetime of a relativistic particle is sufficient so that it can travel a significant distance from the point of production, it can be directly detected. Examples of relatively long-lived particles include the muon ($\tau_{\text{rest}} \approx 2.2 \times 10^{-6}$ s), neutron($\tau_{\text{rest}} \approx 8.8 \times 10^{2}$ s), charged pions ($\tau_{\text{rest}} \approx 2.6 \times 10^{-8}$ s), and charged kaons ($\tau_{\text{rest}} \approx 1.24 \times 10^{-8}$ s). Conversely, short-lived particles such as the neutral pion ($\tau_{\text{rest}} \approx 8 \times 10^{-17}$ s) or the higgs boson ($\tau_{\text{rest}} \approx 1.24 \times 10^{-22}$ s) decay before they can travel a significant distance, leaving only their decay products detectable. Particle physics collider experiments rely not only on the observation of stable and relatively long-lived particles but also on identifying unstable particles through the observation of their decay products, and considering the energy balance, especially for invisible particles emitted, such as neutrinos. The detection and identification techniques utilised depend on the specific ways in which these particles interact with matter, generally classified into three main categories [39]:

Continuous energy loss of charged particles: This category involves the interactions of particles that possess electric charge. These interactions can be studied through the detection of charged tracks left behind in detectors, which provide information about the particle's momentum, trajectory, and energy loss.

Electromagnetic interactions of electrons and photons: Electrons and photons, being electrically charged or neutral, respectively, exhibit electromagnetic interactions. These interactions are detected through the measurement of electromagnetic radiation emitted or absorbed by the particles, such as the detection of photons in calorimeters or the measurement of electron tracks in tracking detectors.

Strong interactions of charged and neutral hadrons: Hadrons, such as protons, neutrons, and mesons, experience strong interactions mediated by the strong nuclear force. These interactions are typically studied through the detection of hadronic showers produced in calorimeters, where the energy and pattern of particle deposition provide insights into the nature of the interacting particles.

3.1.1. Interactions of Charged Particles

When a relativistic charged particle moves through a medium, it undergoes electromagnetic interactions with the atomic electrons, resulting in the loss of energy through the ionisation of atoms. The mean energy loss per unit length (dE/dx) travelled by a singly charged particle, with a velocity of $v = \beta c$, passing through a medium with an atomic number Z and number density n, can be described by the Bethe-Bloch equation

$$-\frac{dE}{dx} = Kz^2 \frac{Z}{A}\frac{1}{\beta^2}\left[\frac{1}{2}\ln\left(\frac{2m_e c^2\beta^2\gamma^2 W_{\max}}{I^2}\right) - \beta^2 - \frac{\delta}{2} - \frac{C}{Z}\right]. \tag{3.1}$$

$W_{\max}$ represents the maximum kinetic energy that can be transferred to a free electron in a single collision. I is the effective ionisation potential of the material averaged over all atomic electrons. I can roughly be approximated by $I \sim 10\ Z$ eV [39]. Z is the atomic number and A the atomic mass of the absorber. In a specific medium, the rate at which a charged particle loses ionisation energy depends on its velocity. Due to the $1/\beta^2$ term in Eq. (3.1) the energy loss per unit distance is highest for particles with lower velocities. $K = 4\pi N_A r_e^2 m_e c^2$ with the electron mass m_e and Avogadro's number N_A.

The validity of Eq. (3.1) extends to the interval $0.1 \leq \beta\gamma \leq 1000$ with an accuracy of a few percent [52]. For values of $\beta\gamma$ around 0.1, the speed of the projectile is comparable to that of atomic electrons, around $\beta\gamma \approx 1000$ radiative effects, such as pair production,bremsstrahlung and photonuclear interactions become significant. Both limits depend on Z [52]. Eq. (3.1) within its valid interval is plotted in Fig. 3.1 for different particles and targets. At low $\beta\gamma$, $1/\beta^2$ is the dominating factor and in this region the stopping power decreases with increasing energy. At $\beta\gamma = 3.8 - 3.0$ a minimum is reached [52]. For different materials with the same Z the $\beta\gamma$ where the minimum appears is almost the same. Below the minimum ionising energy, different particles have a different $\frac{dE}{dx}$ behaviour. This property can be used for particle identification [58]. At higher $\beta\gamma$ values the term $1/\beta^2$ becomes almost constant and the stopping power rises due to the increase of the argument of the logarithmic term.

From Eq. (3.1) it is apparent that $\frac{dE}{dx}$ is proportional to Z/A. Given that nuclei contain approximately equal numbers of protons and neutrons, Z/A remains relatively constant. Accordingly, $\frac{dE}{dx}$ is proportional to the density, but apart from that is not significantly influenced by the material. This can be seen in Fig. 3.1, where particles with the same speed exhibit similar rates of energy loss while traversing different materials, with the exception of H. In order to extend the validity of Eq. (3.1) to higher momenta another effect needs to be accounted for. Namely, that the presence of a charged particle creates an electric field that tends to polarize the atoms along its trajectory. Due to this polarization, electrons located farther away from the particle's path experience a reduced electric field intensity. Consequently, collisions with these outer electrons contribute less to the total energy loss than considered in the Bethe-Bloch formula. This effect becomes increasingly significant as the particle's energy increases [58]. The impact of

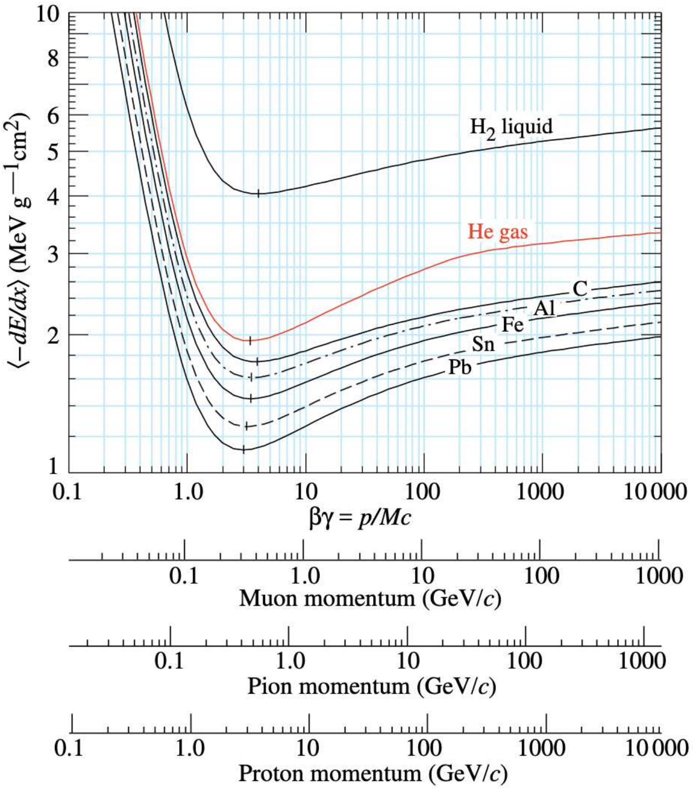

Figure 3.1.: Mean energy loss rate as a function of $\beta\gamma$ and particle energy for different particles on different x axis. Shown for different materials and based on the Bethe-Bloch Eq. (3.1). Radiative effects are not included, thus the validity ends depending on the particle and material around $\beta\gamma > 1000$. Taken from [39].

.

this effect varies with the density of the material since condensed materials show greater induced polarization compared to lighter substances such as gases, hence, this correction is referred to as density correction and expressed as δ. As mentioned previously, $\frac{dE}{dx}$ at $\beta\gamma$ values above the minimum, rises due to the logarithmic term. The density correction counteracts this rise. Furthermore, the equation's validity extends to lower values of $\beta\gamma$, accounting for effects that arise when the velocity of the incident particle becomes comparable to or smaller than the velocity of atomic electrons. At these energies, the Bethe-Bloch formula breaks down as it assumes electrons that are stationary compared to the speed of the incident particle. An additional correction, known as the shell correction and denoted as C, is applied to address this issue, typically resulting in small adjustments.

As an example in the context of this thesis, the Bethe-Bloch equation can be used to compute the energy at which different particles start to penetrate a thin beryllium layer. Protons penetrate a 868 μm thick beryllium layer at a kinetic energy around 7 MeV, kaons at roughly 5 MeV and pions at about 3 MeV as shown in Fig. 3.2. Such calculations can be applied to the beryllium beam pipe described in Section 2.2.3 and used as in Section 7 to understand what energy/momentum pions need to penetrate the beam pipe and reach the IBL layer, and how large their energy loss is.

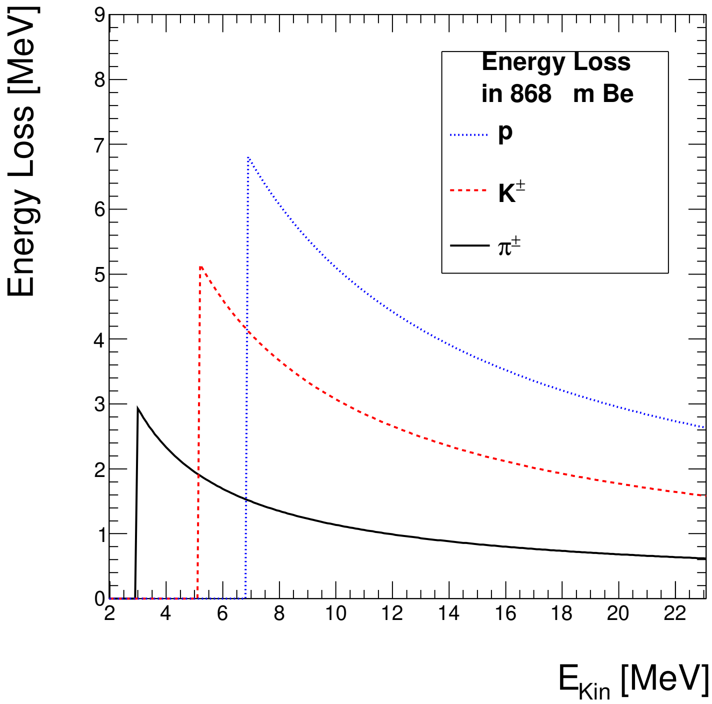

Figure 3.2.: Stopping of charged particles in beryllium according to the Bethe-Bloch Eq. (3.1)

Electrons and positrons, similar to heavy charged particles, lose energy through collisions when they traverse matter. Additionally, due to their relatively low mass the emission of electromagnetic radiation becomes significant. This is caused by scattering in the electric field of a nucleus, known as bremsstrahlung [58]. This process can occur for all charged particles, but the rate is inversely proportional to the square of the mass of the particle and thus is most significant for electrons and positrons. When the energy is within the range of a few MeV or lower, the contribution of bremsstrahlung as an energy loss mechanism is relatively insignificant even for electrons and positrons. However, as the energy level rises, the likelihood of bremsstrahlung increases significantly. The critical energy is defined as the point when radiative losses exceed the collision-ionisation losses. For electrons it can be approximated as

$$E_{\text{crit}} = \frac{610 \text{ MeV}}{Z + 1.24}, \tag{3.2}$$

where Z is the atomic number of the medium [52].

In reality, the energy loss for any given particle generally won't precisely match the described mean value. This discrepancy arises due to statistical fluctuations in the number of collisions and the corresponding energy loss experienced by the particle. As a result, an initially monoenergetic particle beam will exhibit an energy distribution after passing through a material. The shape of the distribution depends on the absorber thickness. The total energy loss, when a particle traverses an absorber, is the sum of losses in N scatterings, each with a small, random, loss. In a thick absorber N becomes large and the central limit theorem states that for large N the sum over N obeys a Gaussian distribution [58]. In the case of thin absorbers or gases where N is small, the central limit theorem is no longer valid. As a result, the energy loss distribution becomes more complicated, and the possibility of large energy transfers in a single collision can dominate the sum. The energy loss of heavy particles is generally limited by a maximum energy transfer. The energy deposition for electrons, however, is more intricate due to the dominance of other processes, such as Bremsstrahlung, in their energy loss. Although such events of large energy loss are relatively rare, they contribute to an asymmetric form of the distribution. The presence of these events leads to a tail at the high-energy side, resulting in the shift of the mean towards higher energy values. The peak position of this distribution represents the most probable energy loss for the particles in the material [58]. The resulting energy distribution is referred to as the Landau distribution.

The Landau tail originates from delta-electrons, resulting from collisions with large energy transfer. These electrons can escape the thin layer, such as a silicon detector, leading to a discrepancy between the energy loss and deposition.

3.1.2. Interactions of Neutrons

Neutrons possess no charge and thus, do not engage in Coulomb interactions with electrons and atomic nuclei. Instead, their primary mode of interaction is through the strong force with atomic nuclei. These interactions occur less frequently due to the limited range of the strong force. Given that most of ordinary matter consists of empty space, it is not surprising that neutrons have significant ability to traverse materials, depending on their energy and the target material [1]. When neutrons do engage in interactions, they can undergo various nuclear processes depending on their energy. Among these interactions are [58]:

[1] In most materials the mean free path of neutrons is long, but there are also cases where it is not, e.g. for a thermal neutron in boron the MFP ≈ 0.1 mm.

1. The primary way neutrons lose energy in the MeV region is through elastic scattering from nuclei, denoted as $A(n,n)A$.

2. Another type is inelastic scattering: $A(n,X)B$. In these reactions, the nucleus is left in an excited state, which can later decay through the emission of gamma rays or other forms of radiation. For the inelastic reaction to take place, the neutron must possess sufficient energy to excite the nucleus, typically around 1 MeV or higher. Below this energy threshold, only elastic scattering and capture can occur.

3. Neutron capture, denoted as $A(n,\gamma)B$, for which the cross-section is proportional to v^{-1}, with neutron velocity v. Consequently, absorption is more likely at lower energies. Resonance peaks may also be present, depending on the element, in addition to this inverse velocity dependence. At the resonance energies, the probability of neutron capture is significantly increased.

4. Other nuclear reactions, such as $(n,p),(n,d),(n,\alpha)$, etc., involve the capture of neutrons and the emission of charged particles. These reactions typically occur in the MeV range. There are a few exceptions, such as $^{10}\mathrm{B}(n,\alpha)^{7}\mathrm{Li}$, which exhibit a $1/v$ dependence. This is primarily due to the significantly more favorable energetic conditions for disintegration compared to de-excitation through gamma emission.

5. Fission, denoted as (n,f). The probability of fission depends on the neutron energy and the target material.

6. Above nuclear binding energies ($\approx$ 10 MeV), the significance of nuclear structure diminishes, distinguishing it from nuclear reactions with discrete final states, described in point 2. Consequently, an intranuclear cascade emitting neutrons and protons can be generated, with the possibility of pion production above 100 MeV.

The overall probability for a neutron to interact in matter is determined by adding up the individual cross sections:

$$\sigma_{\text{total}} = \sigma_{\text{elastic}} + \sigma_{\text{inelastic}} + \sigma_{\text{capture}} + \dots \tag{3.3}$$

Due to the significant energy dependence of neutron interactions, it has become common practice to categorize neutrons based on their energy. However, specific boundaries between these classes are not strictly defined. An overview of the classification according to [58] is given in Tab. 3.1.

Slowing Down of Neutrons

When a fast neutron enters a material, it usually undergoes elastic and inelastic scattering with the nuclei, causing it to lose energy. This process continues until the neutron

[2] Technically the high-energy limit in this work is at 20 MeV, which is mainly set by having the evaluated libraries in FLUKA up to that energy.

Energy Range	Neutron Classification
$E \geq 100$ MeV [2]	High-energy neutrons
Few hundred keV - Tens of MeV	Fast neutrons
0.1 eV - 100 keV	Epithermal neutrons
Comparable to room temperature	Thermal neutrons
μeV - meV	Cold or ultra-cold neutrons

Table 3.1.: Neutron classifications based on its energy [58]. Room temperature corresponds to 25 meV.

reaches thermal equilibrium with the surrounding atoms. Once in thermal equilibrium, the neutron diffuses through the material until it is either captured by a nucleus or involved in another type of nuclear reaction, such as fission. The neutron can undergo a nuclear reaction or be captured by a nucleus before reaching thermal energies, especially if resonances are present. Elastic scattering serves as the primary mechanism for energy loss of fast neutrons. At energies in the range up to several MeV, the problem can be simplified using nonrelativistic treatment and conservation laws so that the limits of the energy of the scattered neutron can be approximated [58] as

$$\left(\frac{A-1}{A+1}\right)^2 E_0 < E < E_0, \tag{3.4}$$

with the energy before E_0 and after E the scatter event. The limits correspond to the cosines of the scattering angle $\cos\,\theta = \pm 1$. For a proton target ($A = 1$) the lower limit is zero. Thus, the lighter the nucleus, the more recoil energy it tends to absorb from the neutron. As a result, neutrons slow down most efficiently when they move through a medium containing protons or light nuclei. For this reason hydrogenous materials such as water and polyethylene are used to slow down neutrons. Also concrete serves this purpose well, since it has a lot of chemically bound water and a dense composition and therefore works also against fast hadrons.

Neutron Capture

As mentioned above, the probability of neutron capture is given by the capture cross section, which usually [3] is proportional to v^{-1} and thus increases with decreasing energy. It further depends on the target. Materials with high thermal neutron capture cross sections are for instance B, Li, Co and Ag. Fig. 3.3 shows the cross section of the neutron capture reaction

$$^{10}\mathrm{B}(n,\alpha)^{7}\mathrm{Li}, \tag{3.5}$$

[3] For instance the Ag cross section in Fig 3.3 is not proportional to v^{-1} over the full energy range

in which ^{10}B captures a thermal neutron and then decays into the stable ^{7}Li emitting an α particle. Due to their mass, the α and ^{7}Li have a high dE/dx. Upon capturing a neutron, nuclei often become unstable, as is the case for the natural occurring ^{109}Ag. When ^{109}Ag captures a neutron, it transforms into ^{110m}Ag, which is a reaction of particular significance in the context of ATLAS,

$$^{109}\mathrm{Ag}(n,\gamma)^{110m}\mathrm{Ag}. \tag{3.6}$$

^{110m}Ag is problematic in the detector because it has a half-life that is short enough to reach saturation during LHC operation but long enough to persist throughout most of an LHC shutdown. Thus, it represents a concern of radiation protection during maintenance work. ^{110m}Ag is a strong gamma emitter with cross sections for this particular reaction shown in Fig. 3.3. The cross-section for producing ^{110m}Ag is merely 4.5 b, compared to 89 b for producing ^{110}Ag. However, the half-life of ^{110}Ag is only 25 s and the emitted radiation very weak. Moreover, a minor portion of ^{110m}Ag decays through internal conversion to ^{110}Ag. Consequently, only a small fraction of the capture events result in the formation of the problematic radioisotope ^{110m}Ag.

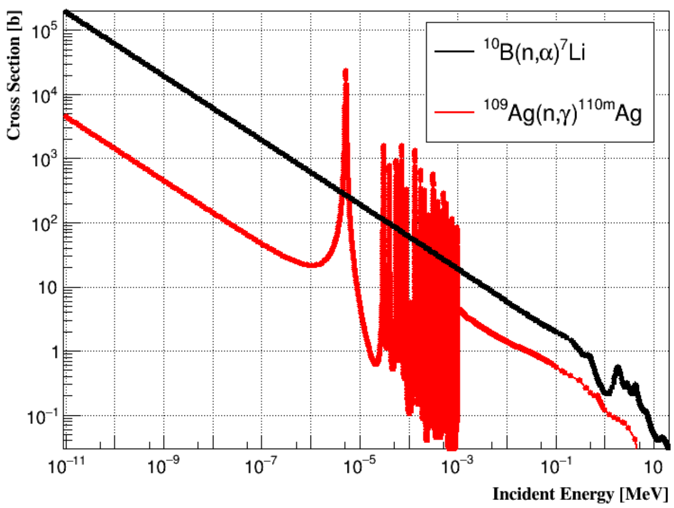

Figure 3.3.: Cross section in barns as a function of the incident neutron energy in MeV for the capture reaction $^{10}\mathrm{B}(n,\alpha)^{7}\mathrm{Li}$, in which ^{10}B captures a neutron and then decays into ^{7}Li emitting an α particle. And for the reaction $^{109}\mathrm{Ag}(n,\gamma)^{110m}\mathrm{Ag}$, in which ^{109}Ag captures a neutron and becomes ^{110m}Ag. Data taken from [59].

3.2. Simulation of Radiation Environments

Simulating radiation environments plays a crucial role in the design of new hadron collider experiments or upgrades, especially when considering higher collision energies where previous experience may not be applicable. Radiation in LHC experiments comes from proton-proton collisions, beam-gas interactions [60], and beam halo losses [61]. Monte Carlo event generators like PYTHIA8 and DPMJET-III are used to simulate these collisions [4]. For the results in this thesis PYTHIA 8 was used and is described in Section 3.2.1. Particles from proton-proton collisions interact with the detector materials, leading to complex electromagnetic and hadronic showers. Advanced Monte Carlo codes like FLUKA or GEANT4 [62] can be employed for this simulation. FLUKA was used in this thesis and is described in Section 3.2.2.

3.2.1. Event Generation

The central focus of this thesis is on FLUKA simulations. Given that particle transport simulations of the ATLAS experiment depend on the results simulated by event generators, this section provides a concise overview of the latter, focusing on PYTHIA 8 in particular.

In this context, an event is defined as a collision of two protons, producing outgoing particles that conserve energy, momentum, and relevant quantum numbers. These outcomes vary due to quantum randomness, with their probability distributions derived from data ensembles or theoretical models. Event generators are numerical algorithms that aim to predict properties of high-energy collisions and therefore rely on numerous parameters calibrated against data. These predictions serve as a valuable tool for studying the impact of new against known phenomena in experiments.

Fundamental to radiation background studies in the ATLAS experiment are simulations of pp collisions at LHC energies. In the endeavour to establish statistical robustness for the investigations in this thesis, files are generated, encompassing $50,000$ to $500,000$ events. These files are subsequently employed as input for FLUKA simulations, wherein the transport of these particles is simulated within a simplified geometry of the ATLAS detector.

The events used in this thesis are derived from PYTHIA [63] and EPOS [64] and are taken from the ATLAS Collaboration [65], respectively for Run 3 and Phase 2. Only the outcomes in Section 3.2.1 are not taken from [65], but simulated in the context of this thesis with PYTHIA 8.310. For that purpose, the default settings of that PYTHIA version were used, which are the Monash 2013 tune [66], based on a larger set of LHC distributions and the NNPDF 2.3 parton distribution functions. [63].

This section focuses on some basic properties of pp collisions, such as elastic and inelastic and single and double diffractive events and the corresponding cross sections at LHC energies.

In pp or, more generally, hadron-hadron scattering, interactions are classified by the characteristics of the final states [67]. These interactions can be either elastic or inelastic. In elastic scattering

$$p_1 + p_2 \to p_1' + p_2', \tag{3.7}$$

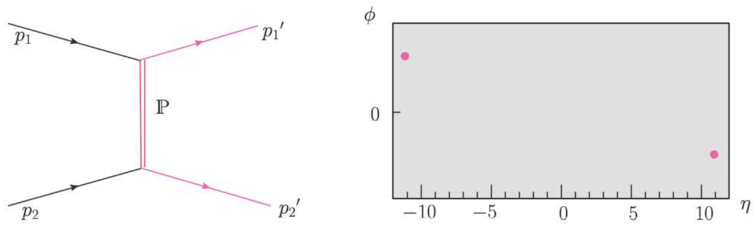

Figure 3.4.: Elastic scattering diagram (left) and a ϕ versus η plot that displays the distribution of products after the interaction (right). Taken from [67].

both protons remain intact and no additional particles are produced, depicted together with the corresponding rapidity distribution in Fig. 3.4. In this case the final and initial state particles are identical. The cross-section for elastic scattering at the LHC at $\sqrt{s} = 14$ TeV is approximately 30 mb [68].

Inelastic collisions comprise diffractive and non-diffractive processes. In diffractive scattering, the energy transfer between the two interacting protons stays small and no internal quantum numbers are exchanged. One or both protons can dissociate into multi-particle final states with the same internal quantum numbers as the colliding protons. If only one of the protons dissociates, the interaction is termed single diffractive

$$p_1 + p_2 \to p_1' + X_2 \quad \text{or} \quad p_1 + p_2 \to X_1 + p_2'. \tag{3.8}$$

The dissociated proton is shown as a spray of blue dots (particles) and the non-dissociated proton as the pink dot in Fig. 3.5.

In Fig. 3.5, the dissociated proton is represented by a spray of blue dots (particles), while the non-dissociated proton is depicted as the pink dot. Additionally, the corresponding rapidity distribution is shown. The cross-section for single diffractive scattering at the LHC at $\sqrt{s} = 14$ TeV is approximately 10 mb [68]. If both colliding protons dissociate, it is termed double diffractive

$$p_1 + p_2 \to X_1 + X_2, \tag{3.9}$$

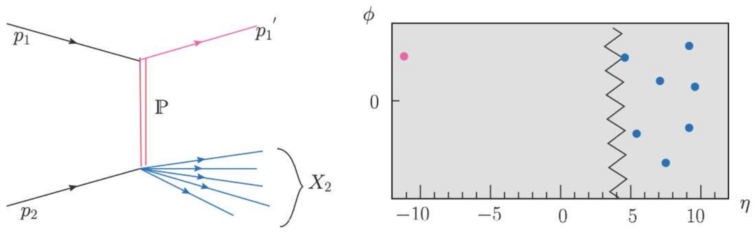

Figure 3.5.: Single diffractive scattering diagram (left) and a ϕ versus η plot that displays a rapidity gap between $-10 < \eta < 3.5$ (right). Taken from [68].

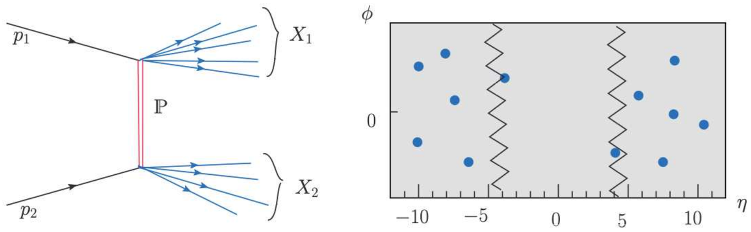

Figure 3.6.: Double diffractive scattering diagram (left) and a ϕ versus η plot that displays a rapidity gap between $-4 < \eta < 4$ (right). Taken from [67].

as depicted together with the rapidity distribution in Fig. 3.6. The cross-section for double diffractive scattering at the LHC at $\sqrt{s} = 14$ TeV is approximately 7 mb [68].

Another process is central diffraction

$$p_1 + p_2 \rightarrow p_1' + X + p_2'. \tag{3.10}$$

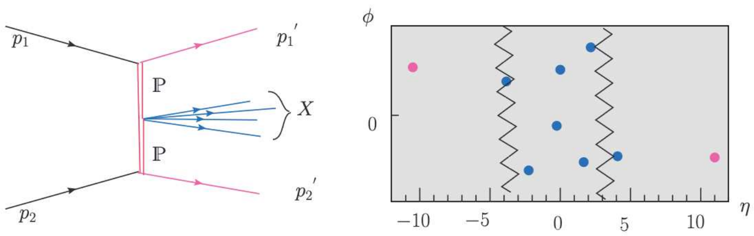

Figure 3.7.: Central diffractive scattering diagram (left) and a ϕ versus η plot that displays two rapidity gaps between $-10 < \eta < -2.5$ and $2.5 < \eta < 10$ (right). Taken from [67].

In this process, both protons remain intact and are observed in the final state (as two pink dots in Fig. 3.7 that also shows the corresponding rapidity distribution). The cross-section for central diffraction at the LHC at $\sqrt{s} = 14$ TeV is approximately 1 mb [68].

In non-diffractive interactions, there is an exchange of colour charge, leading to the production of more hadrons, as depicted in Fig. 3.8 together with the corresponding rapidity distribution. Non-diffractive interactions dominate in proton-proton interactions and are expected to constitute about 60 % of all interactions at the LHC, with a cross-section of approximately 65 mb at $\sqrt{s} = 14$ TeV [67].

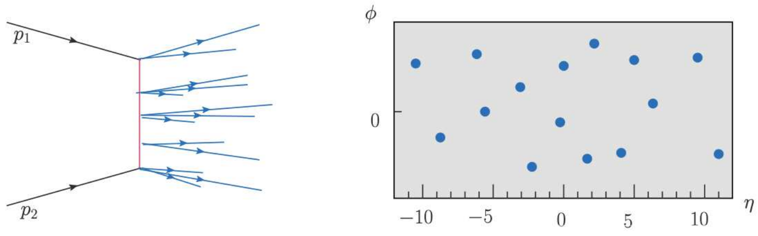

Figure 3.8.: Non diffractive scattering diagram (left) and a ϕ versus η plot that shows that there is no rapidity gap (right). Taken from [67].

The total pp cross-section is given by the sum of the scattering cross-sections described above

$$\sigma_{\text{tot}} = \sigma_{\text{el}} + \sigma_{\text{inel}} = \sigma_{\text{el}} + \sigma_{\text{SD}} + \sigma_{\text{DD}} + \sigma_{\text{CD}} + \sigma_{\text{ND}}. \tag{3.11}$$

Event generators integrate models that account for these processes. The model parameters vary based on the used parameter tune [69].

Following the initial interaction, whether diffractive or non-diffractive, partons with sufficient energy can radiate and initiate parton (quark and gluon) showers. Isolated quarks, unable to exist freely [4], combine to form color-neutral hadrons, including mesons and baryons [70].

Results in Fig. 3.9 represent final state particles, of which pions are the most frequent ones as illustrated in Fig. 3.9a and 3.9b. In Fig. 3.9a and 3.9c it is further shown, that pions have a lower p_T compared to all other particles in the graph, except $e^{\pm}$. The Rest fraction includes muons, baryons involving strange, charm and bottom quarks, such as lambdas and sigmas. Photons are excluded from the graphs and do not contribute to the Rest fraction. Fig. 3.9c further shows that as a function of η the average p_T values per η bin for hadrons peak around $\eta \approx 0$ and decrease with increasing η due to the decreasing parton density in the forward regions. Fig. 3.9b shows the expected symmetry between positive and negative η.

[4]Quarks and gluons cannot be observed in isolation but are instead found within composite particles (hadrons). This arises due to the increase in energy between quarks when they are separated, prompting the creation of new quark-antiquark pairs and the formation of bound states.

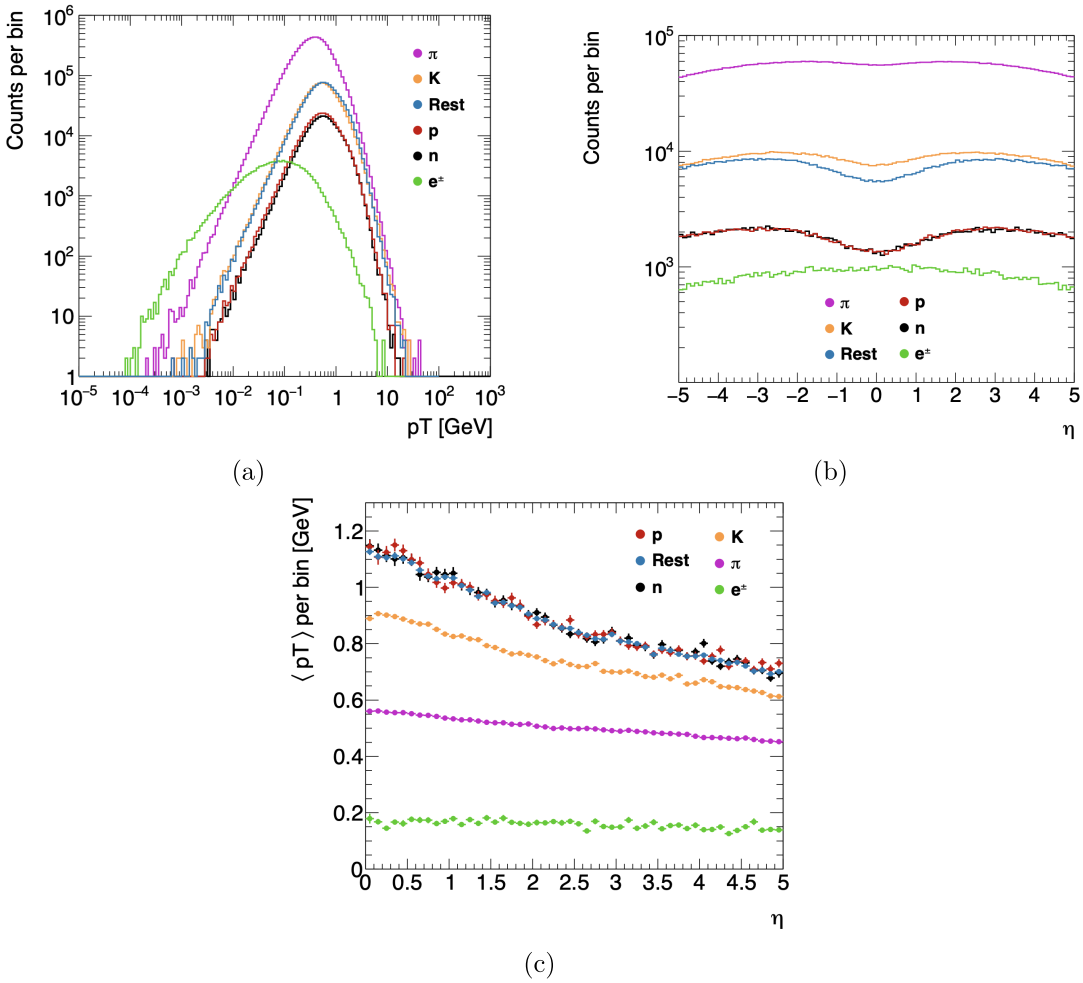

Figure 3.9.: Simulation results of a proton - proton collision at 13 TeV with PYTHIA 8 using default settings. Shown are final state particles separated in neutrons, protons, all types of pions, all types of kaons, electrons & positrons, and remaining particles summed up in 'Rest', except for photons, which are not recorded.

3.2.2. Particle Transport with FLUKA

The FLUKA code [5–7] is widely used for studying high-energy particle-induced hadronic and electromagnetic cascades. It serves as the fundamental tool for simulating radiation backgrounds, in particular at CERN and LHC experiments. FLUKA allows to simulate interactions and transport of electrons, photons, muons up to 1000 TeV, and hadrons up to 20 TeV. For low-energy neutrons, the lower transport limit extends to thermal energies. Anti-particles, heavy ions, and residual nuclei production are also included. FLUKA employs a microscopic physics model whenever possible and ensures conservation laws at each interaction step. The accuracy of its results is verified against experimental data at the individual interaction level. This approach relies on a minimal set of fixed parameters applicable to all projectile energies and target materials. Consequently, FLUKA simulations offer good reliability when extrapolating to complex scenarios without available experimental data, preserving correlations within interactions and shower components [4].

FLUKA's comprehensive physics models and capabilities are extensively described in references listed in [5]. The model used for inelastic hadron collisions varies with energy. Above 5 GeV for inelastic hadron-hadron interactions, the dual parton model (DPM) [71] is employed, while below 5 GeV, the resonance production and decay model [72] is used. For inelastic interactions between hadrons and nuclei up to 100 TeV the pre-equilibrium-cascade model PEANUT [73, 74] is utilised by default.

The neutron transport in FLUKA is separated in two energy regions. Neutrons with energies above 20 MeV are transported using continuous cross-section tabulations, whereas for low-energy neutrons, FLUKA employs a multigroup algorithm. The idea behind multigroup transport is that cross sections are defined as fluence (ϕ) weighted avereages

$$\overline{\sigma} = \int_{E_{\mathrm{min}}}^{E_{\mathrm{max}}} \sigma(E)\phi(E)dE, \tag{3.12}$$

with the actual cross section $\sigma(E)$ at energy E. The challenge with group wise cross sections arises from the non-universality of the fluence spectrum. When evaluated for a specific fluence spectrum, the cross section is exact only for that spectrum, while for others, it becomes an approximation. As the group widens, its accuracy decreases. Certain neutron transport codes use point wise cross sections, which necessitate extensive tables of σ values. Also in FLUKA versions 4-3.0 and newer, it can optionally be applied. The point wise cross section approach doesn't assume any specific fluence in the simulated problem, making it generally more accurate and applicable to various scenarios. However, it's essential to acknowledge that the point wise cross sections themselves are derived from experimental neutron irradiation data, assuming a certain neutron spectrum ($\phi(E)$) for that particular experiment. Deconvoluting a neutron spectrum from measured data is challenging, leading to errors in the point wise cross sections that might not necessarily be smaller than those in the group wise cross sections [75].

The point-wise cross section library, available in FLUKA 4-3.0, is the same as the default one used in GEANT4, and can be found in [76]. In Section 6.2.7, the outcomes of group-wise and point-wise transport simulations in FLUKA and GEANT4 (point-wise only) for the inner detector of the Phase 2 upgrade (ITk) are evaluated.

3.2.3. Fluxes, Fluences and Doses

This section provides fundamental definitions of physical quantities employed in presenting the results. A fundamental quantity in most radiation calculations is the flux density which can be defined as the track length per unit volume per unit time [52]. Thus, the unit can be expressed as m^{-2} s^{-1}. The fluence is the time integral of the flux density and thus given by

$$\Phi = \frac{dl}{dV}, \tag{3.13}$$

where dl is the sum of the particle trajectory lengths in the volume dV.

For numerous investigations in this thesis, thermal neutrons are particularly significant. In describing the energy distribution of particles in a system at thermal equilibrium, as governed by the Boltzmann distribution, it's important to note that particles exhibit a range of energies. For practical purposes, it is often useful to introduce a single representative value for the integrated thermal fluence. For the entire thesis the following definition is used:

$$\Phi_{\text{th}} = \int \frac{\sigma(E) \times \Phi(E)}{\sigma_{\text{th}}} dE \tag{3.14}$$

where $\sigma(E)$ represents the capture cross section of ^{10}B for a neutron with energy E, $\Phi(E)$ the total neutron fluence and σ_{th} the capture cross section of ^{10}B for a neutron with 0.025 eV.

Another type of fluence particularly essential for studies of silicon damage is the Si 1 MeV neutron equivalent fluence $\Phi^{\text{Si}}_{n_{eq}}$ and is described in Section 4.2.

Dose is defined as absorbed energy per unit of mass and is expressed in Gy $(= \frac{\text{J}}{\text{kg}})$. Doses have no universal one-to-one relationship to fluences.

4. Silicon Particle Detectors

4.1. Semiconductor Physics

In a lattice structure, the closely bound atoms exhibit overlapping orbits, causing the energy levels of individual atoms to split into two distinct bands known as the valence band and the conduction band. The valence band is comprised of electrons tightly bound to the atoms, while the conduction band allows electrons to move throughout the material. The energy difference separating the conduction band from the valence band is commonly referred to as the band gap. In thermal equilibrium, the probability of a particular energy state E being occupied at a temperature T is determined by the Fermi-Dirac statistics, incorporating the Pauli exclusion principle as

$$f(E,T) = \frac{1}{e^{(E-E_f)/(k_B T)} + 1}. \tag{4.1}$$

k_B represents the Boltzmann constant and E_F is the Fermi energy or Fermi level which can be regarded as the energy where exactly half of the available levels are occupied, usually in the middle between the valence and conduction band. The band gap size is a characteristic that allows for the classification of materials. In conductors, the valence and conduction bands overlap, facilitating the unrestricted movement of electrons between atoms and resulting in their high conductivity. Insulators, on the other hand, possess a significant band gap of more than 3 eV, separating the valence and conduction bands. Semiconductors typically exhibit a band gap smaller than 3 eV, making it easier for electrons in the valence band to transition to the conduction band through excitation. As an electron transitions to the conduction band, it creates a vacancy in the valence band known as a hole, which can freely move and carry a positive charge. This hole can be filled by another electron in a process called recombination. In the absence of impurities and at low temperatures, the valence band of a semiconductor such as silicon, is fully occupied while the conduction band remains unoccupied. To modify the conductivity behaviour and thus shift the Fermi level, additional states can be introduced within the band gap through a process known as "doping".

Silicon, having four valence electrons, can have its free charge carrier concentration modified by introducing impurities. By adding materials with 5 valence electrons such as phosphorus (donor impurity), "n-type" silicon can be produced, resulting in an excess of electrons as the majority charge carriers. On the other hand, by adding materials with three valence electrons like boron, "p-type" silicon can be assembled, leading to a deficiency of electrons and the presence of holes as the majority charge carriers [77].

When the n-type and p-type silicon are brought together, they form a pn-junction. In this arrangement, the majority of charge carriers in each region are attracted to their oppositely charged counterparts. As a result, electrons and holes begin to diffuse and recombine within the p-type or n-type silicon. This process causes a buildup of charge, resulting in a negative charge in the p-type silicon and a positive charge in the n-type silicon as illustrated in Fig. 4.1. With the charge carriers diffused away, a space charge region (SCR) is developed, in which only the ionised donor or acceptor impurities are left behind.

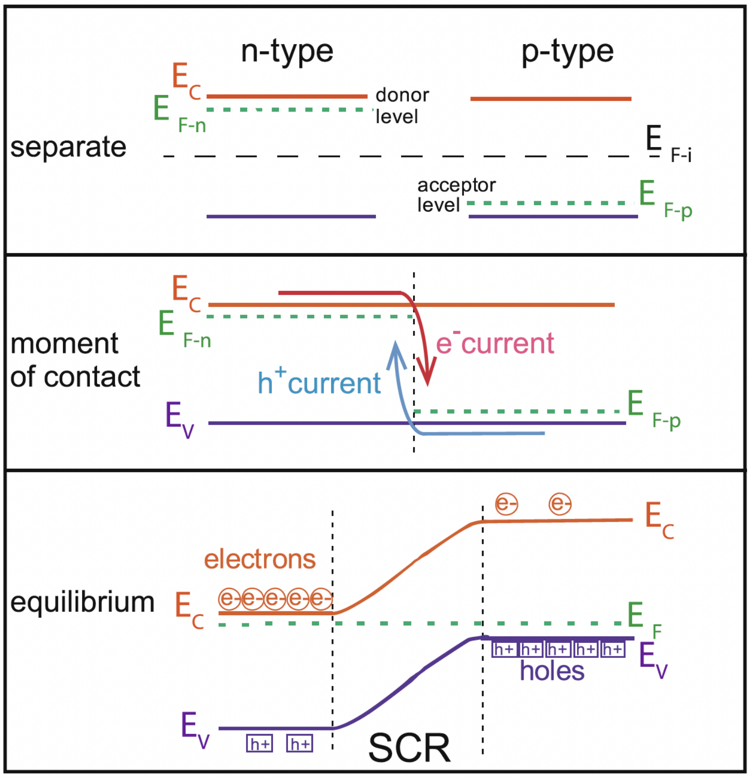

Figure 4.1.: On the top graph separate band diagrams for the p-type and n-type regions, indicate their respective Fermi levels (E_{F-n} and E_{F-p}). The dashed line represents the position of the Fermi level (E_{F-i}) in an intrinsic semiconductor. In the graph in the middle, the two parts are connected, causing electrons to migrate towards the region with the lower Fermi energy, and holes to migrate towards the region with the higher Fermi energy. On the bottom graph the state of equilibrium is illustrated, where a space charge region (SCR) is established, leading to a shift in potentials and ensuring that the Fermi energy remains constant across the entire system. From [77].

An external voltage increases or decreases the width of the SCR, depending on the polarity. Silicon sensors are operated in reverse bias mode, in which the SCR increases and eventually covers the entire volume. The depletion width w is given as

$$w = \sqrt{2\varepsilon_0 \varepsilon_{\mathrm{Si}} \mu \rho V} \tag{4.2}$$

depending on the resistivity ρ (measure of silicon purity), the mobility μ of majority charge carriers (measure of the rate and facility with which charge carriers can traverse a material in response to an applied electric field) and the external voltage V. In reverse bias mode the diffusion across the pn junction is suppressed and the current across the junction is very small. The diffusion current is generated at the edge of the depletion region and is negligible for fully depleted detectors. The generation current (also called leakage current) is generated from thermal induced electron / hole pairs in the depletion region and strongly depends on the temperature.

4.2. Radiation Damage Effects

This section provides an overview of the impact of radiation on silicon detector systems. The section is structured into two main categories: sensors and electronics. Although the underlying physics of energy loss is similar in both categories, the specific radiation parameters used to assess damage often differ. For instance, sensor radiation studies primarily investigate the consequences of bulk displacement damage, while electronics degradation primarily centres on ionising dose effects [16].

4.2.1. Impact of Defects on Silicon Sensors

In a semiconductor displacement damage causes new energy levels within the bandgap, which alter the device's functionality and characteristics by three main effects. In general the impact of each depends on the capture cross sections for holes σ_p and electrons σ_n, the position in the bandgap, the type of defect (acceptor or donor), and the concentration of the defect N_t [16].

Leakage Current

Leakage current primarily arises from defect levels positioned near the midpoint of the bandgap. An increase in leakage current leads to increased noise in amplifiers and higher power consumption. As leakage current is temperature-dependent and increases exponentially with rising temperatures, cooling proves highly effective in reducing these adverse effects [16]. In order to calculate the leakage current, it is necessary to ascertain the defect occupancy with electrons f_t is defined as

$$f_t = \frac{c_n n + e_p}{c_n n + e_n + c_p p + e_p}, \tag{4.3}$$

where c_n and c_p are the capture coefficients for electrons and holes, n and p are the electron and hole densities, and e_n and e_p are the emission rates for electrons and holes. c_n is given by $c_n = \sigma_n v_{th,n}$ with $v_{th,n}$ being the thermal velocity for electrons, and e_n is given by $e_n = c_n n_i \exp(E_t - E_i/k_B T)$ with n_i being the intrinsic carrier density, E_i is the intrinsic Fermi level, E_t represents the energy level associated with a specific defect within the bandgap, T is the temperature, and k_B is Boltzmann's constant [16]. In the depletion region of a detector, the carrier densities are very low and can often be neglected so that Eq. (4.3) becomes

$$f_t = \frac{e_p}{e_n + e_p}. \tag{4.4}$$

Defect levels contribute to leakage current by emitting electrons and holes, facilitating the transfer of electrons from the valence to the conduction band. The generation rate G_t for a specific defect type t, assuming negligible free carrier concentrations, can be calculated according to [16] as

$$G_t = N_t f_t e_n = N_t(1 - f_t)e_p = N_t \frac{e_n e_p}{e_n + e_p}. \tag{4.5}$$

By summing the contributions from all defect types and considering the active volume of the sensor (depletion width ω and area A), the total device leakage current can be derived as

$$I = q_0 \omega A \sum_{\text{defects}} G_t, \tag{4.6}$$

with q_0 representing the elementary charge [16].

Effective Space Charge

Radiation-induced changes in sensor materials can modify the effective space charge, shifting the electric field distribution and depletion voltage within the device. Such shifts may necessitate higher operational voltages to maintain performance, risking underdepletion and signal loss. Non-uniform space charge distribution can lead to undesired effects, while the impact of radiation damage depends on material characteristics and particle type. Defect engineering, like impurity content adjustment, can mitigate these effects, as defects introduce positive or negative charges, altering the electric field distribution and device behavior. The effective space charge N_{eff} (neglecting free carriers) is then given by the sum of all positively charged donors N_D and all negatively charged acceptors N_A.

$$N_{\text{eff}} = \sum_{\text{donors}} (1 - f_t) N_t \; - \sum_{\text{acceptors}} f_t N_t, \tag{4.7}$$

where the index t is running over all donor and acceptor such as defect types t with concentration N_t [16].

Trapping

Ionising particles or photons in the depletion region create charge carriers that constitute the sensor's signal. However, defects within the sensor can trap these charge carriers. When the trapping time is significantly longer than the collection time, or if there's a high concentration of trapping centers, the sensor's overall signal is diminished. Trapping becomes a limiting factor, particularly in high-fluence applications. This issue can be addressed through device modifications aimed at reducing collection times (device engineering). In segmented sensors, collecting electrons instead of holes at the sensing electrodes can be advantageous, leveraging the higher electron mobility and the potential for charge multiplication via impact ionisation at lower electric fields, without risking device breakdown. The trapping is characterised by a trapping time (inverse capture rate) τ_e for electrons and τ_h for holes that are calculated as

$$1/\tau_e = c_n (1 - f_t) N_t \;\text{ and }\; 1/\tau_h = c_p f_t N_t. \tag{4.8}$$

Summing over all defects contributing to the trapping results in the effective trapping times τ_{eff} for electrons and holes

$$\frac{1}{\tau_{\text{eff},e}} = \sum_{\text{defects}} c_{(n,t)} (1 - f_t) N_t \tag{4.9}$$

$$\frac{1}{\tau_{\text{eff},h}} = \sum_{\text{defects}} c_{(p,t)} f_t N_t \tag{4.10}$$

4.2.2. Non-Ionising Energy Loss

High energy particles, traversing material, experience ionising and Non-Ionising Energy Loss (NIEL). The ionising energy loss, caused by the charge of a particle, is responsible for the generation of electron-hole pairs. The NIEL, caused by momentum transfer from the particle to atoms of the medium, displaces atoms from their positions in the crystal lattice. The energy of an incident particle can be high enough to displace several atoms, which themselves displace further atoms on their way through the crystal [82]. Only a fraction of the NIEL yields displacement damage, since a part of the energy dissipates in phonons. This fraction depends on the energy of the impinging particle. Defined in MeVcm^2/g or as NIEL cross section in units of MeV·mb, it is also referred to as displacement damage function D. The Si [1] 1-MeV neutron equivalent (neq) fluence has been fixed to 95 MeV·mb as reference value [16]. In Fig. 4.2, commonly used values of NIEL cross sections for different particles are illustrated.

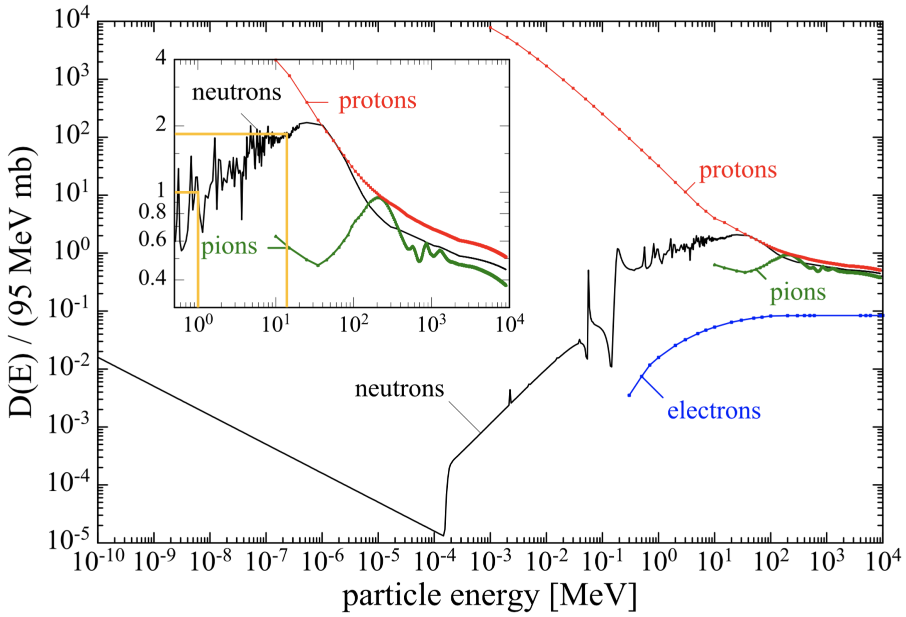

Figure 4.2.: NIEL cross sections normalised to 95 MeV·mb. Data collected by A. Vasilescu and G. Lindstroem [11] and based on [12–15].

The displacement damage from different particles with different energies can be related by the NIEL scaling hypothesis which is based on the assumption that the radiation damage effects scale linear with the NIEL irrespective of the type or energy of the particles involved in the interaction.With the displacement damage function the Si 1-MeV neutron-equivalent fluence $\Phi^{Si}_{n_{eq}}$ of different radiation fields can be calculated. For

[1]The NIEL cross section depends on the particle, but also on the target material and that target dependence is not the same for all particle types, i.e. the 1MeV n equivalence itself is target-dependent.

instance the orange lines in Fig. 4.2 indicate that a 14 MeV neutron produces 1.8 times more displacement damage in silicon than a 1 MeV one. [11]. The displacement damage functions shown in Fig. 4.2 are presently used to calculate the 1 MeV neutron equivalent fluence radiation fields in the experiments of the LHC and HL-LHC [16].

4.2.3. Impact of Defects on Electronics

This section delves into radiation-induced effects on silicon-based electronic systems in the context of the HEP experiments. For this matter, three effects are discussed, namely Total Ionising Dose (TID) effects, Single Event Effects (SEE) and NIEL effects.

Total Ionising Dose Effects

This form of damage accumulates gradually, resulting in the deterioration and potential failure of electronic devices. TID damage is associated with the buildup of trapped charge states within an oxide layer or at the oxide–bulk interface. This accumulation leads to alterations in the device's electric fields, affecting its electrical characteristics. In the case of metal-oxide-semiconductor (MOS) transistors, TID primarily influences critical parameters, including the threshold voltage, charge mobility, and leakage current. The measurement of TID is quantified in Gray (Gy), and values observed in the ATLAS experiment can range from a few Gy to several MGy [4].

Single Event Effects

Single event effects (SEEs) encompass a range of radiation-induced disturbances within electronic circuits, which can be triggered by the transit of a single particle through the device [78]. These include single event upset (SEU), single event latch-up (SEL), single event gate rupture (SEGR), and single event burnout (SEB). For practical classification, SEEs can be grouped according to their impact on a system [4]:

Soft SEEs (or soft SEUs): These are radiation-induced bit flips that corrupt data or system configurations. They are not permanent effects and can be addressed by resetting the system or rewriting data in memory. For instance, a '1' can change to '0' (or vice versa) in a combinatorial logic circuit, register, or memory.

Hard SEEs (or hard SEUs): These are radiation-induced bit flips that permanently corrupt data or system configurations, such as a bit stuck at '1' in a memory cell.

Destructive SEEs (SELs, SEBs, SEGRs): These lead to permanent damage. SELs are destructive SEEs, unless a robust architectural solution protects the circuit against thermal destruction resulting from latch-up. SEBs and SEGRs are invariably destructive SEEs, typically affecting high-power and/or high-voltage circuits.

SEEs are the result of a single particle depositing a significant amount of ionising energy within a small, sensitive region of the chip. For SEUs, this sensitive region is typically the drain of a transistor, and the amount of charge required for such an event is smaller than that needed for destructive SEEs. Due to the small size of the sensitive region, only particles with high linear energy transfer (LET) can trigger an event. In the Complementary Metal Oxide Semiconductor (CMOS) generations employed in LHC experiments, only nuclear fragments resulting from hadronic collisions of incoming particles (protons, neutrons, pions) with atoms composing the circuit can generate sufficient charge deposition. These fragments have a limited range of only a few micrometers in silicon and must be produced very close to the sensitive region [79].

As integrated circuits continue to feature smaller dimensions and lower operating voltages, they become increasingly sensitive to smaller amounts of deposited charge. In contrast to that, with the shrinking of sensitive areas inside the chips, the probability that a fragment hits the sensitive region deceases. Further, when a smaller sensitive region (in the order of μm) is hit, only a fraction of the ionisation is deposited. Thus, below a critical size ($\sim$ fragment range) a reduction of the sensitive region reduces both, the probability of being hit and the fraction of energy deposited. Consequently, the occurrence of SEUs per unit of data stored in the chip tends to decrease with shrinking feature sizes.
However, there is an additional consideration: with reduced energy needed to cause disruptions, the chips may be more sensitive to even minor disturbances, such as those from low-energy particles. Additionally, although individual parts of the chip are less likely to be affected, the higher density of components in smaller chips means that the overall risk of disruption for the entire chip increases significantly [4].

Besides high-energy hadrons, thermal neutrons can significantly impact soft error rates of electronic devices. Neutrons above a few MeV (and even below for elastic processes) can indirectly ionise the atoms of the sensitive region through elastic and/or inelastic reactions, depending on the initial particle energy and target material. In contrast, thermal neutrons are absorbed by the ^{10}B isotope, still present inside the structure of the device, causing the reaction ^{10}B(n, α)^{7}Li, mentioned in Section 3.1.2. The ^{7}Li and the α particle can ionise the silicon atoms, collecting charge in the sensitive region, triggering SEU. Therefore, thermal neutron sensitivity in electronics depends on the ^{10}B content in the device. Despite being avoided in recent technologies, ^{10}B persists in electronic devices because of its use in p-doping and tungsten coatings [80].

Non-Ionising Energy Loss Effects on Electronic Devices

NIEL effects can induce changes in the electrical and optical properties of electrical devices. The accumulation of NIEL-induced defects leads to various outcomes, including heightened leakage currents and modifications in effective doping concentrations. CMOS devices typically exhibit a lower sensitivity to NIEL effects compared to TID effects, primarily due to their high level of majority charge carrier doping. However, in specific MOS devices characterised by low-doping features, such as laterally diffused MOS (LDMOS), the influence of NIEL can assume a significant role. Bipolar electronics generally display greater sensitivity to bulk defects compared to CMOS technology [4].

5. Monte Carlo Simulations of the ATLAS Detector

5.1. Implementation of the ATLAS detector in the FLUKA Framework

The FLUKA Monte-Carlo simulation program has been used for radiation simulations at CERN for more than 40 years and for the ATLAS detector since its construction in the early 90ies. The description of the detector geometry has evolved and has been refined over the years, but the FLUKA model remains an approximation of the actual detector layout. The results obtained from the simulations have played a key part in the design of the ATLAS radiation shielding, in the prediction of radiation levels and in studying radiation damage in detector components.

5.1.1. Description of the Geometry and the Magnetic Field

The geometry description is in constant development and therefore available in different versions. For the simulation studies in this thesis one geometry is used that represents the current Run 3, and one the Phase 2 geometry of the ATLAS future upgrade. The latter differs for instance by the ITk replacing the ID and the new VAX.
The symmetry of ATLAS allows the entire detector's geometry, except for some parts of the Cavern, to be modeled exclusively in the $+z$ direction and to be reflected into $-z$. Fig. 5.1 presents a cross-sectional view of the ATLAS FLUKA geometry, illustrating only one quadrant, as the geometry is further symmetric in the azimuthal angle Φ.

FLUKA enables the use of arbitrarily complex magnetic fields. During the propagation of a charged particle within a magnetic field, the actual trajectory is approximated by linear segments. A correction is then applied to account for the accurate curved path length, ensuring precise calculations of energy loss and interaction probability. The implementation of the ATLAS magnetic field in FLUKA can be accomplished through a user-defined routine. This routine reads the B_r, B_ϕ, and B_z components from a 2D field map and returns the field components based on each particle's current position and region.

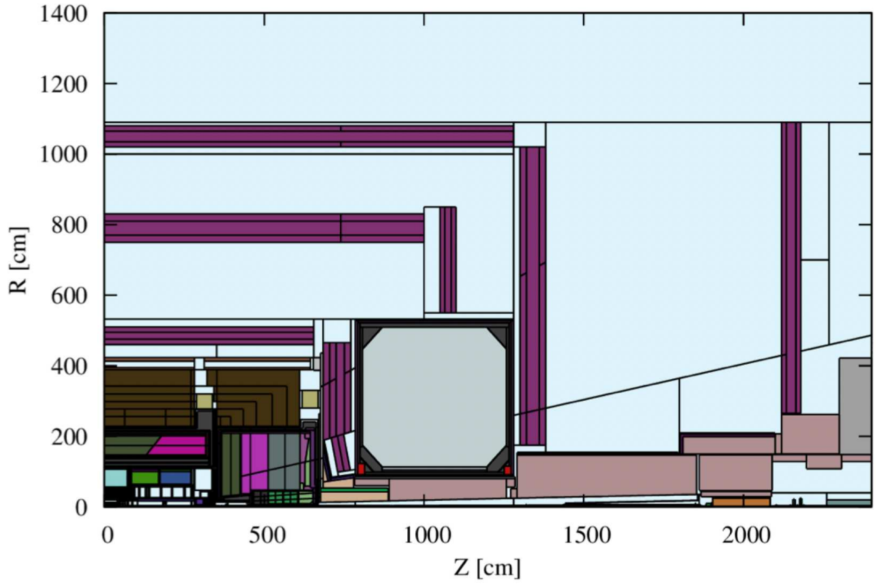

Figure 5.1.: Cross-sectional view of the ATLAS geometry as implemented in FLUKA. Only one quadrant is illustrated, as the geometry is mirrored in the longitudinal $-z$ direction and symmetric in azimuthal angle Φ.

5.1.2. Simulation Settings

In order to obtain accurate results, as presented in subsequent chapters, the precision of FLUKA simulations was controlled by a range of distinct settings. These settings were adjusted to achieve the best possible tracking accuracy within a reasonable CPU time, as outlined below.

- Detailed transport of electrons, positrons, and photons, encompassing the simulation of electromagnetic cascades, which includes the incorporation of Rayleigh scattering and inelastic form factor corrections to Compton scattering and Compton profiles.
- Particle transport threshold set at 100 keV, except for neutrons which are transported down to thermal energy levels
- Handling of low-energy neutron transport spanning from 20 MeV down to thermal energies
- Generation of δ-rays with a lower production threshold of 100 keV
- Restricted ionisation fluctuations (continuous slowing down approximation) for hadrons, muons, and electromagnetic particles below the δ-ray threshold
- Pair production initiated by heavy particles with explicit generation of $e\pm$ pairs

- Transport of heavy fragments

5.2. Enhancing FLUKA Simulations of ATLAS through New Binning Techniques

As previously mentioned, the MC simulation methods for ATLAS are in constant development. In the context of this thesis, the FLUKA geometry has been thoroughly refined and updated. Additionally, new recording (binning) techniques have been implemented in the FLUKA code. The development of these features was inspired by the user-friendly interactive tools introduced in [81], which significantly improve the visualization of Geant4 simulation results for the various radiation maps in the ATLAS experiment. These advancements motivated the implementation of similar tools in FLUKA to enhance its capabilities in recording and visualizing simulation data. These html-based tools enable users to examine particle fluence, energy spectra, time dependent TID and the compositions of detector materials at various locations within the experiment. The visualization tool relies on simulation results that are organised into customised spatial bins. This section describes the implementation of such a binning in the FLUKA code.

5.2.1. Implementation of Energy Spectrum and TID time distribution in the FLUKA Code

Extracting energy spectra with spatial binning from a FLUKA simulation is not straightforward, as the default recording methods of spectra are restricted to FLUKA Regions [1]. This issue can't be solved by the usage of standard user routines, since these give access only at the end of each step and that is either at an interaction or at a region boundary, as illustrated in Fig. 5.2. Since these region boundaries are defined by the geometry design, they do not necessarily align with the spatial binning grid. The desired output cannot simply be achieved by modifying the existing scoring routine of FLUKA, such as with the FLUSCW routine [2]. In order to bypass these issues and implement spatial binning, it is required to modify the source code of FLUKA, to find, record and print the tracklength information when entering and exiting each bin, irrespective of the geometry.

For the implementation of spatial binning in FLUKA two key routines are essential: KASKAD and USRSCO. KASKAD steers the particle transport and calls the tracklength scoring, which is implemented in USRSCO. Within the latter the new dedicated routine for binned spectrum scoring subroutine is called. This implemented subroutine takes inputs such as tracklength, location (e.g., r and z bins), and additional information like energy and particle age. Subsequently, an additional output routine, called from USROUT, prints the results into a separate output file.

To initialise the customised scoring, the default scoring card USRSBIN is utilised to

[1] The concept of Regions within FLUKA is described in Section A.1

[2] Essential subroutines are described in Section A.2

define the binning which has to match the binning that is defined in the spectrum scoring routine. USRBIN is also used to select the particle (group). For example, when selecting the neutron particle type, the energy spectrum of neutrons is recorded. For time-dependent scorings, it is possible to either select a particle (group) to obtain the time-dependent tracklength of that particle (group), or select energy deposition to obtain the time distribution of the dose. Additional parameters such as number of bins and limits for energy and time are specified in an include file.

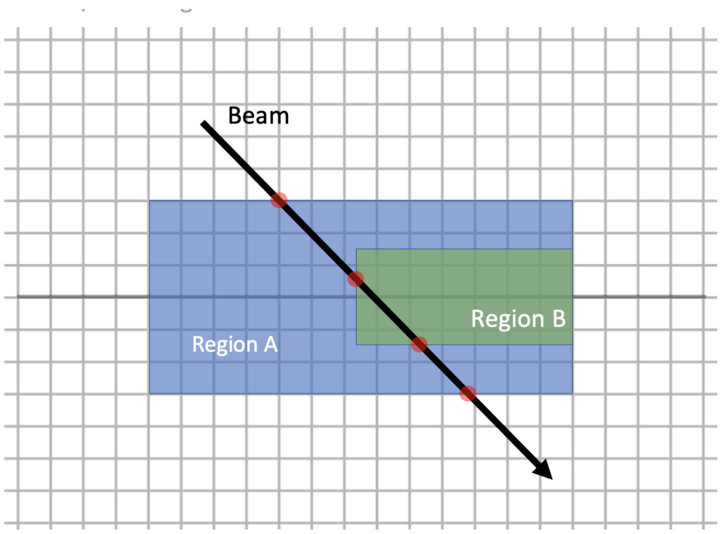

Figure 5.2.: Illustration of a particle beam (black) passing through two distinct FLUKA Regions. Red dots mark the locations where normal user access is given (e.g. FLUSCW is called), while the beam intersections with the grey grid indicate the desired spatial binning locations. Even though the last red point aligns with the binning it would deposit too much, since it takes the full tracklength between the two red points and not only that in the last bin crossed.

Fig. 5.3 illustrates the particle fluences as a function of kinetic energy within a single bin situated inside the ITk volume of ATLAS. Neutrons are tracked down to thermal energies, while all other particles are tracked down to 10 keV. Generally, neutrons and photons dominate the fluence, with the exception being the innermost regions of ATLAS where primary particles from collision events are the most abundant. In Fig. 5.3, the normalization is represented as $0.2 \times d\Phi/d\log_{10}(E_{\mathrm{kin}}/\mathrm{MeV})$. This normalization is convenient for the interactive tool as it facilitates the direct summation of energy-binned fluence values (with a bin size of 0.2 in $\log_{10}(E_{\mathrm{kin}}/\mathrm{MeV})$), resulting in the total fluence.

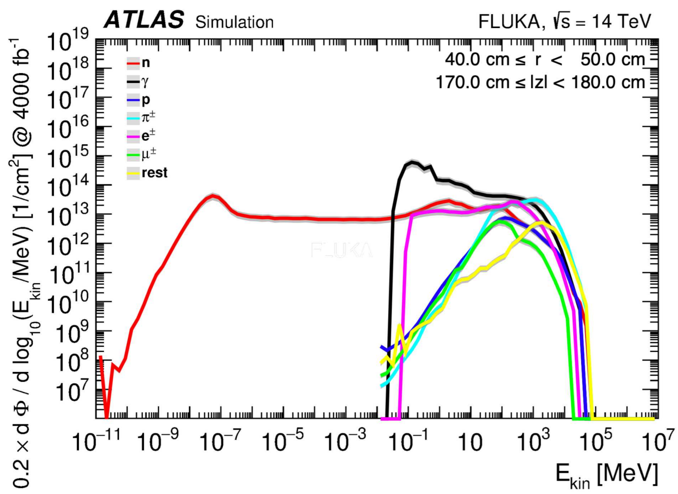

Figure 5.3.: Particle fluences for neutrons, protons, electrons (and positrons), photons, muons (and anti-muons), charged pions and all other particles as function of their kinetic energy from a FLUKA simulation of the ATLAS detector setup of Phase 2 with $\sqrt{s} = 14$ TeV normalised to a cross section of $\sigma_{\text{inel}} = 79.31$ mb and an integrated luminosity of $L = 4000\ \text{fb}^{-1}$. Neutrons are shown for all energies down to 10^{-11} MeV, while the other particle spectra start at 10^{-2} MeV. These spectra represent a specific position within the inner detector, with the gray bands serving to represent the associated statistical uncertainties.

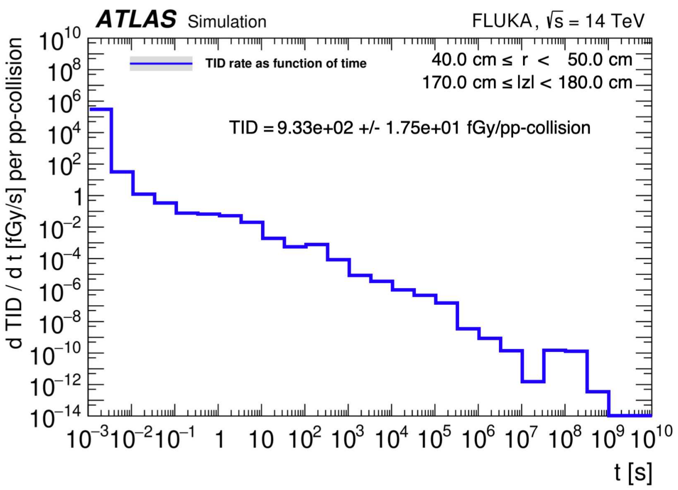

Figure 5.4.: TID rate per pp-collision from a FLUKA simulation of the ATLAS detector setup of Phase 2. The time bins grow logarithmically and the ratio of bin boundaries is constant: $t_{\text{up}}/t_{\text{low}} = 10^{0.5}$. This spectrum represents a specific position within the inner detector.

Fig. 5.4 shows the TID rate per pp-collision. The time bins grow logarithmically and the ratio of bin boundaries is constant: $t_{up}/t_{low} = 10^{0.5}$. The first bin reports the average dose rate for the first 3.16 ms after the time of the pp collision event (no lower boundary) and the last bin the average rate between 100 and 317 years after (with upper boundary). This time distribution can be folded with a luminosity profile to predict the TID rate after any arbitrary periods of running and cooling [81].

5.2.2. Verification of the Customised Scoring

To verify the results of the customised scoring, several tests were conducted before adding energy and age information. This comparison was performed across different scoring types, such as X-Y-Z scoring and R-Z scoring, initially using simple geometries and later incorporating the full ATLAS geometry. The geometries of a basic test for the R-Z scoring are shown in Fig. 5.5 and 5.6. Fig. 5.5 depicts the geometry used for testing energy-integrated tracklength scoring in the z direction. For this purpose, three z bins of 10 cm were implemented, so that the region boundaries of the target do not align with the binning. The cylindrical target consists of vacuum, since its purpose is simply to verify the position and outcome of the scoring. The implemented routine records each tracklength scoring with the corresponding z bin. The results are shown in Tab. 5.1. As expected, the tracklength is scored according to the binning and at each region boundary. The correctness of the scoring is immediately visible by comparing Fig. 5.5 and Tab. 5.1 where the total tracklength in each bin adds up to the correct value of 10 cm.

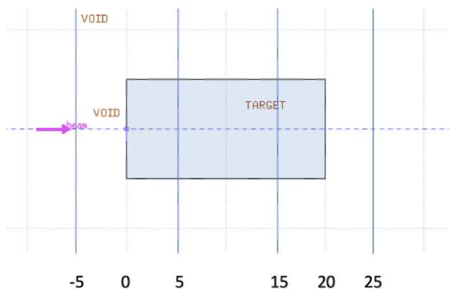

Figure 5.5.: Vacuum target with z bins (blue lines) and beam direction (pink arrow). Axes values in cm.

z Bin	Tracklength
1	5 cm
1	5 cm
2	10 cm
3	5 cm
3	5 cm

Table 5.1.: Results for the z direction of the implemented R-Z scoring.

A similar test was applied for the r direction. Fig. 5.6 shows the corresponding geometry with three r bins of 4 cm. In this scenario the beam direction is towards r and the beam starts on the inside of a hollow cylinder. The results for the r direction are presented in Tab. 5.2, confirming that the tracklength scoring is consistent with the binning and

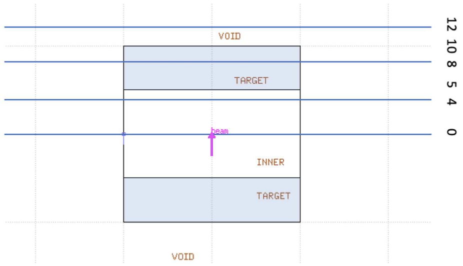

Figure 5.6.: Vacuum target with r bins (blue lines) and beam direction (pink arrow). Axes values in cm.

r Bin	Tracklength
1	4 cm
2	1 cm
2	3 cm
3	2 cm
3	2 cm

Table 5.2.: Results for the r direction of the implemented R-Z scoring.

region boundaries, as seen by comparing Fig. 5.6 and Tab. 5.2.

To test the scoring for complexer geometries and eventually the full ATLAS geometry the energy-integrated tracklength scoring was directly compared with FLUKA's standard scoring, yielding identical results.

Subsequently, energy was introduced as an additional dimension to obtain energy spectra instead of only fluences. This enhancement was also validated by comparing it with a standard FLUKA scoring of energy spectra, achieved by designing Regions comparable to spatial bins. This extended binning also proved to be successful.

To test the time-of-flight scoring, a cylindrical target with $R = 10$ cm and $z = 20$ cm composed of the stable isotope ^{59}Co is irradiated with thermal neutrons. Due to the high capture cross sections of thermal neutrons radioactive ^{60}Co isotopes are formed. A suitable age binning method is employed to plot the exponentially decreasing tracklength of the gamma particles in Fig. 5.7. An exponential fit is employed, and the slope of the fit corresponds to the half-life time of ^{60}Co (1.66×10^8 s), proving that the implemented binning method works.

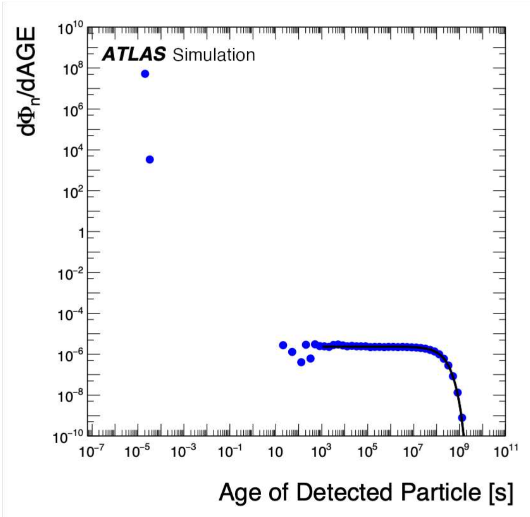

Figure 5.7.: Time distribution of gamma particles after irradiating ^{59}Co with thermal neutrons, so that the radioactive isotope ^{60}Co is formed. The two blue points around 10^{-5} s are from the prompt radiation. The remaining points indicate the exponential decay of ^{60}Co. The black line represents an exponential fit with a slope of $1.66E{+}08$ s, i.e. the half-life time of the radioactive cobalt isotope.

5.2.3. Implementation of Material Binning in the FLUKA Code

For Geant4 geometries, a material density map has been developed using non interacting particles. These are referred to as geantinos and serve to examine all detector volumes with the focus on the material properties encountered along the tracks [81]. To achieve equivalent results with FLUKA simulations, neutrinos were used instead. For the implementation the SOURCE routine was used, to define a geometry that surrounds the volume to be mapped, e.g. a box. The neutrino starting point is sampled on the surface of that volume. The direction of the neutrino is sampled randomly. The input file contains two USRBIN cards, one for recording the fluence of neutrinos and one for recording the density weighted fluence. The latter is implemented using the FLUSCW routine. Within each volume bin, the density is determined by computing a weighted average of the detector densities encountered along the paths of the neutrino as

$$\rho = \frac{\sum_i \Phi_i \; \rho_i}{\sum_i \Phi_i}, \tag{5.1}$$

with neutrino fluence Φ_i. In Fig. 5.8, a density map depicting the FLUKA model of the ATLAS detector and the adjacent cavern in the R - $|z|$ plane, with averaging performed over the azimuthal angle ϕ and the sign of z is presented. This geometry corresponds to Phase 2.

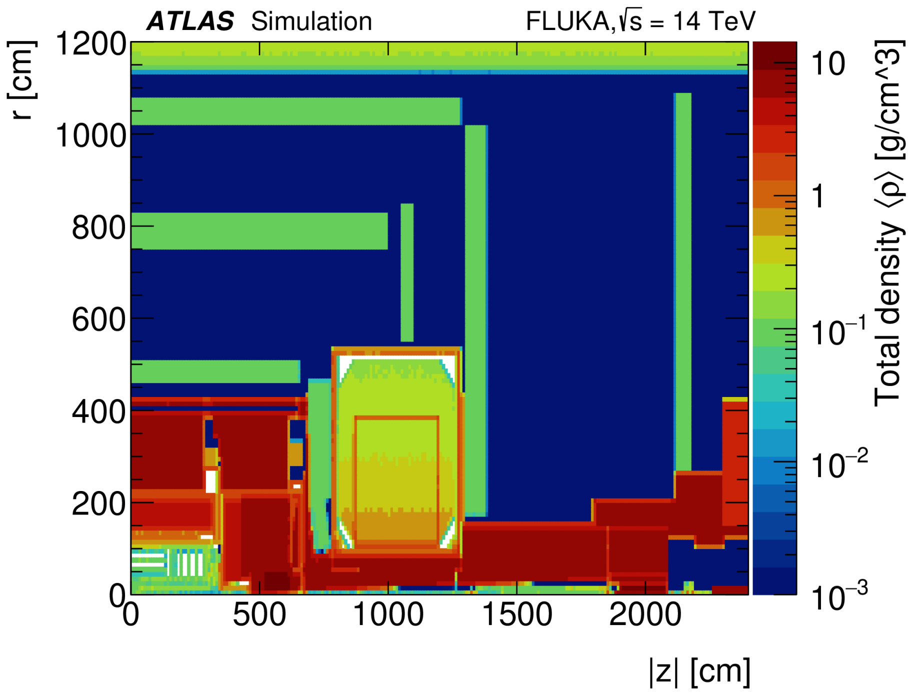

Figure 5.8.: The average material density derived from a FLUKA geometry of the ATLAS detector, corresponding to the Phase 2 configuration is shown. These values are obtained through a comprehensive scan using neutrinos. The colours in the visual representation are used to convey density information on a logarithmic scale. Regions predominantly composed of gaseous materials are appear in blue, while areas containing lighter solids and fluids range from green to orange, and volumes comprising metallic materials appear in red.

The density map in Fig. 5.8 offers a comprehensive view of the overall average density. However, for more detailed investigations, such as analysing material variations between geometries or simulation frameworks, additional information becomes necessary. Displaying the density of specific chemical elements can offer significant insights. For instance the hydrogen density map shown in Fig. 5.9 can be particularly useful in neutron moderator studies. Once the total density mapping is established, separating individual materials is straightforward within the FLUSCW routine.
In the visualization tool [81], maps for 92 elements have been generated for various detector regions. Similar to the energy spectra and time-dependent TID binning, the tool allows users to select a specific bin, displaying the material composition of these 92 elements with a periodic table, as depicted in Fig. 5.10.

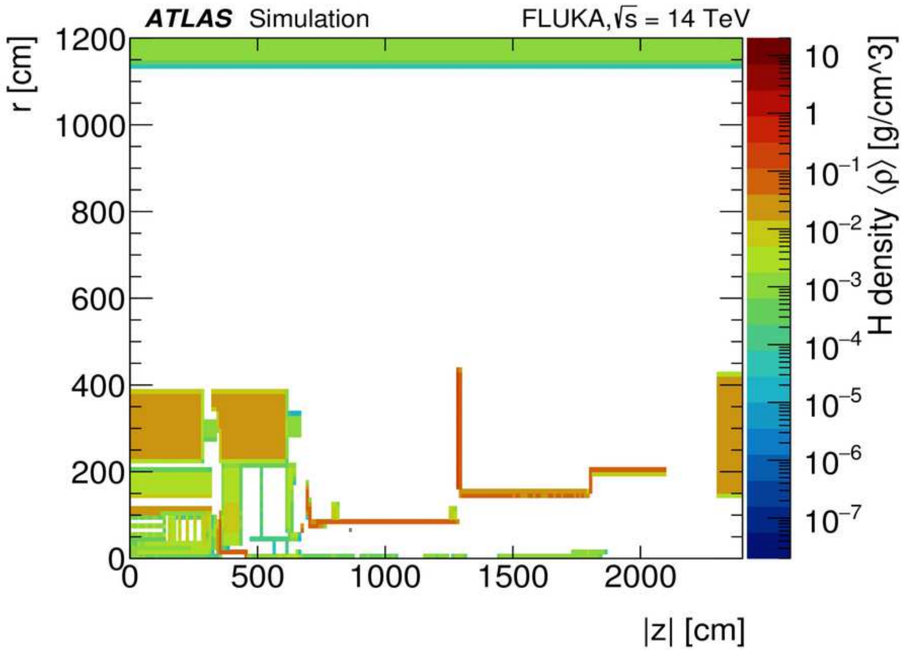

Figure 5.9.: Shown is the hydrogen density derived from a FLUKA simulation of the ATLAS detector, employing the Phase 2 configuration. White regions don't contain any hydrogen.

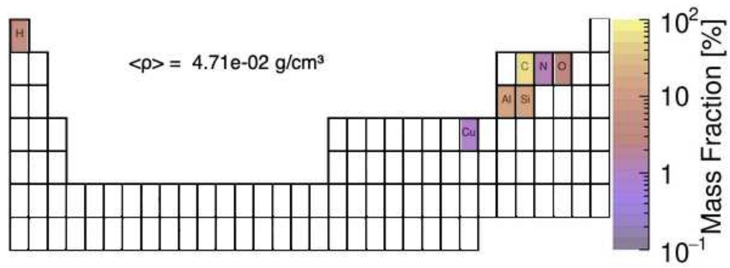

Figure 5.10.: Partial material densities for 92 elements together with the total density, displayed for a specified bin: 40 cm $\leq r <$ 50 cm and 170 cm $\leq z <$ 180 cm. The selection of the bin, is done with the cursor in the interactive visualisation tool [81].

Single element maps have proven invaluable for debugging geometries. Fig. 5.11a, comparing simulated $\Phi^{\mathrm{Si}}_{\mathrm{n_{eq}}}$ results from FLUKA and Geant4 illustrates this. Between z = 300 cm and z = 350 cm, the results begin to diverge, consistent with a similar trend observed in thermal neutron fluence. Upon examining the partial hydrogen and boron maps, the latter are displayed in Fig. 5.12a, the cause of the discrepancy became immediately apparent: a detector part with significant hydrogen and boron content was absent in the Geant4 geometry. The deficiency in boron content influenced thermal neutron fluence, while missing hydrogen affected $\Phi^{\mathrm{Si}}_{\mathrm{n_{eq}}}$. Fig. 5.12b shows the implemented correction and Fig.5.11b the corrected result.

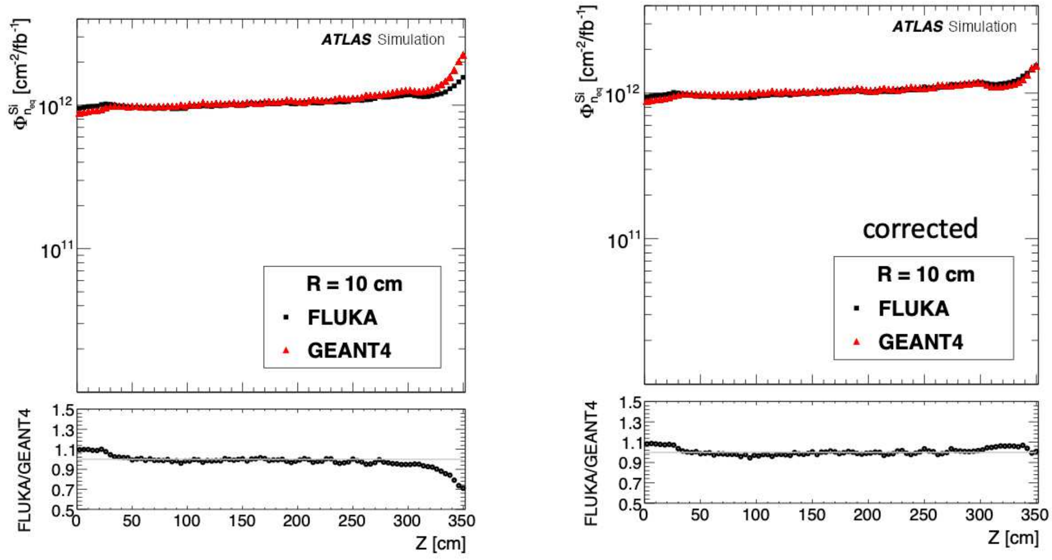

(a) (b)

Figure 5.11.: Simulation results of the Si 1 MeV neutron equivalent fluence in the inner detector of the ATLAS Phase 2 upgrade. (a) shows a version with an error in the Geant4 results. (b) shows the corrected version. The Geant4 data is taken from [81]

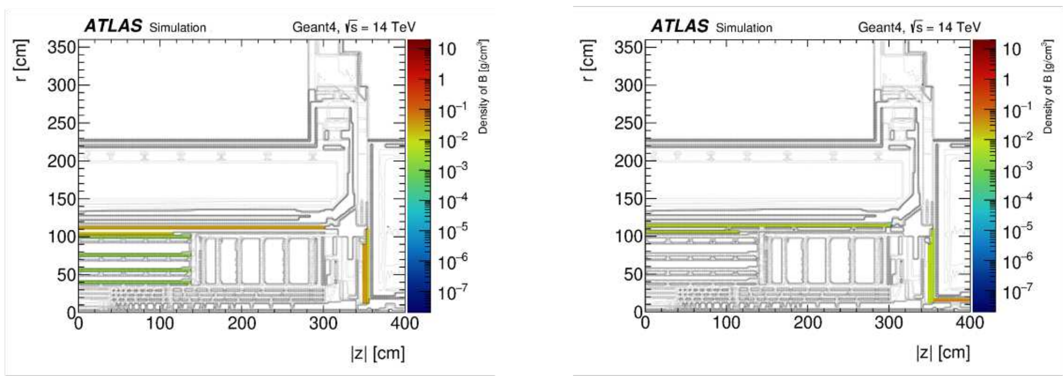

(a) (b)

Figure 5.12.: Boron material maps of the ATLAS Phase 2 upgrade of Geant4. In (a) a component rich in boron is missing between $z = 300$ cm and $z = 350$ cm and $R < 20$ cm. The graphs are taken from [81]

Ultimately, the spatial binning outcomes for material composition, energy spectrum, and TID time distribution, along with additional fluence and dose predictions obtained through FLUKA's standard scorings, are incorporated into the visualization tool [81]. These additional methods are discussed in the subsequent section.

5.2.4. Fluence and Dose Predictions with FLUKA's Standard Scoring

The visualization tool includes multidimensional maps, primarily represented in cylindrical coordinates $|Z|$ and R, where Z corresponds to the beam direction and R represents the perpendicular direction to Z. These maps are commonly used for estimating the radiation background and provide valuable insights into the relevant simulation outcomes such as:

- the total ionising dose (TID) ,
- the equivalent fluence of 1 MeV neutrons in Silicon ($\Phi^{\mathrm{Si}}_{\mathrm{n_{eq}}}$),
- the fluence of hadrons with $E > 20$ MeV,
- the fluence of neutrons with $E > 100$ keV,
- the fluence of charged hadrons.

Example radiation maps in two dimensions are illustrated in Fig. 5.13, displaying the TID and the $\Phi^{\mathrm{Si}}_{\mathrm{n_{eq}}}$. These radiation levels span 10 orders of magnitude across the entire detector region, with the highest levels observed near the beam pipe and the lowest levels in regions effectively shielded by the massive calorimeters and forward shielding components.

Of particular significance are gaps in the detector's hermeticity, such as the service areas that separate the barrel and endcap LAr calorimeters ($|z| \approx 330$ cm, 150 cm $< r < 200$ cm) and the barrel and extended barrel Tile calorimeters ($|z| \approx 300$ cm, 230 cm $< r < 400$ cm), which contain electronics and air instead of dense absorbers. These areas act as particle chimneys, transporting radiation to outer locations in r and are crucial for estimating radiation exposure to the front-end electronics of the calorimeters. The maps suggest that these areas experience higher radiation levels, although they are small and not easily discernible within the comprehensive coverage of the ATLAS maps.

Fig. 5.13 shows FLUKA simulation results at $\sqrt{s} = 14$ TeV, normalised to $\sigma_{\mathrm{inel}} = 79.31$ mb and $L = 4000$ fb^{-1}. Fig.5.13a shows the TID and 5.13b the associated statistical uncertainty. Fig. 5.13c depicts the $\Phi^{\mathrm{Si}}_{\mathrm{n_{eq}}}$ and 5.13d the associated statistical uncertainty.

The TID is dominated by electrons and low energy protons from (n,p) reactions in hydrogen containing materials. Thus, the material dependence of dE/dx is larger than that of neutrons.

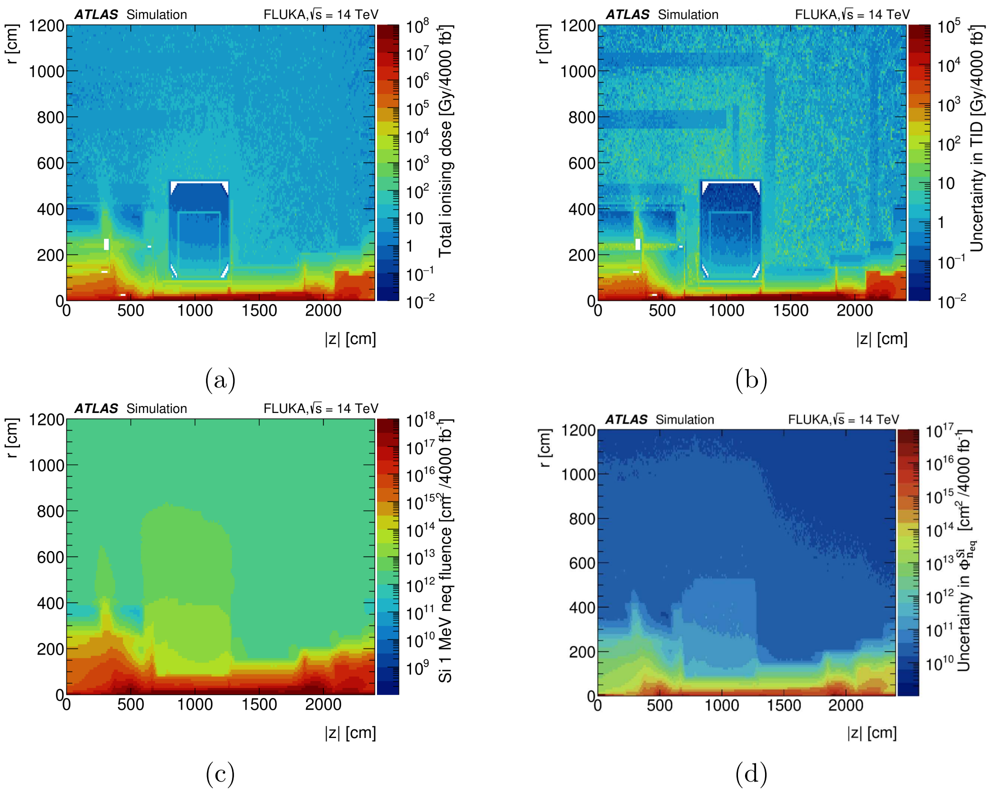

Figure 5.13.: (a) Shows the total ionising dose (TID) and (b) its associated statistical uncertainty; (c) the 1 MeV neutron equivalent fluence in Silicon and (d) its associated statistical uncertainty from a FLUKA simulation of the ATLAS detector setup of Phase 2 with $\sqrt{s} = 14$ TeV normalised to a cross section of $\sigma_{\text{inel}} = 79.31$ mb and an integrated luminosity of $L = 4000$ fb^{-1}. Bin-averages are shown on a color scale for $\Delta r \times \Delta|z| = 10 \times 10$ cm^2 in the full detector region, with $|z| < 24$ m and $R < 12$ m.

5.2.5. Conclusions and Applications

The interactive webpages for exploring the material composition, partial densities, radiation quantities, particle- and time-dependent TID spectra within two-dimensional maps of the ATLAS detector have been extended to show FLUKA results in addition to those from Geant4. Initially set up for Geant4 results, they are now available for FLUKA as well. These interactive visualization pages are implemented using plain HTML and JavaScript, ensuring a seamless and responsive experience on modern computers and web browsers.

Analysing both particle spectra and TID time distributions at any location within the detector, along with related radiation quantities using the visualisation tool, enables a rapid assessment of radiation damage predictions for future upgrades. The utilisation of both FLUKA and Geant4 has become indispensable for simulation work within the

ATLAS experiment. The availability of both frameworks within the same visualization tool significantly simplifies the comparison between FLUKA and Geant4 results.
For instance, the partial density maps have proven highly beneficial in debugging the geometrical description of the ATLAS detector and revealing differences between the setups of the two frameworks.

6. Shielding Studies for the ATLAS Experiment

This chapter delves into the detailed examination of specific detector components within the current Run 3 geometry and the Phase 2 Upgrade of the ATLAS experiment using FLUKA simulations. In particular, the focus is on three specific cases: neutron moderators, sensors close to cooling stations, and the luminosity detector concept LUCID-3. Through these simulations, it is aimed to gain insights into their responses to the radiation environment within the intricate experimental setup.

6.1. Introduction of a Toy Model for Effective Moderator Studies

To study in detail the neutron attenuation process, a toy model is devised. This model, characterised by its simplicity and computational efficiency, enables the examination of different material compositions. Notably, it grants a more straightforward analysis of individual scattering events compared to comprehensive FLUKA simulations. The subsequent section presents illustrative examples that showcase the model's potential and serves to investigate the parameter space for a design upgrade of the neutron moderators in the ATLAS Phase 2 geometry. This paves the way for a more detailed and complex investigation in Section 6.2, fostering a general understanding of the effectiveness of hydrogen and boron in neutron shieldings.

The simplified model takes the following interactions into account:

- n - H elastic scattering
- n - C elastic scattering
- n - B absorption
- n - H absorption

Each interaction occurs with a certain probability given by its cross section σ, taken from [59]. Based on the cross section, the mean free path can be calculated according to Eq. (2.14). To simulate the transport, the distance to each type of collision is sampled from an exponential distribution and the interaction type with the shortest path is then taken. If it is a scatter event, a new energy is calculated depending on the scattering angle, which is assumed isotropic in the centre-of-mass frame with a complete loss of kinetic energy for backward scattering and no loss for forward scattering (assuming the mass of the proton equals that of the neutron). When the neutron is absorbed or exits the system a new particle is started.

If the particle with mass m_{part} is moving with $v_{\text{part}}^{\text{LAB}}$ in the laboratory frame and the target of mass m_{targ} has a velocity in the laboratory frame of $v_{\text{targ}}^{\text{LAB}}$, then the velocity of the center of mass (v_{cm}) is given by

$$v_{\text{cm}} = \frac{v_{\text{part}}^{\text{LAB}} \cdot m_{\text{part}} + v_{\text{targ}}^{\text{LAB}} \cdot m_{\text{targ}}}{m_{\text{part}} + m_{\text{targ}}}. \tag{6.1}$$

In order to get the target velocity $v_{\text{targ}}^{\text{LAB}}$, the energy of the target particles is sampled from the Maxwell-Boltzmann distribution

$$f(E) = 2^{3/2} \cdot (k_B T)^{-3/2} \cdot \sqrt{\frac{m}{\pi}} \cdot \sqrt{E} \cdot e^{-\frac{E}{k_B T}}. \tag{6.2}$$

The velocity of the particle in the center of mass frame $v_{\text{part}}^{\text{CM}}$ can be calculated

$$v_{\text{part}}^{CM} = v_{\text{part}}^{\text{LAB}} - v_{\text{cm}}. \tag{6.3}$$

The elastic scattering angle is sampled isotropically in the CM frame and the velocity after the collision is boosted into the laboratory frame.

The target-energy sampling from the Maxwell-Boltzmann distribution is only essential for the thermal region, in order to prevent further energy loss, once the neutron is thermal. A thermal neutron absorbs on average as much energy as is looses in a collision. For higher neutron energies $v_{\text{targ}}^{\text{LAB}} \approx 0$ is a good approximation.

Parameters, Insights, and Conclusions from the Toy Model

A target/moderator consisting of 1 to 5 cm thickness of Pure Polyethylene (PE) or Boron-Doped Polyethylene (BPE) is exposed to 1 MeV neutrons, infinite in the lateral directions. For the BPE, with a density of 0.99 g/cm^3, natural boron mass fractions between 0 to 5% are considered. The remaining mass comprises hydrogen and carbon in a 1/6 ratio.
Fig. 6.1 presents the energy spectra of neutrons that have penetrated the 5 cm PE moderator, along with a comparison to the corresponding FLUKA and Geant4 outcomes. The hydrogen state, whether bound or free, significantly influences the results. The toy model and Geant4 assume free H, while FLUKA defaults to H_2O bound. This distinction,

altering the effective mass of the molecule, primarily affects the thermal peak. In the case of CH_2 bound hydrogen, a slightly lower thermal peak is observed and its low-energy edge is shifted due to the larger effective target mass shown in Fig. 6.1b. In Fig. 6.1a each framework assumes free hydrogen.

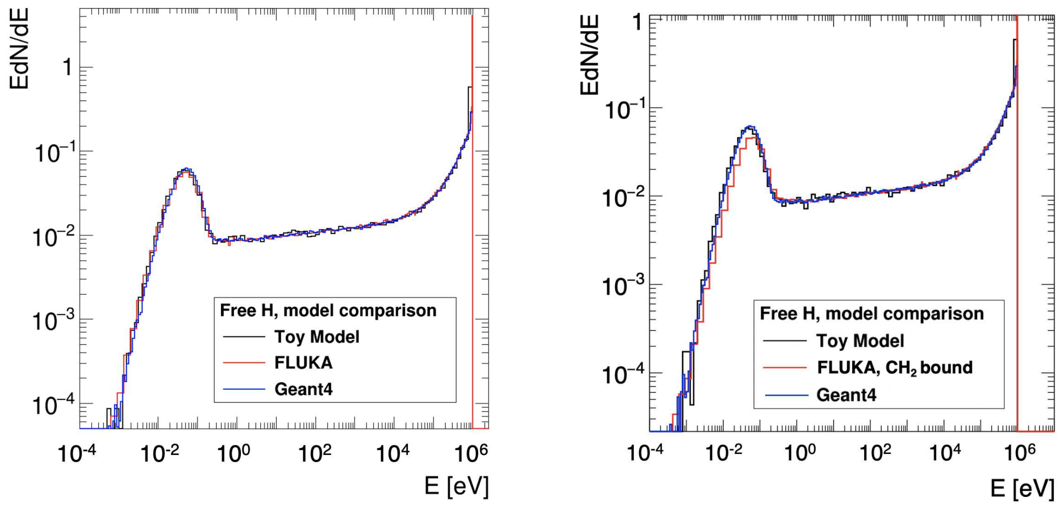

(a) (b)

Figure 6.1.: Spectrum of 1 MeV neutrons that passed a 5 cm moderator of pure polyethylene, simulated by the toy model, Fluka and G4. On the left graph all frameworks assume free hydrogen and on the right one, FLUKA assumes CH2 bound hydrogen.

Fig. 6.2 visualizes the percentage of neutrons that traverse the moderator for different boron configurations. Fig. 6.2a represents the whole spectrum and 6.2b only the thermal (weighted with the ^{10}B cross section). The latter demonstrates that a 1 % boron content reduces the passage of thermal neutrons by 77 %; going to 2 % boron gives an additional 8 % reduction and at 5 % boron an additional reduction of about 7 %. Comparing 5 % to 1 % boron gives a difference of 75 %.

Figure 6.2c illustrates the $>$ 100 keV neutrons. Due to the large step seen in the neutron damage function of Fig. 4.2, the latter is a good approximation of the neutron contribution to $\Phi^{\mathrm{Si}}_{\mathrm{n_{eq}}}$. It can be seen, that the number of passed high energy neutrons slightly increases with the boron content. Increasing boron from 0 to 5 %, increases the number of passed $>$ 100 keV neutrons by about 8 %. This is due to the corresponding reduction of hydrogen in the moderator and therefore, the reduction of effective moderator thickness. According to the parameters above, the partial hydrogen density with no boron in the moderator is 0.14 g/cm^3, while its value for 5 % boron in the moderator drops to 0.13 g/cm^3. For a moderator thickness of 5 cm, this difference corresponds to a reduction of effective moderator thickness by roughly 0.25 cm.

Fig. 6.2d depicts the percentage of $>$ 100 keV neutrons that traverse the moderator as a function of its thickness. Comparing the two boron configurations reveals that reducing hydrogen content by increasing boron results in an increase in > 100 keV neutrons passing through. However, the plot illustrates how minor this effect is compared to variations in moderator thickness.

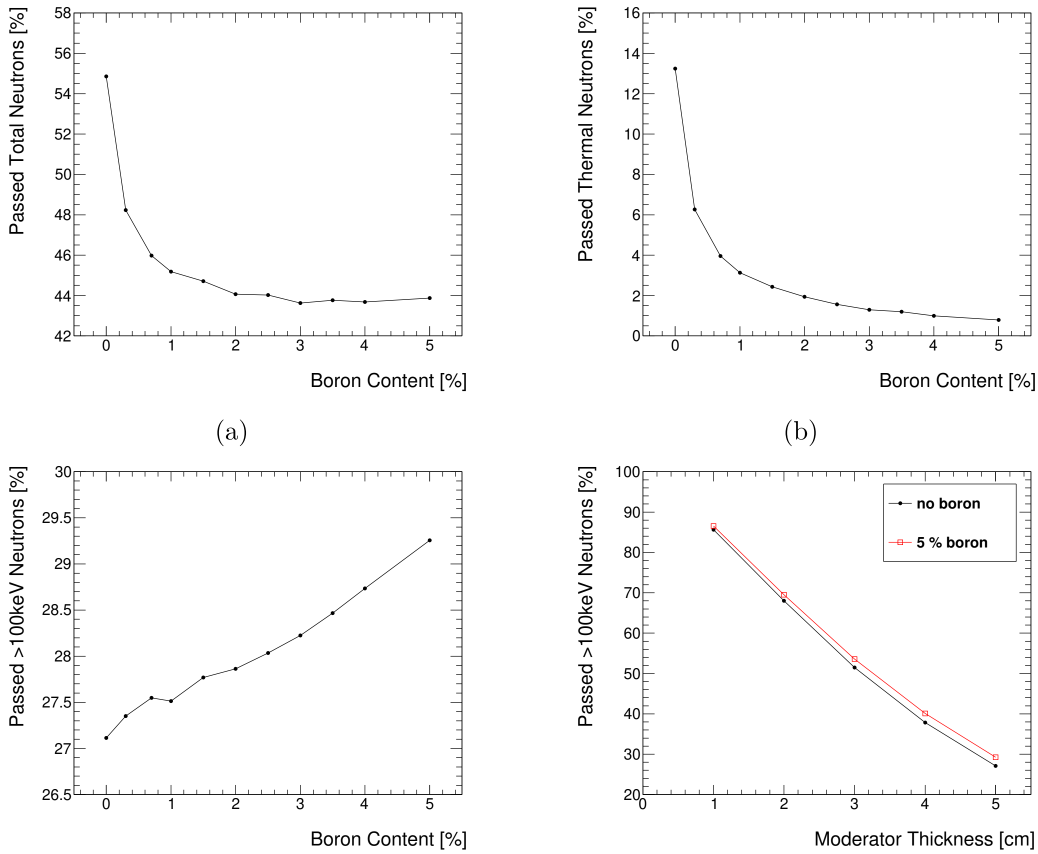

(a) (b) (c) (d)

Figure 6.2.: Toy model results of moderator studies with varied boron content and 1 MeV neutrons. Since the results are from a single run, there are no error bars. In 6.2a all neutrons / in 6.2b thermal neutrons / in 6.2c > 100 keV neutrons - that passed relative to the initial amount. In 6.2d neutrons above 100 keV are plotted as a function of the moderator thickness.

The results of the 5 cm thickness confirm the reduction of effective moderator thickness by roughly 0.25 cm. Furthermore, it demonstrates how this effect diminishes with decreasing moderator thickness, as the reduction in hydrogen content becomes more crucial for shielding neutrons with kinetic energies 100 keV. A thickness increase from 1 to 2 cm results in an effect of approximately 19 %, whereas the effect of increasing from 4 to 5 cm is only about 10 %. Hence, it can be concluded that slight decreases in moderator thickness or hydrogen density may be justified. However, unlike the trend observed for boron content, up to 5 cm there is significant gain if monoenergetic 1 MeV neutrons are assumed.; in other words, the mrgin is narrower. This also implies that a potential increase in moderator thickness or hydrogen density could be highly effective in slowing down neutrons.

Fig. 6.3 visualises a result that can easily be assessed by the toy model, but is difficult to extract from FLUKA: the percentage of thermal neutron absorptions on boron versus hydrogen as a function of boron content. This points out the effectiveness of boron capture, since already 0.3 % of boron dominate over the absorption events of hydrogen. The thickness of the moderator is 5 cm.

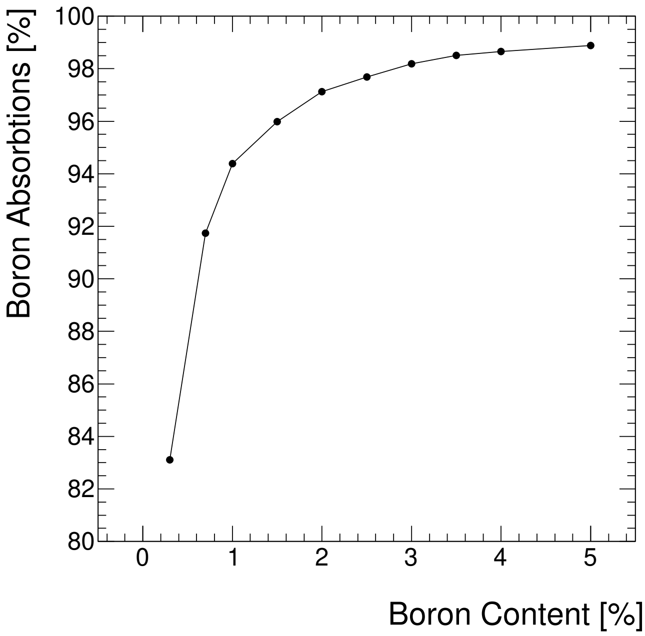

Figure 6.3.: The percentage of neutrons absorbed by boron in a 5 cm thick moderator.

In crafting an effective moderator design based on the approximate toy model, it can be concluded that boron is highly effective in absorbing and thus shielding thermal neutrons. However, its effectiveness levels off when exceeding about 1-2 % of the moderator mass fraction. Conversely, the shielding effect of hydrogen against high-energy neutrons shows much less plateauing, thus maximizing its content is highly favourable. Yet, the effect of decreasing small amounts of boron in order to gain hydrogen is still very small (about 2 %), considering a moderator effective thickness about 5 cm.

6.2. Neutron Moderators and the Effect of Boron

The toy model in Section 6.1 was used to study a simple moderator layer and monoenergetic neutrons. The ATLAS geometry however, is more complex and the calorimeter albedo has a wide spectrum. For more detailed investigations FLUKA simulation are applied to study the radiation environment in the ITk in detail. The results are utilised to adapt the material compositions, to gain shielding efficiency and address issues of material constraints. The following, partly independent, studies are performed:

1. The albedo from the plain ECAL is investigated in order to set a scale for the moderator efficiency.
2. In order to determine the impact of reducing the amount of boron on the thermal neutron fluence several simulations with different boron content are done. The way the boron content is decreased below 5 % is by partially replacing B-10 by B-11. In that way the hydrogen density is kept constant while the effective density of the B-10 is reduced.
3. To investigate potential cross talk, i.e. whether neutrons originating from the endcap at $+z$ contribute to regions close to $-z$ and vice versa, the direction cosines of neutron fluence in the ITk are studied.
4. In order to determine the impact of reducing the hydrogen density several simulations with different densities are performed. Furthermore, the contribution of neutrons to the total $\Phi^{\mathrm{Si}}_{\mathrm{n_{eq}}}$, in comparison to other particles, is illustrated.
5. Connecting the above two points, the effect of hydrogen loss due to the boron doping is investigated.
6. In a separate section the FLUKA results are compared to GEANT4. Beyond the comparison of the two MC codes, two essentially different FLUKA versions are set side by side. The older one with group-wise low energy neutron transport and the recently released one with point-wise transport. With respect to the GEANT4 comparison this is of special interest, because GEANT4 using a point-wise approach has been one of the major differences between these codes.

Before delving into the various neutron moderator studies, the current moderator configuration is introduced.

6.2.1. Neutron Moderator Configuration

The ITk is enveloped by four moderators: the outer and inner barrel poly-moderator, and two located between the HGTD and the endcap calorimeter cryostat, known as the outer and inner end-cap moderator. After completing the studies, it was found that the dimensions of moderator thickness and length were inconsistent with the ones used for the Geant4 geometry. However, as these minor discrepancies do not undermine the primary conclusions, the dimensions were revised solely for comparisons with Geant4 (Section 6.2.7). The updated dimensions, representative of the baseline Phase 2 geometry, are outlined in Tab. 6.1. The dimensions provided in parenthesis are utilised solely for the simulations presented in this chapter.

	Length (cm)	Thickness (cm)
Inner Barrel	230	2.5 (3)
Outer Barrel	634.9 (619.6)	2.5 (2.9)
Inner End-cap	78	2.5 (3)
Outer End-cap	99	2

Table 6.1.: Dimensions of the baseline Phase 2 ITk moderator components, used for the comparison to Geant4. In parentheses, the outdated values (used only for the FLUKA studies).

The simulation results are recorded at radii of $R = 10\,\text{cm}$, which corresponds to the characteristic radius of the pixel detector, at $R = 40\,\text{cm}$, which corresponds to the innermost radius of the strip detector, and at $R = 100\,\text{cm}$. The latter one corresponds to the outermost layer and is positioned closest to the moderators. For this reason the largest influences from changes in the moderator composition are expected to be observable there. For the z-averaging, the range of $Z = 0 - 24\,\text{cm}$ was chosen, as it corresponds to the range of the barrel pixel detector, and $Z = 120 - 136\,\text{cm}$, since it represents the end of the barrel strip detector. The scoring regions, together with the design of the moderators are illustrated in Fig. 6.4. The radial averaging is done within the intervals listed in Tab. 6.2.

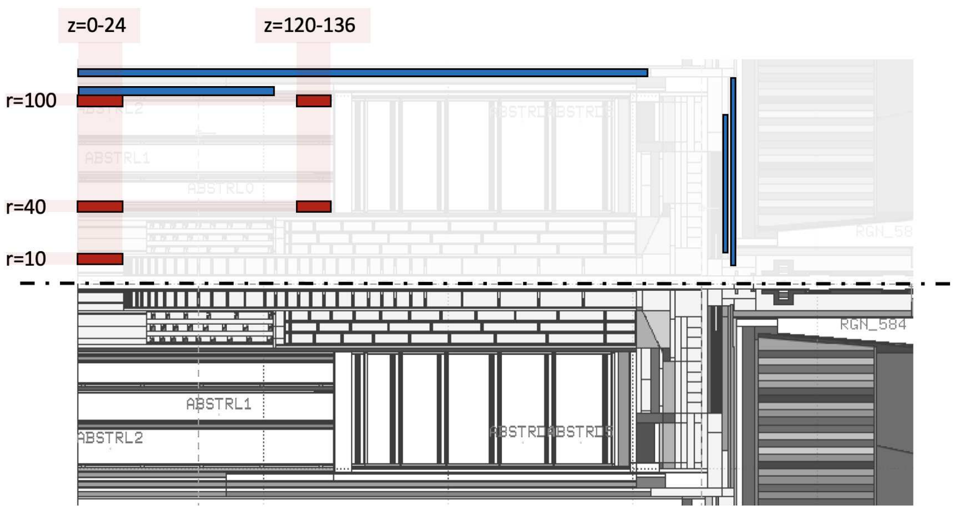

Figure 6.4.: FLUKA geometry of the yz - plane of the neutron moderators surrounding the Inner Tracker (ITk) of the Phase 2 upgrade. The blue regions indicate the barrel and end-cap poly-moderators. The red regions illustrate the areas at which the simulation results are recorded in chapter 6.2.All values are given in cm.

r (cm)	Interval (cm)
10	8 – 12
40	36 – 44
100	92 – 100

Table 6.2.: Intervals used for the radial averaging. r gives the nominal and the interval the radial bin width.

The baseline composition of the moderator in the Phase 2 geometry is listed in Tab. 6.3. It contains 5 % natural boron, that is composed of 80 % ^{11}B and 20 % ^{10}B where only the latter acts as neutron absorber.

Material	Mass Fraction (%)
Carbon	81.3
Hydrogen	13.7
Boron-11	4
Boron-10	1

Table 6.3.: Material composition of the moderator in the Phase 2 geometry. The total density of the moderator material $\rho = 0.99\,\mathrm{g/cm^3}$.

6.2.2. Contribution of the plain Electromagnetic Calorimeter Albedo

The ECAL incorporates a significant amount of lead, which results in a higher neutron yield during hadronic interactions compared to lighter nuclei. This characteristic makes it the dominant neutron source in the vicinity of the ITk. This section delves into the neutron spectra originating from these interactions. To record the unmodified calorimeter albedo contribution, air is used to replace the moderating material. To quantify the influx of neutrons entering the ITk volume from both the barrel and endcap calorimeters, one-way boundary crossing scorings are implemented at $R = 145$ cm and $Z = 353$ cm, respectively. By not considering directional weightings in scoring, particles travelling from the ITk towards the ECAL and vice versa are taken into account separately. The scoring of the former, however, includes contributions from other calorimeter regions. Despite this, it remains insightful as it demonstrates the moderating potential of the ITk materials. Specifically, it is observed that the thermal neutron count is higher upon entry into the calorimeters, as depicted in Fig. 6.5. Within the resonance region (< a few MeV), the particle count is greater for neutrons exiting the calorimeters as can be observed in Tab. 6.4, owing to their production in lead within that energy range. The peak within this range surpasses 100 keV (as indicated by the line in Fig. 6.5). The NIEL cross section for neutrons has a jump by about an order of magnitude at energies about 100 keV as illustrated in Fig. 4.2. From this it can be concluded, that neutrons below that threshold are negligible for silicon damage, while those above are responsible for most of the damage. Thus, moderators serve as effective shielding for the silicon components in the ITk. The values in Tab. 6.4 also show that the endcap calorimeters emit about 17 times more neutrons into the ITk region than the barrel calorimeters, so their shielding is much more crucial. Some high energy neutrons (> 20 MeV) stem from primary pp-interactions while most come from particle showers. Consequently, there is a pronounced peak of high-energy neutrons entering the moderators, but only a minimal number exiting the moderators.

Event	Counts of > 100 keV Neutrons per $cm^2 \cdot fb^{-1}$
Entering Barrel Calorimeter	$2.25 \pm 0.07 \times 10^{10}$
Exiting Barrel Calorimeter	$2.40 \pm 0.07 \times 10^{10}$
Entering End-cap Calorimeter	$1.65 \pm 0.06 \times 10^{11}$
Exiting End-cap Calorimeter	$4.02 \pm 0.11 \times 10^{11}$

Table 6.4.: Neutrons with $E > 100$ keV entering/exiting the calorimeters per unit surface.

6.2.3. Impact of the Boron Content on the Thermal Neutron Fluence

Fig. 6.6 presents a comparison of the thermal neutron fluence at various radii within the ITk, considering boron contents of 5%, 1%, and 0% in the barrel moderators.

Comparing Fig.6.6a to Fig.6.6b below $Z = 300$ cm, the thermal neutron fluence results from the simulation without any boron are slightly higher for Fig.6.6b, i.e. for $R = 100$ cm. Between $Z \approx 300$ cm to $Z = 350$ the fluence is higher at $R = 100$ cm. Results from simulations with with 1 % and 5 % boron in the moderator compound, show that the thermal neutron fluence is slightly lower in Fig.6.6b, i.e. the effect of the boron content on the moderator performance is slightly higher at $R = 100$ cm. This agrees with the expectation described in Section sec:ModConfig, based on the position of the moderator.

Additionally, it is evident in Fig. 6.6, that the influence of boron is most notable for small values of Z. This can be attributed to the fact that the boron content is not modified in the endcap calorimeters, which contribute significantly to the neutron fluence at larger values of Z.

Fig. 6.7 depicts the thermal neutron fluence as a function of boron content for regions averaged over R and Z by considering the mean value. It is evident that the thermal neutron fluence remains relatively stable between boron contents of 5% and 2.5%, while a notable increase is observed when transitioning from 1% to 0%. The color map displayed in Fig. 6.8a reveals that contributions from the endcap at $Z \approx 140$ cm and $R = 40$ cm are more prominent compared to $R = 100$ cm, in accordance with the trends presented in Fig. 6.7. A comparison between Fig. 6.8a and 6.8b demonstrates that the moderator with 5% boron efficiently mitigates thermal neutron fluence from the barrel. Reducing the boron content in the barrel moderator to 0% leads to comparable contributions from both the endcap (with a constant 5% B) and the barrel in the central regions of the ITk.

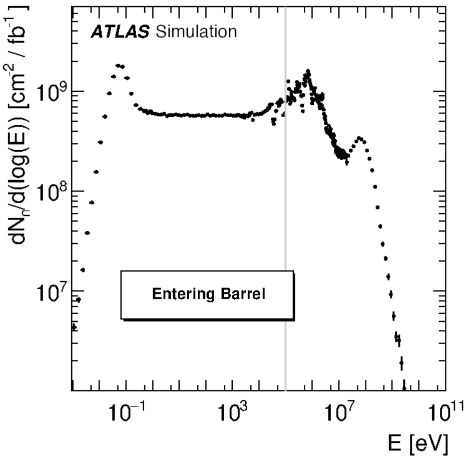

(a)

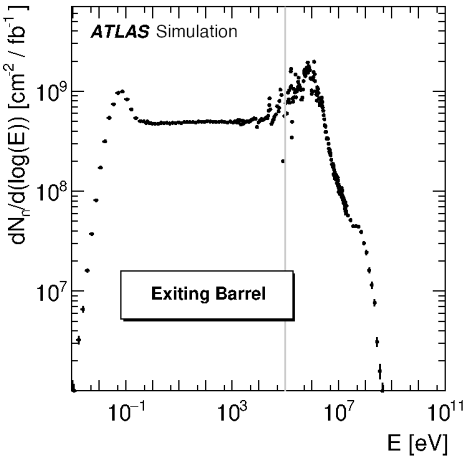

(b)

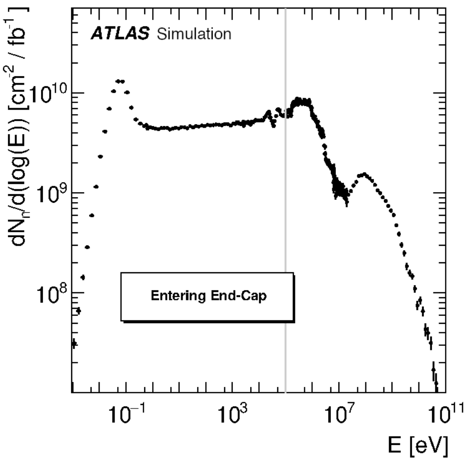

(c)

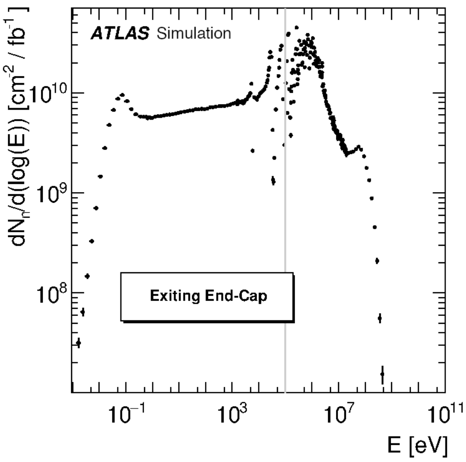

(d)

Figure 6.5.: Energy spectrum of neutrons exiting/entering the plain calorimeters. At energies above the 100 keV, threshold indicated with a gray line, neutrons are effectively contributing to silicon damage.

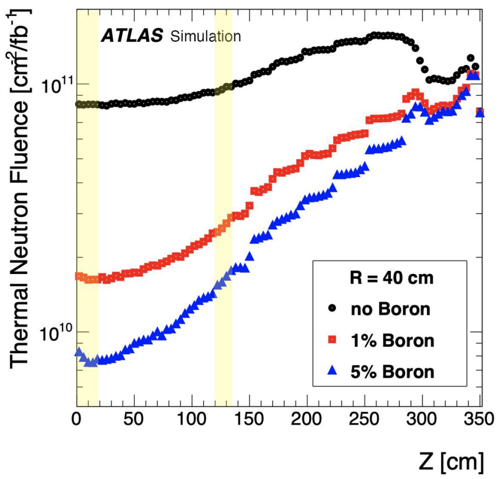

(a)

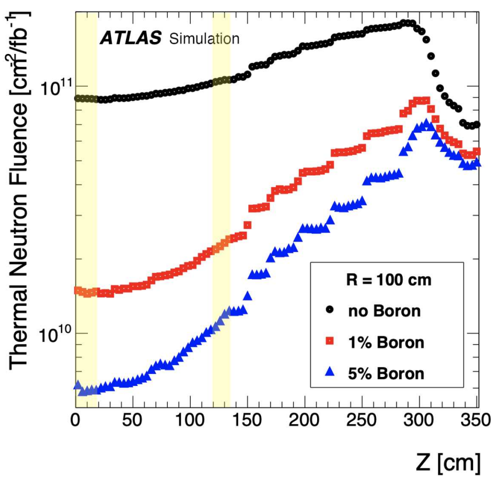

(b)

Figure 6.6.: Thermal neutron fluence as a function of z for three different boron configurations. It is averaged over the r-values at $R = 40\,\mathrm{cm}$ in Fig. 6.6a and $R = 100\,\mathrm{cm}$ in Fig. 6.6a by considering the mean values. The yellow-marked regions, indicate the z-ranges where the fluences are averaged for Fig. 6.7.

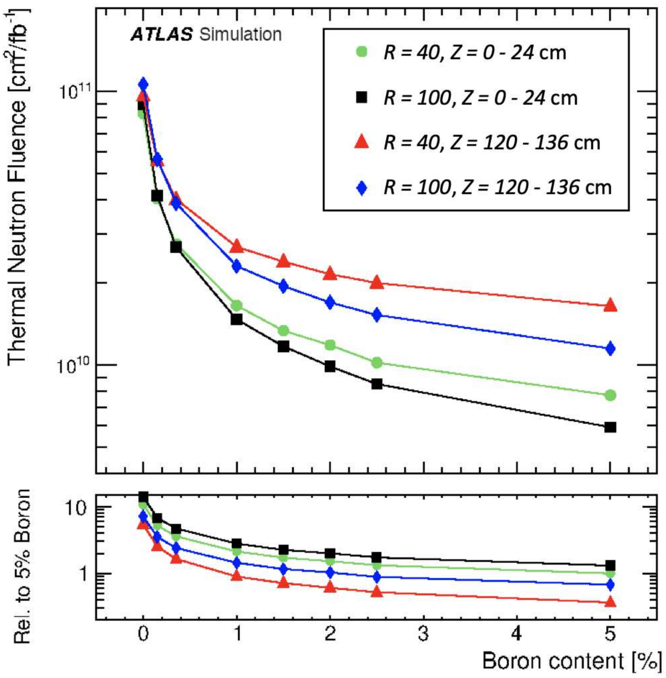

Figure 6.7.: Thermal neutron fluence as a function of the boron content, averaged over the indicated $R - Z$ regions by considering the mean value. The bottom graph illustrates the thermal neutron fluence values relative to the 5 % boron content. Statistical uncertainties are smaller than the marker sizes.

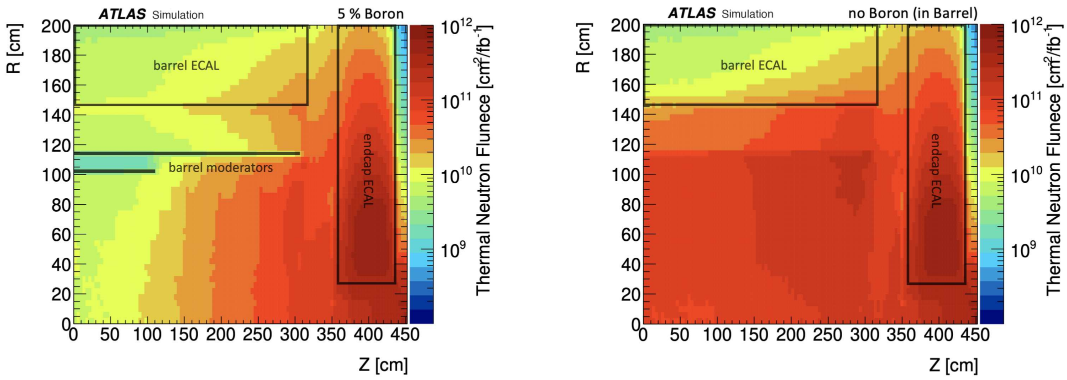

(a)

(b)

Figure 6.8.: Thermal neutron fluence in the ITk and calorimeter regions with the moderator compound containing 5 % boron as the baseline Phase 2 geometry does (a); without any boron in the barrel moderator (b). The endcap moderator has 5% boron in both cases.

6.2.4. Directionality of Thermal and Fast Neutrons

As depicted in Fig. 6.8, a significant fraction of neutrons is observed to propagate from the endcaps towards the $Z = 0$ plane. This observation raises the question of how pronounced the neutron fluence directionality is along the z-direction. To conduct a thorough investigation, simulation results of the direction cosines of neutrons within the ITk are examined. Fig. 6.9a and Fig. 6.9d illustrate that the distribution of direction cosines for neutrons in the negative Z region is skewed towards 1, while the distribution in the positive Z region (Fig. 6.9c and Fig. 6.9f) exhibits the opposite trend. Fig. 6.9b and Fig. 6.9e are symmetric, demonstrating that near $Z = 0$, the direction cosines along the z-axis (tz) predominantly peak at 1 and -1. Most of the neutrons come from the endcaps and have $tz < 0$ for $Z > 0$ and vice versa. This tendency is more pronounced for fast neutrons (> 100 keV) than for thermal neutrons.

The direction cosines tx, ty, tz are normalised, so that

$$tx^2 + ty^2 + tz^2 = 1. \tag{6.4}$$

Consequently, if one direction is biased, it biases the others in the opposite direction. In particular, since tz is biased towards -1 and 1, tx and ty are biased towards 0, as can be seen when the non-isotropy is significant enough, as it is the case for fast neutrons in Fig. 6.9d, 6.9e and 6.9f. Completely flat lines for all components, on the other hand, indicate a perfectly isotropic flux.

Fig. 6.9b and 6.9e visually reveal the presence of larger statistical uncertainties, a result stemming from the lower fluence within the interval $Z = [-50\,\text{cm}, 50\,\text{cm}]$ as compared to the intervals $Z = [-300\,\text{cm}, -250\,\text{cm}]$ and $Z = [250\,\text{cm}, 300\,\text{cm}]$. By juxtaposing Fig. 6.9a and 6.9b, it becomes apparent that thermal neutrons predominantly reside within their respective hemispheres, given the average neutron count of ≈ 8000 per bin at both ends and a count of ≈ 600 around $Z = 0$. This observation suggests that only a minimal number of thermal neutrons traverse the entire ITk. Furthermore, from Fig. 6.9d and 6.9e, it emerges that approximately 3500 fast neutrons with $tz \approx 1$ (directed toward the $+z$ side) are situated on the $-z$ side, with this number decreasing to about 1000 at $Z \approx 0$. Analogously, approximately 1000 fast neutrons are found on the $+z$ side. Hence, at least $70 - 80\%$ of even the fast neutrons do not traverse the entire length. Thermal neutrons are distributed almost isotropically in all z-directions, with approximately equal amounts on both sides.

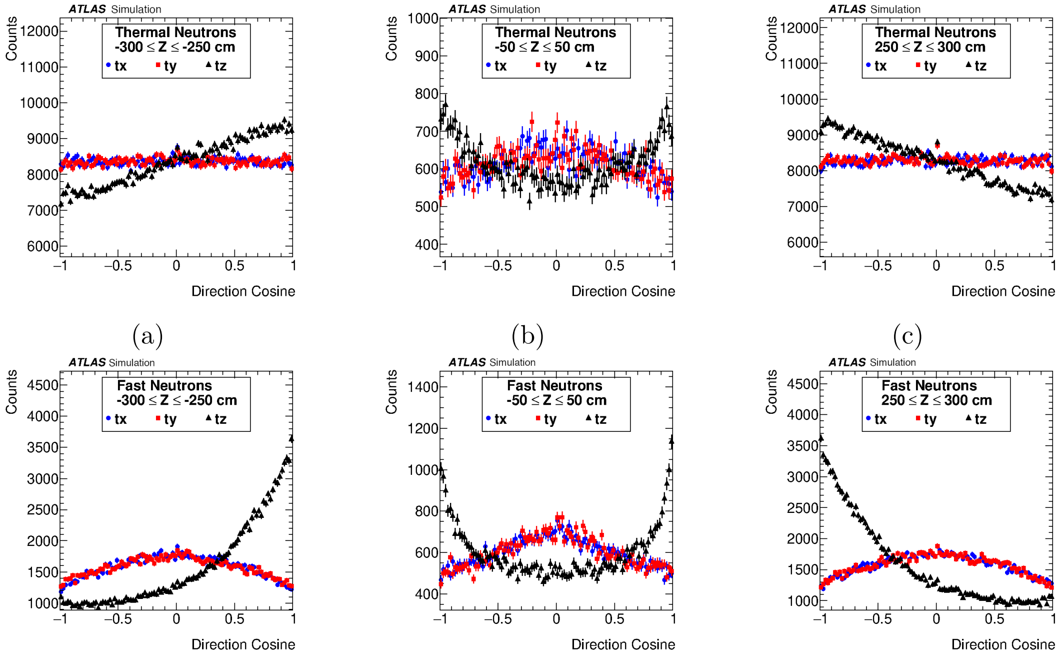

(a) (b) (c)

(d) (e) (f)

Figure 6.9.: Neutron counts as a function of direction cosines within the ITk. Thermal neutrons are illustrated in the top, fast neutrons in the bottom graphs. From left to right the graphs distinguish in the covered z region.

6.2.5. Impact of the Effective Moderator Thickness on the $\Phi^{\mathrm{Si}}_{\mathrm{n_{eq}}}$

In Fig. 6.10, the $\Phi^{\mathrm{Si}}_{\mathrm{n_{eq}}}$ values are presented for three different moderator densities. The illustration includes the baseline Phase 2 geometry with barrel moderator densities of $0.99\,\mathrm{g/cm^3}$, as well as densities of $0.4\,\mathrm{g/cm^3}$ [1] and cases without any moderator. The effect is most prominent at small $|z|$, attributed to the fact that the end-cap moderator density remains constant at $0.99\,\mathrm{g/cm^3}$, whereas only the barrel moderator density is altered. This leads to a larger impact in regions closer to the barrel moderator, particularly evident at $R = 100\mathrm{cm}$.

In Fig. 6.11, the $\Phi^{\mathrm{Si}}_{\mathrm{n_{eq}}}$ values for R and Z averaged regions are presented as a function of the barrel moderator density. Simulations with densities $\rho > 1\,\mathrm{g/cm^3}$ were conducted to explore the asymptotic behavior when increasing the hydrogen content beyond the baseline design. The impact is minimal at $R = 10\,\mathrm{cm}$, whereas it becomes significant at $R = 100\,\mathrm{cm}$. This trend is highlighted in Fig. 6.11b, where the fluence is plotted relative to the density of the baseline moderator with $\rho = 0.99\,\mathrm{g/cm^3}$. At $R = 100\,\mathrm{cm}$, the increase in fluence from $0.2\,\mathrm{g/cm^3}$ (equivalent to an effective thickness of 1 cm) is

[1] A density of $0.4\,\mathrm{g/cm^3}$ would obviously be exaggeratedly low. This low value is taken only to simulate a reduced thickness of the normal density material.

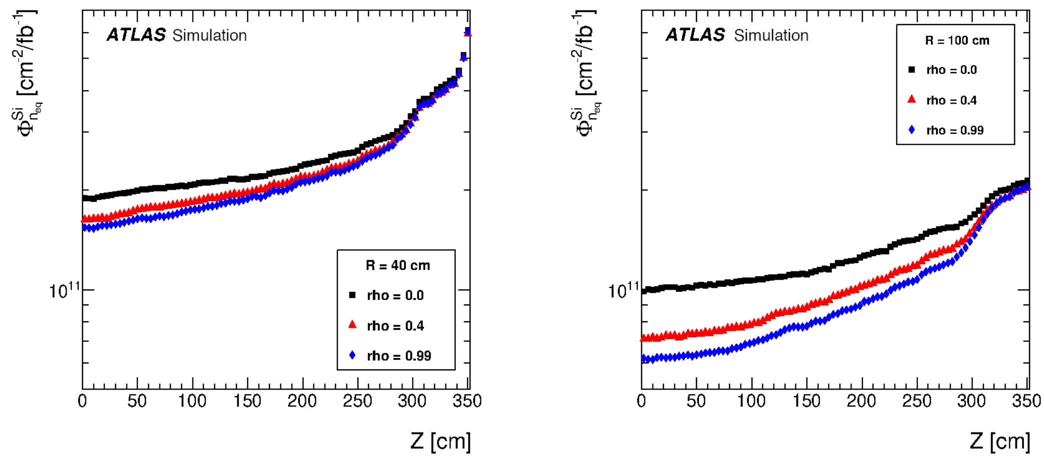

(a) (b)

Figure 6.10.: $\Phi^{\mathrm{Si}}_{\mathrm{n_{eq}}}$ as a function of z, for three different moderator density configurations. It is averaged over the r-values around $R = 40\,\mathrm{cm}$ (left) and $R = 100\,\mathrm{cm}$ (right) by considering the mean value.

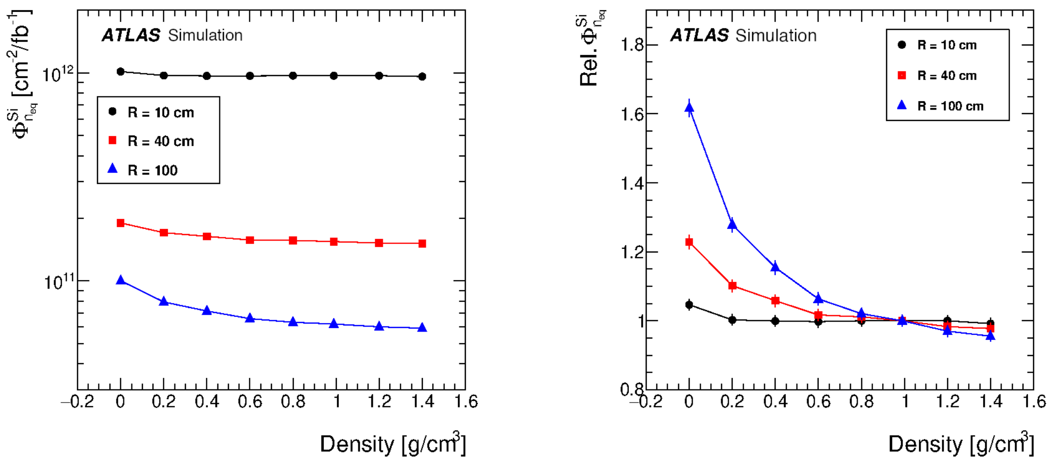

(a) (b)

Figure 6.11.: $\Phi^{\mathrm{Si}}_{\mathrm{n_{eq}}}$ of R and Z averaged regions as a function of the moderator density with z-averaging from 0 to 24 cm (left) by considering the mean value. $\Phi^{\mathrm{Si}}_{\mathrm{n_{eq}}}$ relative to the density of the baseline moderator $\rho = 0.99\,\mathrm{g/cm^3}$ (right).

approximately 27 %. For $0.4\,\mathrm{g/cm^3}$ (2 cm effective moderator thickness), the increase in fluence is about 15 %, while densities exceeding $1\,\mathrm{g/cm^3}$ (5 cm effective moderator thickness) yield gains of less than 5 % per cm. Therefore, increasing the thickness beyond approximately 5 cm results in only marginal improvements, even in the most sensitive regions. The results in Fig. 6.11b differ from the results of the toy model in Fig. 6.2d, because of the effect of the radiation background from the endcap calorimeters, which is absent in the toy model but significant in the full ATLAS simulation.

The $\Phi^{\mathrm{Si}}_{\mathrm{n_{eq}}}$ values in Fig. 6.10 encompass the silicon damage resulting from the collective impact of all particles. In Fig. 6.12a, detailed exploration of the damage contributors is undertaken by separately analyzing the damage caused by neutrons and all other particles. This investigation employs barrel and end-cap moderators with a density of $\rho = 0.99\,\mathrm{g/cm^3}$. At the two larger radii under consideration, neutrons dominate the $\Phi^{\mathrm{Si}}_{\mathrm{n_{eq}}}$ values, as shown in Fig. 6.12b and 6.12c. However, the scenario is reversed in the region around the pixel detector (Fig. 6.12a) at low radii, where other particles give the more significant contribution. This observation is further supported by the color map in Fig. 6.13. In the ITk the neutron-induced damage is dominant in the endcap region.

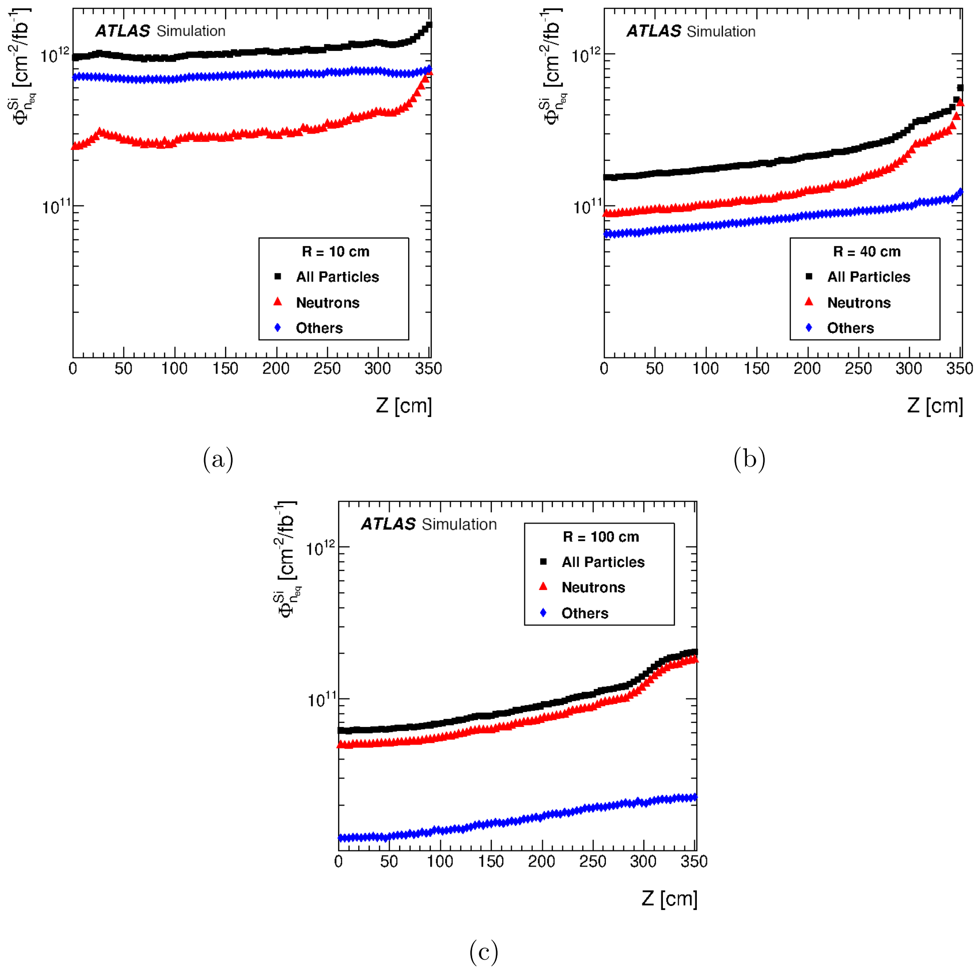

Figure 6.12.: $\Phi^{\mathrm{Si}}_{\mathrm{n_{eq}}}$ in different radial regions with a barrel and end-cap moderator density of $\rho = 0.99\,\mathrm{g/cm^3}$.

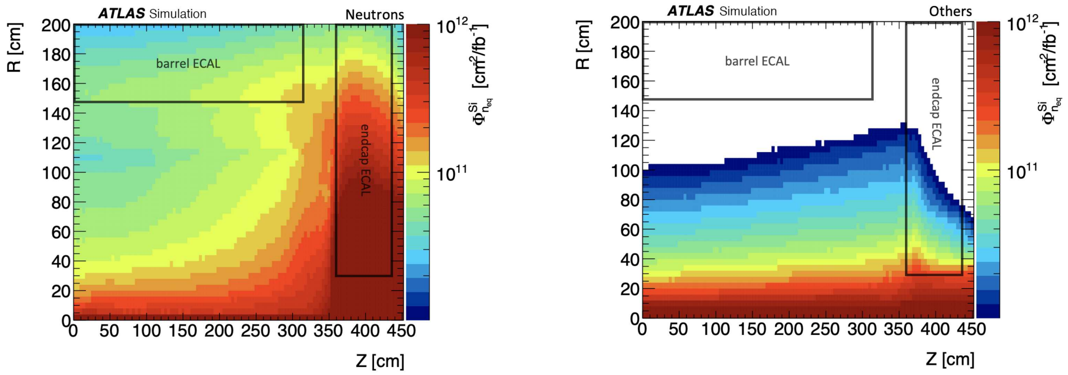

(a) (b)

Figure 6.13.: $\Phi^{\text{Si}}_{\text{n}_{\text{eq}}}$ in the ITk caused by neutrons (left) and all the other particles except neutrons (right). The barrel and end-cap moderator densities are $\rho = 0.99\,\text{g/cm}^3$.

6.2.6. Effect of Boron Doping in Moderators and the Corresponding Hydrogen Loss on Silicon Damage

The incorporation of boron results in a reduction of hydrogen density within the moderator material. As a consequence, the moderating effect diminishes, leading to an increase in the number of high-energy neutrons. In this section, results from FLUKA simulations are presented, focusing on the moderators in the ATLAS geometry. Specifically, the $\Phi^{\text{Si}}_{\text{n}_{\text{eq}}}$ is calculated within the ITk region using the barrel moderator composed of pure polyethylene, B4C, and boric acid-doped PE (while the composition of the endcap remains unchanged at 5% B). The material composition for B4C is provided in Tab. 6.5 and for boric acid-doped PE in Tab. 6.6, and the extent of hydrogen loss due to boron doping is detailed in Tab. 6.7.

Material	Mass Fraction
Carbon	0.813
Hydrogen	0.137
Boron-11	0.04
Boron-10	0.01

Table 6.5.: Mass fractions of the B4C-doped compound with total density $\rho = 0.99\,\text{g/cm}^3$.

Material	Mass Fraction
Carbon	0.6114
Oxygen	0.2220
Hydrogen	0.1166
Boron-11	0.04
Boron-10	0.01

Table 6.6.: Mass fractions of the boric acid compound with total density $\rho = 1.07\,\text{g/cm}^3$.

Fig. 6.14a presents a comparison between pure PE and PE-B4C at $R = 100$ cm. Upon observing the ratio, a subtle effect of approximately 0.7% is discernible. In a similar manner, Fig. 6.14b juxtaposes pure PE with boric acid-doped PE, yielding a ratio of approximately 2.1%. These findings are in line with the results illustrated in Fig. 6.11,

Material	Partial Hydrogen Density	Eff. Reduction of Mod. Thickness (cm)
Pure PE	0.14143	-
B4C doped PE	0.13563	0.25
Boric Acid	0.124762	0.63

Table 6.7.: Different moderator materials

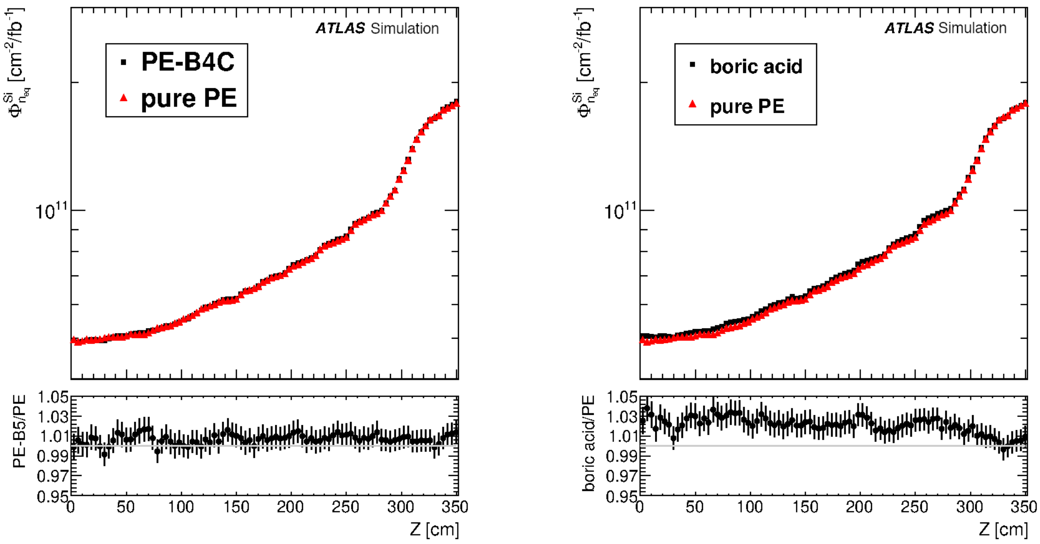

(a) (b)

Figure 6.14.: Comparison of different material compositions of the ITk barrel moderator. (a) shows the result for an idealised 5 % BPE moderator with which the $\Phi^{\mathrm{Si}}_{\mathrm{n_{eq}}}$ increases by about 0.7 % compared to pure polyethylene; (b) for boric acid with which the $\Phi^{\mathrm{Si}}_{\mathrm{n_{eq}}}$ increases by about 2.1 %.

and are consistent with the degree of hydrogen reduction provided in Tab. 6.7. The modest impact at $R = 100$ cm is unsurprising, as the thickness falls within the plateau region of the curve depicted in Fig. 6.11. A smaller thickness (e.g., 2 cm instead of 5 cm) would result in a steeper slope in Fig. 6.11, consequently magnifying the effect.

6.2.7. Comparison of FLUKA Results with Point-Wise and Group-Wise Neutron Transport to Geant4 Results

To fully harness the advantages of employing two independent simulation frameworks, concurrent studies using Geant4 were conducted. While FLUKA holds a well-established position in radiation simulations with a rich historical background, Geant4 derives its strength from the highly detailed and actively maintained ATLAS geometry description. In Fig. 6.15, density maps of the ITk are presented for both MC codes. These maps not only depict the overall density but also highlight the densities of boron and hydrogen individually. This separation is particularly significant as differences in the presence of these elements are of special interest in this study.

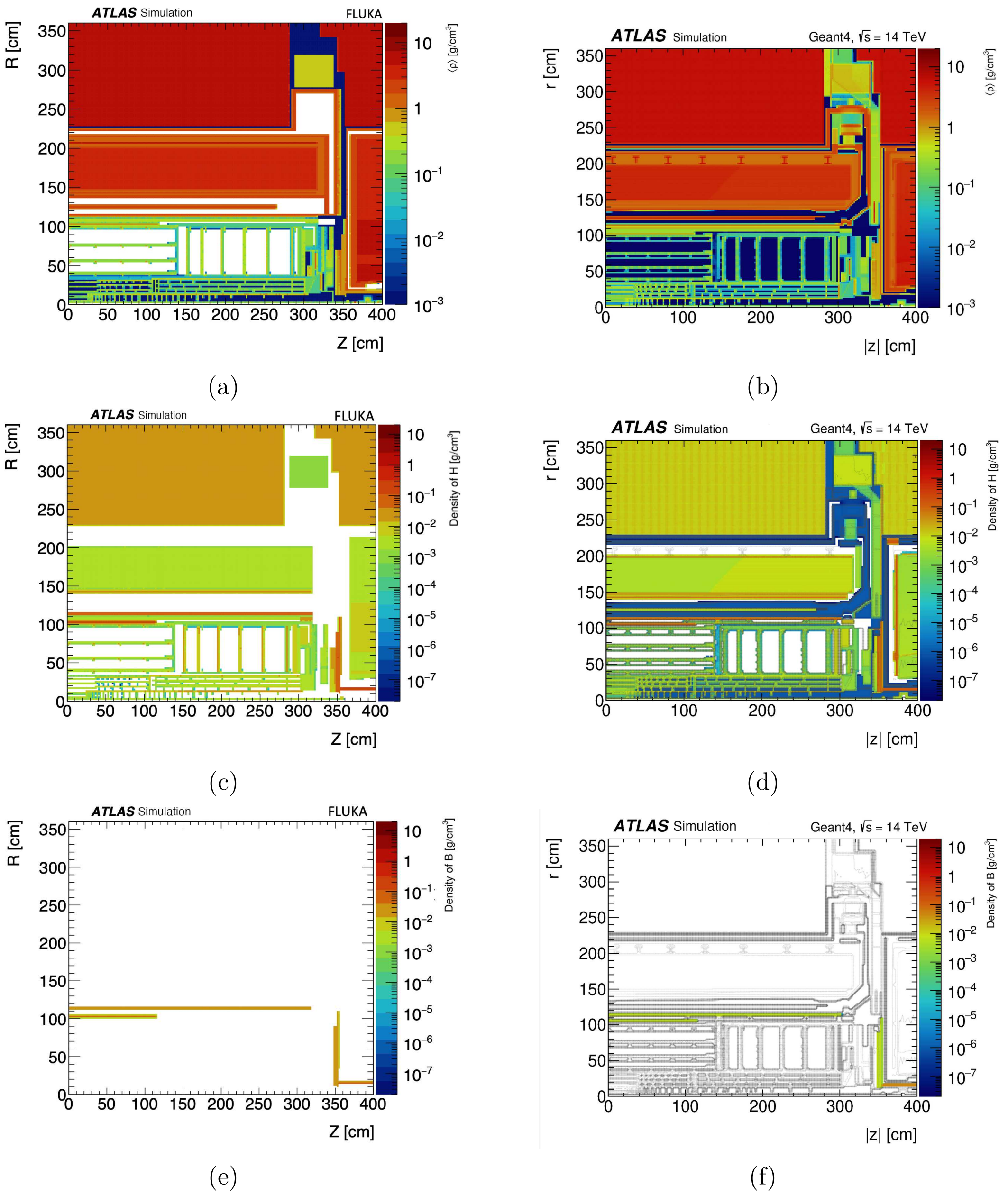

Figure 6.15.: ITk density maps of FLUKA (left) and Geant4 (right). Plotted is the total density, the hydrogen density and the boron density.

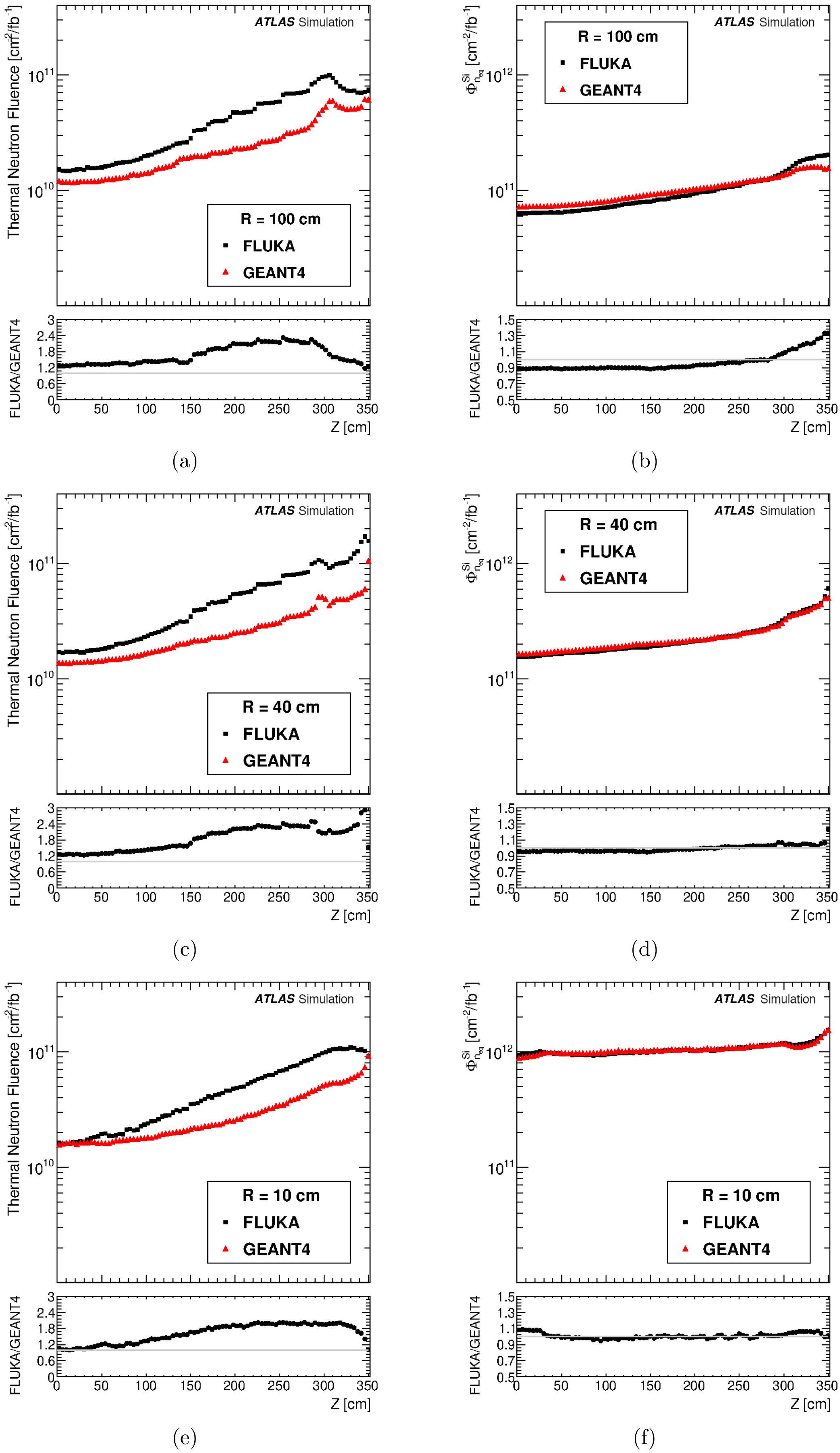

Figure 6.16.: Thermal neutron fluence and $\Phi^{\mathrm{Si}}_{\mathrm{n_{eq}}}$ results of FLUKA and Geant4 are compared at different radii.

In the comparison of the two Monte Carlo codes, the focus is solely on the scenario with 5 % boron content. Fig. 6.16a, 6.16c, and 6.16e illustrate that FLUKA tends to predict higher thermal neutron fluence at all three radii. This discrepancy could possibly arise from differences in geometry descriptions and/or variations in material compositions between the codes. However, when examining the comparison of $\Phi_{\mathrm{n_{eq}}}^{\mathrm{Si}}$ at the corresponding radii, as depicted in Fig. 6.16b, 6.16d, and 6.16f, a better agreement is evident. The influence of small differences in geometry or material compositions on $\Phi_{\mathrm{n_{eq}}}^{\mathrm{Si}}$ is less pronounced, given its domination by > 100 keV neutrons and other fast hadrons.

The difference highlighted in Fig. 6.16b at $R = 100$ cm, from $Z \approx 300$ to 350 cm, could potentially be attributed to an elevated hydrogen density in the Geant4 geometry. This can be observed in Fig. 6.15c, where a thin layer slightly above $Z = 370$ cm, extending from $R \approx 30$ to 200 cm, exhibits an increased hydrogen density not visible in FLUKA.

Fig. 6.17 provides a comparison of the neutron spectra between Geant4 and FLUKA. The results from the latter are divided into group-wise and point-wise neutron transport.

Within the thermal region, the FLUKA results obtained using point-wise neutron transport display slightly better agreement with Geant4 results (also point-wise). This indicates that a portion of the disparity between FLUKA group-wise and Geant4 outcomes could stem from distinct transport methodologies. Nevertheless, the magnitude of this difference is minor, underscoring that multigroup transport remains a sound approximation. For neutrons exceeding thermal energies, the outcomes of both point-wise and group-wise approaches are effectively congruent.

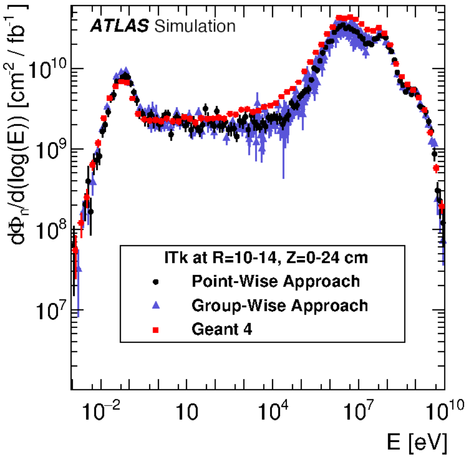

(a)

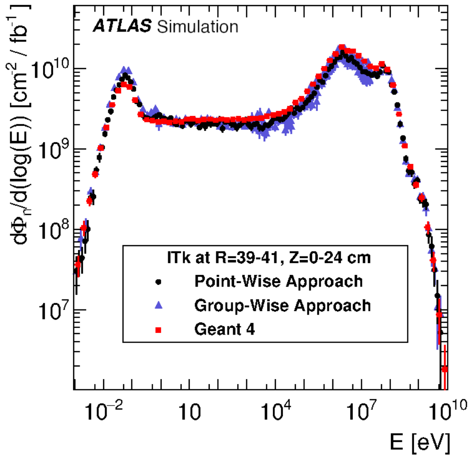

(b)

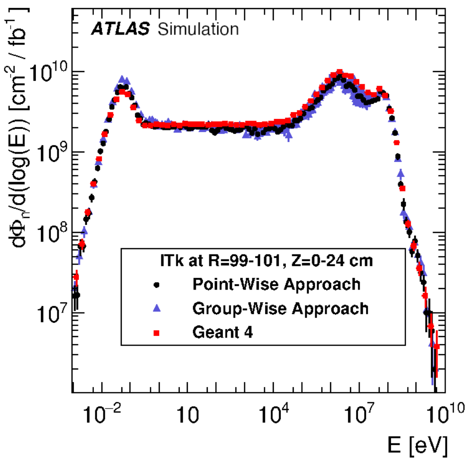

(c)

Figure 6.17.: Neutron fluence on the y-axis and energy on the x-axis. The fluence peak between 10^{-2} and 10^{0} eV is caused by thermal neutrons. In this particular energy range, the group-wise FLUKA approach gives the highest, and the point-wise Geant4 approach the lowest results. The point-wise FLUKA approach, implemented in 2022 [5], lies in between. At higher energies, the different FLUKA approaches give equivalent results. Again for different radii and results averaged in z.

6.3. Shielding for Cooling Sensors

During the ongoing Run 3, problems have emerged with sensors installed during LS2 near the cavern wall beyond 20 meters from the beam. The observed erratic behavior on the sensors was suspected to be caused by SEU. Addressing this, the choice of an optimal, space-efficient shielding material is crucial to lower the fluence that might cause SEU and to ensure sensor reliability. FLUKA simulation were employed to study shielding alternatives. The sensors are located on top of a water tank that is installed on the ground floor of the cavern. Exact coordinates of their positioning and an illustration of their surrounding is given in Appendix B in Fig. B.3.

Particle spectra, shown in Fig. 6.18, of the concerned region are taken from the visualization tool described in Section 5.2. The primary particles for the FLUKA simulation are sampled from this sepctrum. In addition, the particle type is sampled from the spectrum, but at these coordinates the number of protons and pions is very low, as visible in Fig. 6.18. As generic geometry a hollow sphere is used with a radius of 25 cm and 25 mm wall thickness. The particle fluence is evaluated in the center. The geometry of the simulation setup is shown in Fig. 6.19. The compared shielding materials are

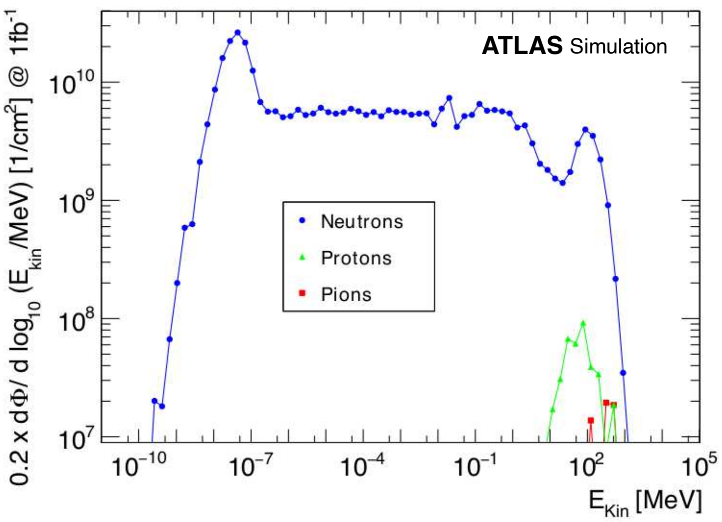

Figure 6.18.: Used particle spectra of neutrons,protons and pions from the corresponding area in the ATLAS Cavern. Data taken from [81].

- polyethylene
- iron
- polyethylene doped with 1 % boron (SWX-201HD1Z from Shieldverx)

As a reference, the simulation is run with vacuum as shielding material.The spectrum then corresponds to the original spectrum used for the sampling. For the visualization

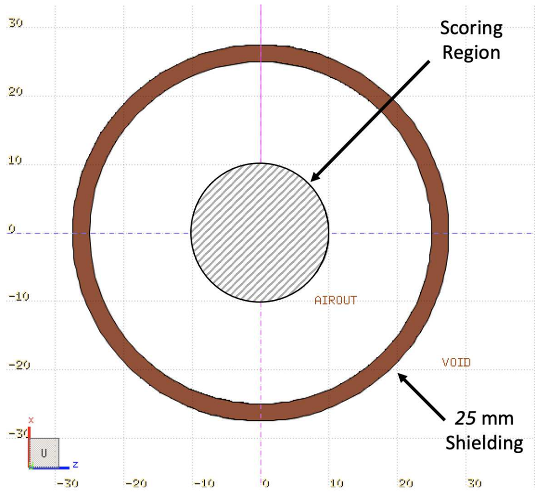

Figure 6.19.: Generic FLUKA geoemtry to study different shielding materials.

of the results in Fig. 6.20, the neutron spectra results of the different shielding materials are then divided by this reference spectrum.

The shielding simulations revealed that polyethylene proved effective for neutrons between thermal energies and ≈ 20 MeV. It was observed that neutrons were successfully thermalised within the shield. However, a noteworthy outcome is an increase of the thermal fluence, which would have doubled the SEU rate if these were due to thermal neutrons, i.e. to the thermal neutron reaction $^{10}\mathrm{B}(n,\alpha)^{7}\mathrm{Li}$ as described in Section 4.2.3. For high-energy neutrons the effectiveness of borated polyethylene was comparable to that of pure polyethylene. However, the presence of boron in the material leads to efficient capture of thermal neutrons, further enhancing its shielding capabilities. In contrast, an iron shielding with 25 mm thickness was found to be insufficient for effectively shielding high-energy neutrons and hadrons. Fig. 6.20 shows that a thin iron layer is effective primarily against low-energy neutrons.

Thus, it can be concluded that a borated PE shielding would be a reasonable choice for the given scenario. If that caused the SEU to disappear, it could be concluded that the presumed SEU were caused by thermal neutrons. If caused by high energy neutrons, the SEU would not disappear, because SEUs from non-thermal neutrons are typically caused by neutrons above $O(3)$ MeV, and for these energies, the shielding would have no effect, as shown in Fig. 6.20.

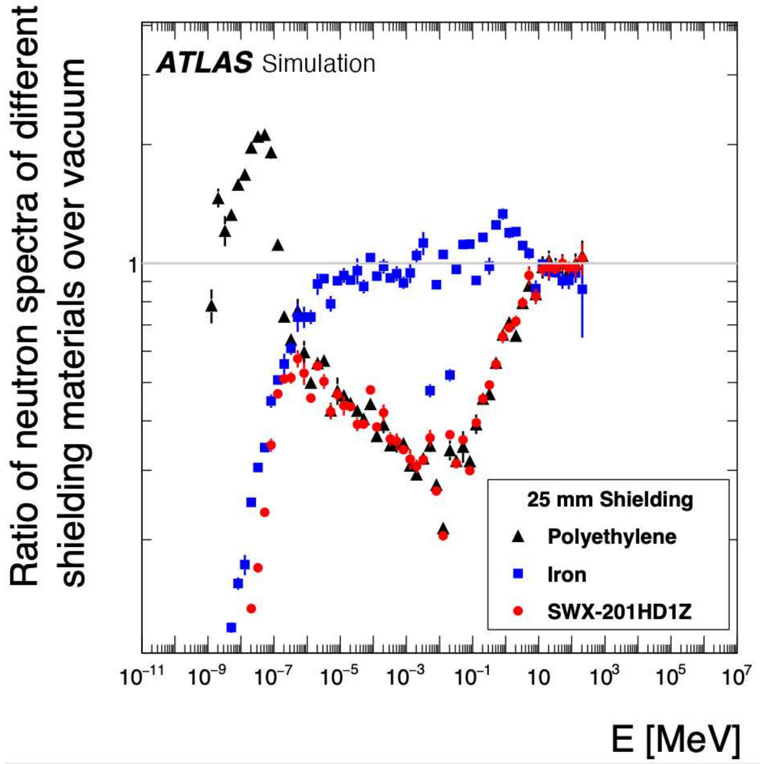

Figure 6.20.: Performance of different shileding materials, in particular the visualization of neutrons that passed the 25 mm thick shielding. SWX-201HD1Z represents polyethylene doped with 1 % boron composited by Shieldverx. Uncertainties are statistical only.

6.4. Simulation Studies of the Vacuum Assembly for eXperimental area (VAX)

Fig. 6.21 illustrates the FLUKA geometry where the LUCID-2 detector is located close to the position where the new vacuum equipment is foreseen. For HL-LHC LUCID-2 needs to be removed to make place for the new VAX of the Phase 2 upgrade. The implementation of the new geometry in FLUKA is illustrated in Fig. 6.22. To investigate the two LUCID-3 proposals and the relocation of the VAX key quantities, including fluence of e^- and e^+ and $\Phi^{\mathrm{Si}}_{\mathrm{n_{eq}}}$ are considered.

The markers 1 to 6 in Fig. 6.23 denote potential locations for fiber bundles within a fiber detector. Markers 4 and 5 designate positions for a detector connected to the VAX and the beampipe cone, while the remaining markers illustrate alternative locations if the fiber detector is affixed to the forward shielding.
The numerical values corresponding to the specified locations can be found in Tab. 6.8. The results show, for the $\Phi^{\mathrm{Si}}_{\mathrm{n_{eq}}}$, there is negligible difference between attaching the detec-

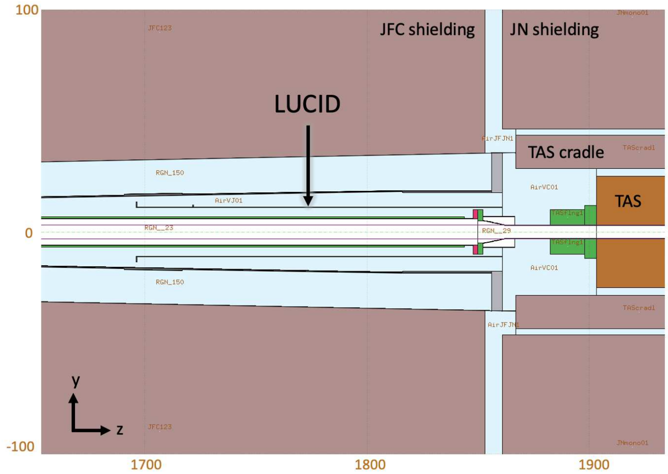

Figure 6.21.: Reference FLUKA geometry before the implementation of the new vacuum equipment. Light-blue areas are composed of air and white ones of vacuum, each other color represents different materials. All values are given in cm.

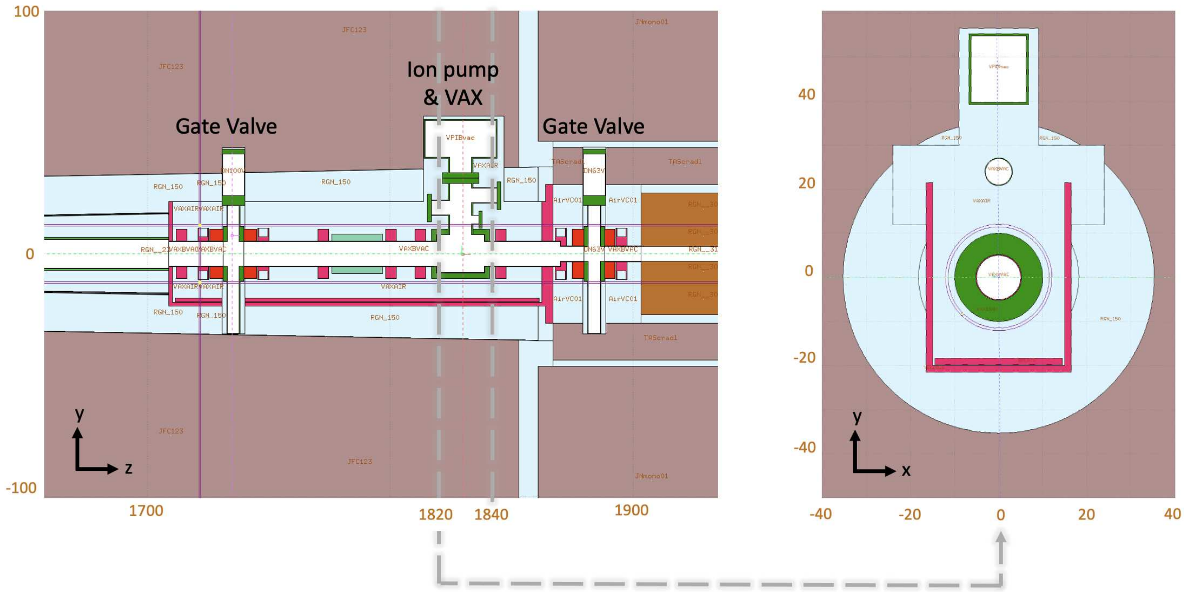

Figure 6.22.: FLUKA geometry of the implemented Vacuum Assembly for eXperimental area (VAX) of the Phase 2 detector. On the left the ZY plane, on the right the XY plane at $Z = 1820$ cm. Light-blue areas are composed of air and white ones of vacuum, each other color represents different materials. The U shaped component visible on the right, is made of aluminium. All values are given in cm.

tor to the beampipe or the shielding. Similarly, the e^+e^- fluence, indicating the signal rate within the detector, exhibits no substantial variance across different locations. Expectations leaned toward a significantly lower $\Phi^{\mathrm{Si}}_{\mathrm{n_{eq}}}$ when LUCID is fixed on the shielding, making these results unexpected and noteworthy.

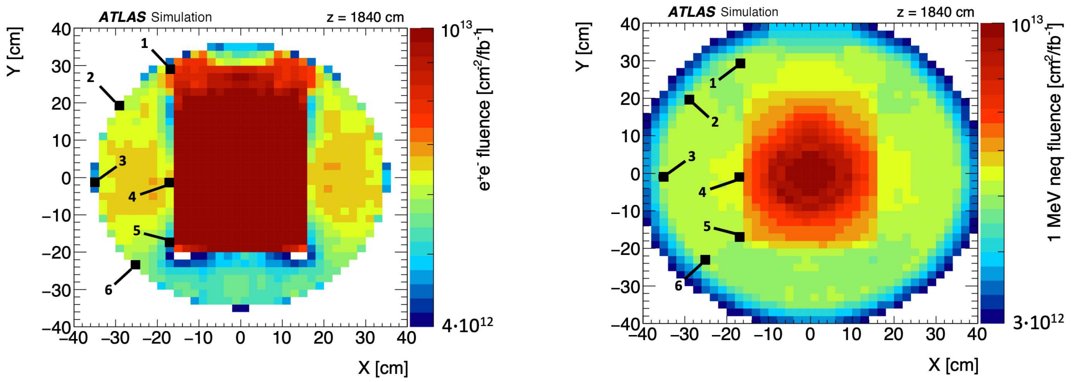

(a) (b)

Figure 6.23.: Results from FLUKA simulations depicting the Vacuum Assembly for eXperimental area (VAX) within the ATLAS detector. The color maps illustrate (a) e^- and e^+ fluence and (b) Si 1 Mev neq fluence. Marked are six locations of interest.

Position	e$^+$e$^-$ fluence (cm^{-2}/fb^{-1})	Si 1 MeV neq fluence (cm^{-2}/fb^{-1})
1	$4.53 \pm 0.08 \times 10^{12}$	$4.94 \pm 0.06 \times 10^{12}$
2	$5.95 \pm 0.09 \times 10^{12}$	$5.11 \pm 0.06 \times 10^{12}$
3	$4.67 \pm 0.08 \times 10^{12}$	$5.07 \pm 0.05 \times 10^{12}$
4	$6.47 \pm 0.11 \times 10^{12}$	$5.55 \pm 0.07 \times 10^{12}$
5	$4.82 \pm 0.11 \times 10^{12}$	$4.94 \pm 0.05 \times 10^{12}$
6	$5.96 \pm 0.08 \times 10^{12}$	$5.06 \pm 0.06 \times 10^{12}$

Table 6.8.: Numeric results from FLUKA simulations of the Vacuum Assembly for eXperimental area (VAX) within the ATLAS detector, encompassing e$^+$/e$^-$ fluence and Si 1 MeV neq fluence. Location numbers correspond to Fig. 6.23, indicating their positions. Additional column presents new data.

The results in Fig. 6.23 reveal a peculiar phenomenon characterised by sharp edges in the color maps within the aluminum region, resembling a distinct shape. By scrutinizing the spectra both inside and outside the aluminum region, it was found that different transport cut-off energies cause this phenomenon, 100 keV on the outside and 1 keV on the inside. Since this study concentrated on electrons above 100 keV, the results and conclusions are unaffected. However, given that this is a strong example of the impact energy cuts have on fluence outcomes, the topic will be investigated in the following.

The abrupt transitions in energy cut-off limits across various regions are responsible for the sharp edges observed in the color maps. To illustrate this problem and to investigate the importance of properly chosen transport limits, a simple FLUKA simulation is set up in the following Fig. 6.24 shows the cylindrical geometry. An electron beam starting at $Z = 0$ hits a copper target. Behind the target with a width of 10 cm is a region with 10 cm of air, then another target of 3 cm aluminium and eventually another region of air again. Three simulations were performed with different energy transport cuts. In one of them each transport cut-off is at 100 keV, in another all cut-off limits are at 100 keV except for the aluminium target, for which it is 10 MeV and in the third all cut-off limits are at 100 keV except for the air region at $Z > 23$ cm, equivalent to the scenario in the ATLAS simulation above.

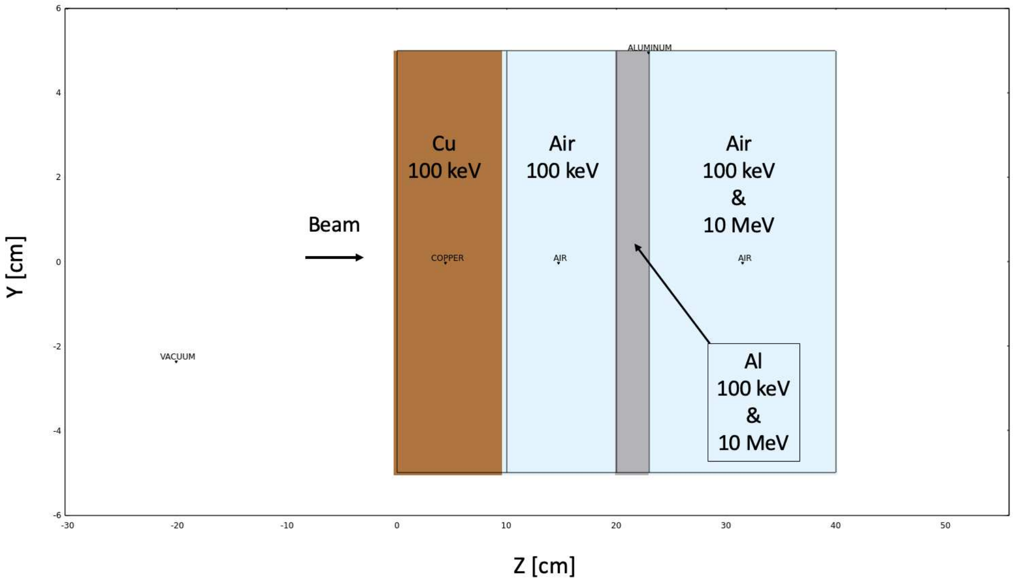

Figure 6.24.: Cylindrical FLUKA geometry to study the effect of different energy cuts. The energy values represent transport cuts, for each region.

Fig. 6.25 depicts the results with a 100 keV cut in each region. The region transitions appear smooth, considering the different materials. The electron beam penetrates the copper target and produces showers also in the aluminium target.

Fig. 6.26 shows the results with a 10 MeV cut within the aluminium target and 100 keV everywhere else. Below 20 cm electrons are transported down to 100 keV. Within the aluminum target, a sudden cutoff occurs, allowing only electrons above 10 MeV to be transported, resulting in a distinct transition in the fluence map. Consequently, only electrons exceeding 10 MeV reach behind the aluminium target.

The histogram in Fig. 6.27 presents the results of all three simulation setups. First the scenario with 100 keV cuts everywhere is compared to the scenario with a 10 MeV cut at the aluminium target. Below $Z = 20$ cm, just before the aluminium target, the effects

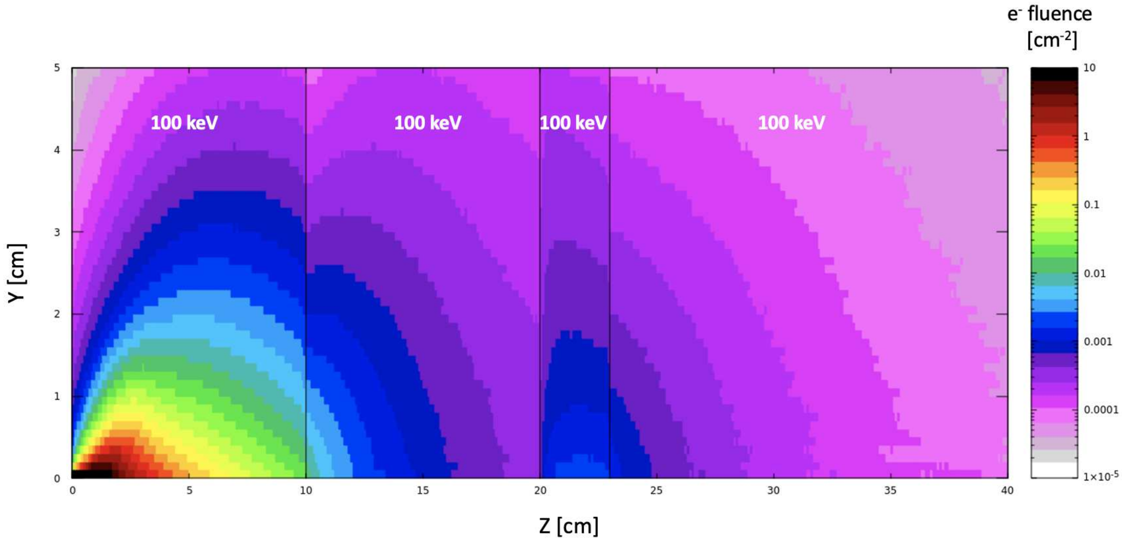

Figure 6.25.: Simulation results showing the electron fluence distribution within the specified geometry. The energy values represent transport cuts, for each region. In this scenario the cut-off energy is uniformly set at 100 keV throughout the entire geometry.

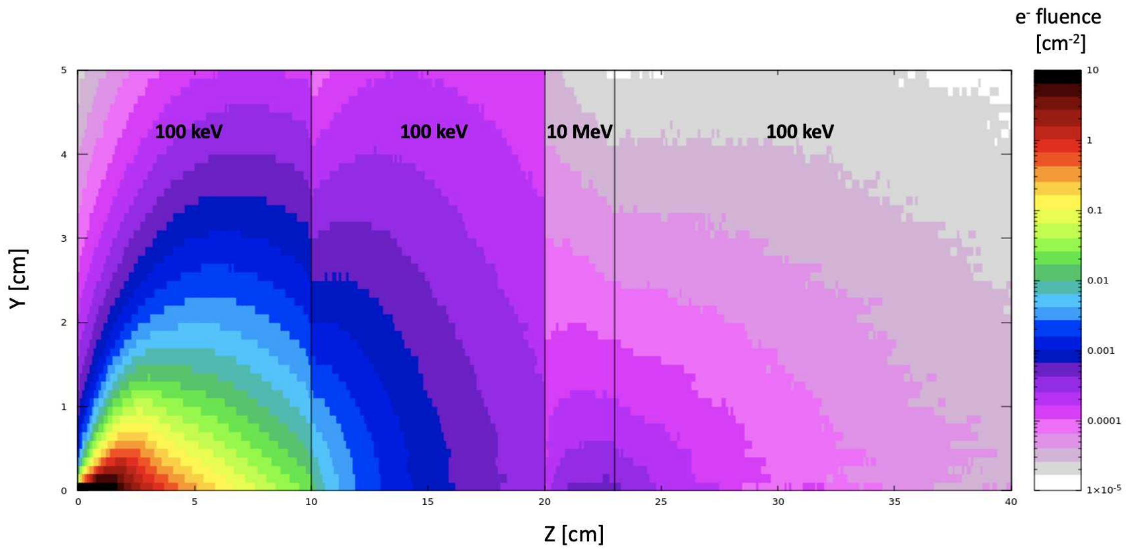

Figure 6.26.: Simulation results showing the electron fluence distribution within the specified geometry. The energy values represent transport cuts, for each region. In this scenario the transport cut-off energy is set at 100 keV, except for the aluminium target from 20 cm to 23 cm, where it is 10 MeV.

of different energy cuts become evident. The reduction in backscattered electrons due to the 10 MeV cut explains the discrepancy in this region. Inside the aluminium target, electron showers are initialised, and again, the higher cut-off results in a reduction. Beyond $Z = 23$ cm, after the aluminium target, where the transport cut-off reverts to 100 keV, all electrons with energies below 10 MeV are already excluded. The result of the third scenario with a 10 MeV cut in the air region at $Z > 23$ cm corresponds to the scenario of the ATLAS simulations in Fig. 6.23. Like for the second scenario, the higher cut-off results in a fluence reduction. Whether the 10 MeV cut is in the aluminium at $Z < 23$ cm or the air at $Z > 23$ cm, at $Z > 23$ cm the reduction based on the given limit is the same.

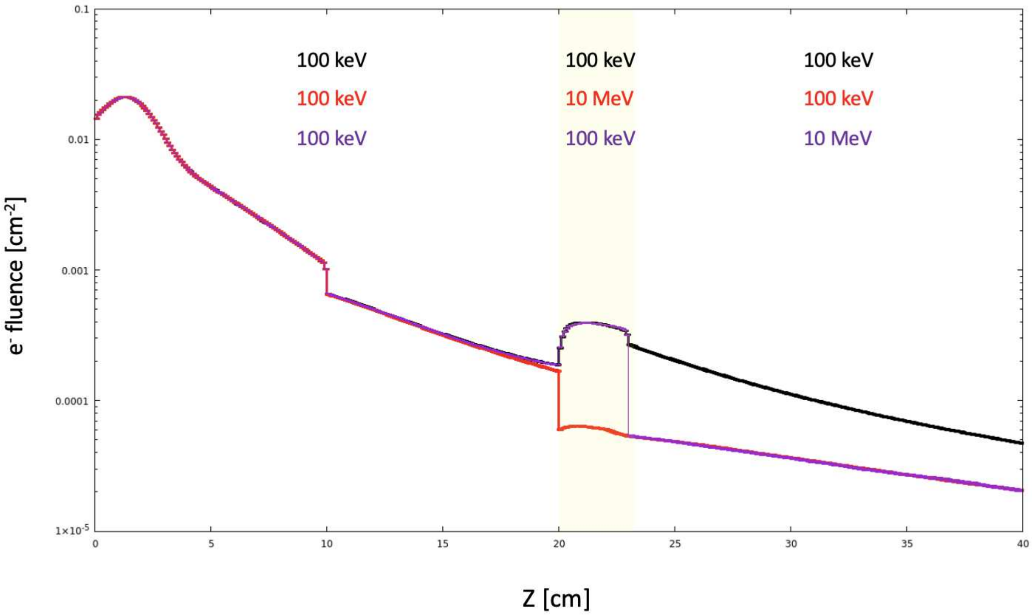

Figure 6.27.: Comparison of simulation results showing electron fluence for different energy limits of electron transport. The black line represents a cut-off below 100 keV, while the red line corresponds to a mixture of 10 MeV and 100 keV cut-offs. The shaded region marks the aluminium target between $Z = 20$ cm and $Z = 23$ cm, where the transport limits differ.

7. Reevaluation of Displacement Damage Factors, Considering π^- and Other Particles Stopping in Si

Charged pions are the primary contributors to bulk damage inflicted on silicon detectors situated near the interaction point of hadron colliders, in particular the LHC; as illustrated in the FLUKA results in Fig. 7.1.

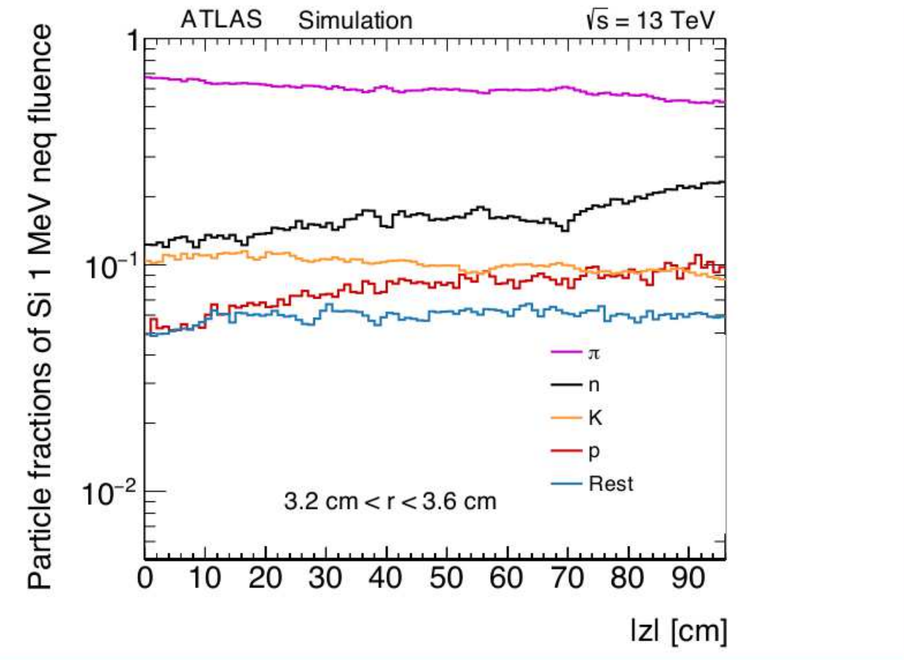

Figure 7.1.: FLUKA results of particle fractions of the Si 1 MeV neutron equivalent fluence $\Phi^{\mathrm{Si}}_{\mathrm{n_{eq}}}$ around the IBL layer in the ATLAS pixel detector. Leptons are not shown, because FLUKA does not consider them for the $\Phi^{\mathrm{Si}}_{\mathrm{n_{eq}}}$.

This is due to their high fluence, as described in Section 3.2.1. As a result of the scarcity of high-intensity pion beams, research into the displacement damage caused by pions in silicon has been limited to a very restricted energy range, spanning from 100 MeV to 400 MeV, as documented in [83–85]. As outlined in Section 4.2.2, it is typically presumed that bulk damage is directly related to NIEL. However, it is acknowledged that certain

particles and silicon material variations can lead to deviations from this proportional relationship [16]. As discussed in Section 4.2.2, hardness factors are utilised to quantify damage from different particle types and energies. These factors relate the NIEL cross section of a certain particle type to that of 1 MeV neutrons. Over three decades ago, hardness factors for pions were approximated by scaling the damage induced by protons through a rather basic approach [13]. Despite the method's inherent simplification, these damage factors have been incorporated into a compilation by the RD48 collaboration and have been widely adopted within the particle physics community ever since [11]. Section 7.1 introduces a new estimation of pion damage factors, based on new methods, including the Robinson formalism [86].
The extent of damage is calculated by multiplying the particle tracklength by the corresponding damage factor. However, when it comes to particles that stop within the silicon, the hardness factors do not include their contribution, because the tracklength of a stopped particle is zero. As a result they are not accounted for when estimating $\Phi^{\mathrm{Si}}_{\mathrm{n_{eq}}}$. In particular, when a negatively charged pion comes to rest in the material, it will be captured by a nucleus and induce a nuclear reaction with a significant amount of energy distributed as kinetic energy of emitted particles and nuclear fragments. Sopped positively charged pions on the other hand are negligible, because they encounter Coulomb repulsion, deflecting them away from the positively charged nucleus instead of being captured. Section 7.2 explores this damage contribution of stopped negative pions and other particles, that has so far not been accounted for in hardness estimations, including that of the RD48 collaboration. It assesses their impact on existing factors and ultimately demonstrates the importance of this study by revealing discrepancies between simulation results and ATLAS data, attempting to explain a long-standing mystery in the silicon pixel detector [19]: this mystery involves the Insertable B-Layer (IBL) and three pixel layers (Pix1, Pix2, Pix3) with increasing R from the beam line, described in Section 2.2.4. Fig. 7.2 shows that the IBL data has a much steeper Z shape than the results of different simulation frameworks estimate. This discrepancy of simulation results and data has been a long-standing issue [20].

7.1. Reassessing RD48 Damage Factors for π Using Robinson's Parametrisation

In this section damage factors for pions are assessed and compared to existing ones from the RD48 compilation. For that purpose Rutherford, nuclear elastic and inelastic scattering is considered. To estimate to what extent these interactions contribute to non-ionising losses, the formalism from Robinson [86] is applied.

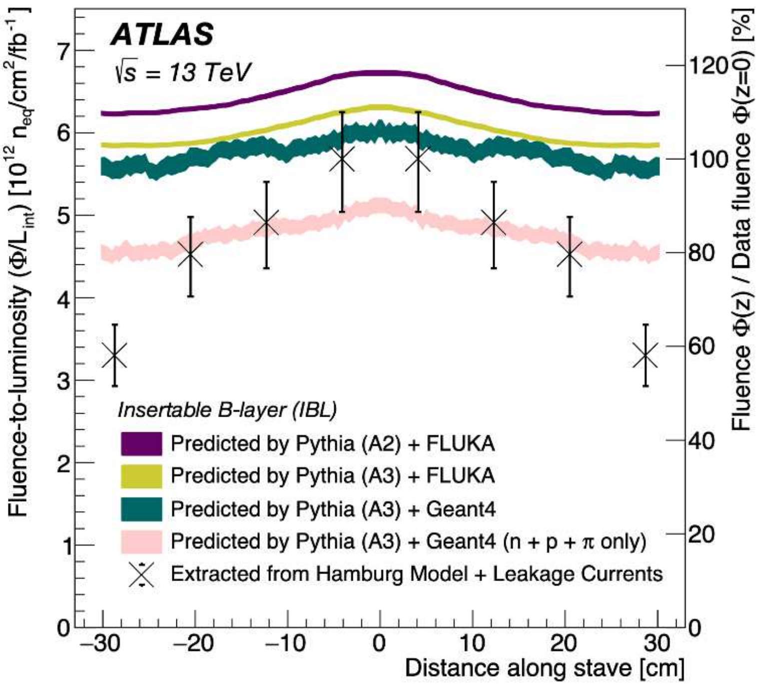

Figure 7.2.: The discrepancy of IBL damage as a funciton of Z has long been a mystery. The data shows a much steeper Z shape than different simulation results do. Taken from [20].

7.1.1. Computational Method

The event generators of FLUKA are utilised to generate hadron-nucleus collisions, in particular of π^--Si collisions for a range of pion energies. Thus, a realistic estimation of the size and energy of the recoil nucleus is obtained, considering nuclear elastic and inelastic interactions. These outcomes are extended to lower energies with a simple Rutherford scattering model to produce the elastic recoil atoms. This model is based on the basic Rutherford scattering formula for the differential cross section [58]

$$\frac{\mathrm{d}\sigma}{\mathrm{d}\Omega} = \left(\frac{1}{4\pi\varepsilon_0}\frac{Z_1 Z_2 e^2}{4E_0}\right)^2 \frac{1}{\sin^4\left(\frac{\vartheta}{2}\right)}. \tag{7.1}$$

Where $\frac{\mathrm{d}\sigma}{\mathrm{d}\Omega}$ is the differential cross-section, which represents the probability of scattering into a given solid angle, ε_0 is the permittivity of free space. Z_1 and Z_2 are the atomic numbers of the incident pion and the silicon nuclei, respectively. e is the elementary charge and E_0 is the kinetic energy of the incident particle. ϑ is the scattering angle.

The energy transfer of the Rutherford scattering is calculated, as outlined in [87], as

$$p_{\text{out}} = \frac{p_0 \cdot \cos(\theta)\left(x_t \cdot e_0 + x_p^2\right) + (e_1 + x_t)\sqrt{(x_t \cdot e_0)^2 - (x_p \cdot x_t)^2 - (x_p \cdot p_0 \cdot \sin(\theta))^2}}{(e_0 + x_t)^2 - (p_0 \cdot \cos(\theta))^2}. \tag{7.2}$$

p_{out} denotes the momentum of the scattered particle. p_0 represents the initial momentum of the incident particle (pion) and e_0 stands for the total energy of it. x_p represents the rest mass of the incident - and x_t of the target particle.

Considering the size of the silicon atom, it becomes unreasonable to utilise the Rutherford formula for impact parameters exceeding the atom's dimensions. This can be avoided by requiring a minimum energy transfer [1]. In this study the cut is set at 0.1 eV.

The Robinson formalism allows for extracting the NIEL from the total losses. In [88] the dimensionless variable ϵ is introduced as

$$\epsilon = E/E_L \tag{7.3}$$

with

$$E_L = \frac{Z_1 Z_2 e^2}{a_{12}} \frac{1 + A}{A}. \tag{7.4}$$

a_{12} serves as a screening length employed within the Thomas-Fermi description of atoms [89]

$$a_{12} = \left(\frac{9\pi^2}{128}\right)^{\frac{1}{3}} \frac{a_H}{\sqrt{Z_1^{2/3} + Z_2^{2/3}}} \tag{7.5}$$

$$\tag{7.6}$$

with the Bohr radius $a_H = 52.92$ pm.

The deposited non-ionising energy can then be calculated as

$$E_{\text{NIEL}} = \frac{E}{1 + k_L \cdot g(E/E_L)} \tag{7.7}$$

[1] Alternatively, a cut could be applied at the impact parameter $b(\theta)$ directly.

with recoil energy E and

$$g(\epsilon) = \epsilon + 0.40244\epsilon^{3/4} + 3.4008\epsilon^{1/6} \tag{7.8}$$
$$\tag{7.9}$$

and

$$k_L = \frac{32}{3\pi}\sqrt{\frac{m_e}{M_2}}\,\frac{(1+A)^{3/2} Z_1^{2/3} Z_2^{1/2}}{\left(Z_1^{2/3} + Z_2^{2/3}\right)^{3/4}} \tag{7.10}$$
$$\tag{7.11}$$

with M_2 being the mass of the target material, and A is the ratio of the masses of the ion and target atom.

Eq. (7.7) is given in units of MeV. In order to obtain the NIEL cross section, E_{NIEL} needs to be multiplied by the cross section of the corresponding interaction given in mb.

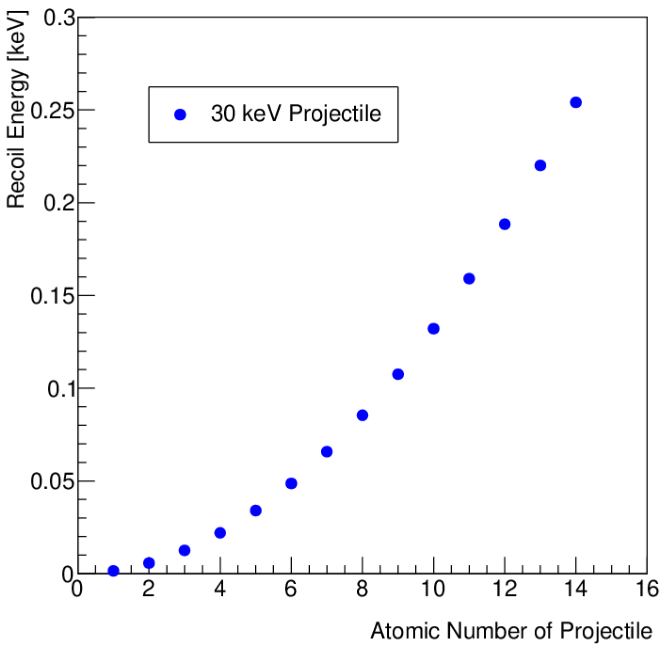

Figure 7.3.: Non-ionising fraction of the recoil energy as a function of the atomic number for 30 keV projectiles impacting a silicon target. Each ion's mass number is twice its atomic number.

Fig. 7.3 illustrates the non-ionising recoil energy for 30 keV projectiles with atomic numbers ranging from 1 to 14 impacting a silicon target. The results demonstrate that the non-ionising recoil energy increases with the atomic number.

7.1.2. Results and Comparisons

The NIEL of silicon recoils produced by negative pions, multiplied by the cross section for Rutherford scattering, is shown in Fig. 7.4. The calculation is based on Eq. (7.1) and Eq. (7.2). The product of total energy deposition and differential cross section remains relatively constant at high pion energies, ranging from 6×10^2 MeV to 4×10^4 MeV. However, it increases sharply, becoming dominant for low energy pi-Si events. The product of the total is shown together with the non-ionising fraction, computed with Eq. (7.7). For high energy pions between 6×10^2 MeV to 4×10^4 MeV the difference between the total and the NIEL contribution is about 40 %, while it decreases for smaller energies to about 15 % for 1 MeV pions.

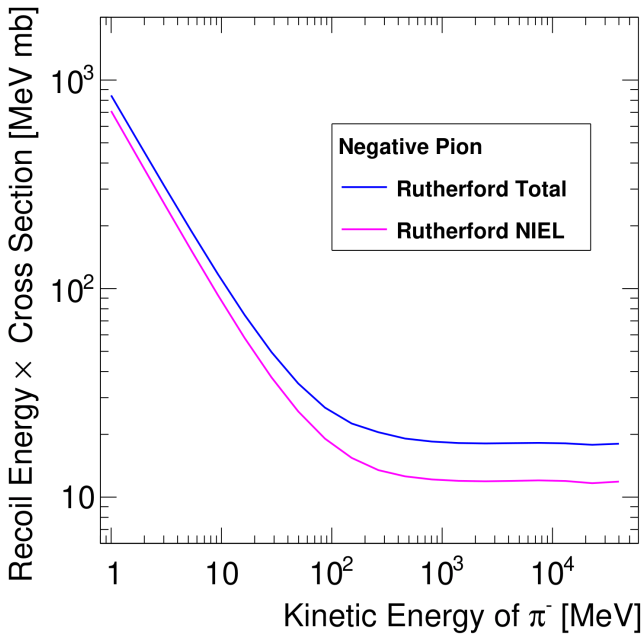

Figure 7.4.: Product of the recoil energy and the differential cross section for Rutherford scattering in silicon as a function of the kinetic energy of incident pions. The plot includes two scenarios: the total Rutherford cross section and the NIEL contribution.

The average recoil energy from nuclear elastic interactions is presented in Fig. 7.5. The total energy deposition is shown together with the non-ionising fraction. Both curves peak around a kinetic pion energy of 30 MeV. Above that energy both curves are relatively constant and dominate the average recoil energy below 30 MeV. At the peak value the average recoil energy of the total and the non-ionising fraction differs by about 65 %, similar as for larger pion energies.

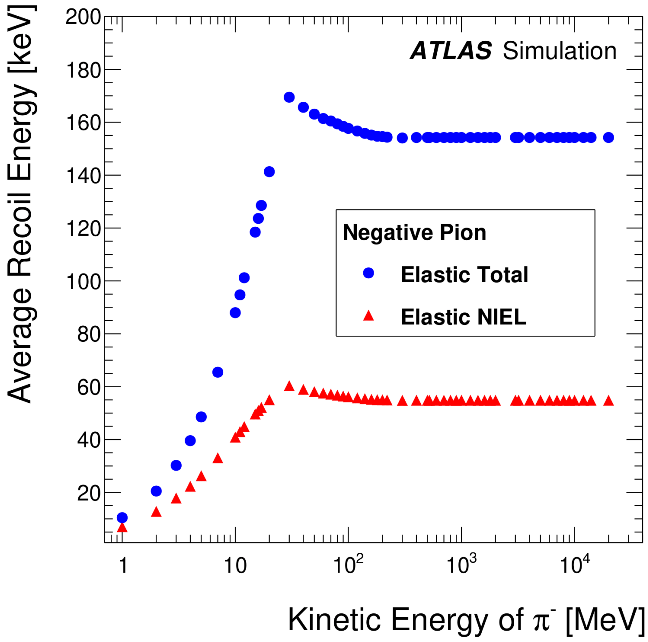

Figure 7.5.: Average recoil energy of silicon atoms as a function of the kinetic energy of incident negative pions based on nuclear elastic scattering. The plot considers the total energy deposition and the non-ionising fraction.

The total energy deposition from nuclear inelastic interactions is illustrated in Fig. 7.6a. As the recoils of inelastic π-Si interactions contain recoils of different Z, Fig. 7.6a shows the results summed over all recoils, those of $8 < \mathrm{Z} < 12$ and $\mathrm{Z} \geq 12$. The results show that the addressed Z ranges contribute weakly to the total energy deposition of high pion energies (above 1×10^2 MeV). The given Z ranges contribute to the sum over all Z about 30 % for low energy pions (around 10 MeV) and only about 5 % for 2×10^4 MeV. This is because the dominant high energy recoils consist of particles with low atomic number. If recoils of all Z are considered, the average recoil energy increases with increasing pion energy. The trend of the addressed Z ranges, is vice versa. Considering total energy deposition, recoils of $8 < \mathrm{Z} < 12$ possess higher energies than those of $\mathrm{Z} \geq 12$, mainly because they are lighter.

The non-ionising fraction is shown in Fig. 7.6b for the same Z intervals. Considering only non-ionising interactions, the trend of the summed up recoils with different Z decreases with increasing pion energy. Around 100 MeV is a pronounced peak. The given Z ranges contribute 10 to 30 % to the sum over all Z and thus, are more relevant to the non-ionising deposition, compared to the total. Further, if the non-ionising fraction is considered, recoils of $\mathrm{Z} \geq 12$ dominate those of $8 < \mathrm{Z} < 12$. This is because projectiles with higher atomic numbers deposit more non-ionising energy as it is shown in Fig. 7.3.

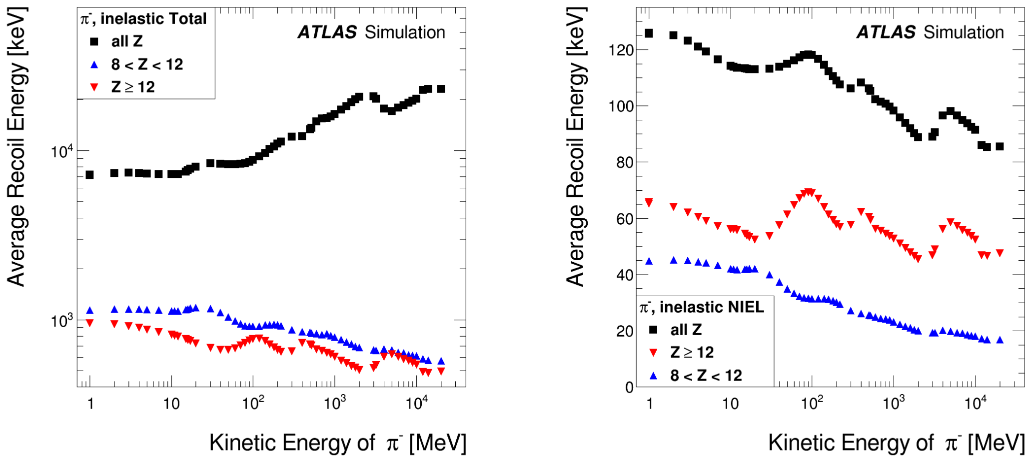

(a) (b)

Figure 7.6.: Average recoil energy of silicon atoms as a function of the kinetic energy of incident negative pions based on nuclear inelastic scattering. (a) considers the total energy deposition and (b) the non-ionising fraction. Both graphs distinguish for recoils with varying Z. Only (a) uses a logarithmic y-scale. (a) and (b) are normalised per event.

Fig. 7.7 presents the cross sections of nuclear elastic and inelastic scattering for a range of pion energies. Both have a peak around 100 MeV, where they differ by about 30 %. When calculating the NIEL cross sections for nuclear elastic and inelastic interactions, the cross sections shown in Fig. 7.7 are needed to obtain the results presented in Fig. 7.8.

Fig. 7.8 displays the NIEL cross section of negative pions as a function of its kinetic energy. Including contributions from nuclear elastic, nuclear inelastic and Rutherford scattering. Below approximately 12 MeV, Rutherford scattering prevails as the dominant contribution, whereas above this threshold, nuclear inelastic scattering emerges as the primary contribution. The display of the nuclear elastic contribution abruptly ends below 20 MeV, because of missing cross sections in FLUKA as displayed in Fig. 7.7. In Fig. 7.9 the results are compared to the RD50 [13] values, also based on simulation results. Additionally the new estimates are compared to a measured value from [85]. The effect of the re-evaluated values on ATLAS simulation outcomes, together with the consideration of stopping particles, is discussed in Section 7.2.3.

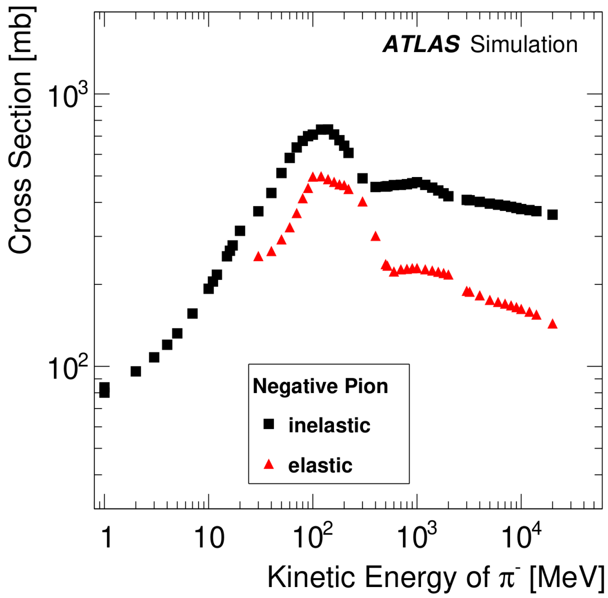

Figure 7.7.: Cross sections of nulcear elastic and inelastic scattering for π^- - Si events for a range of energies.

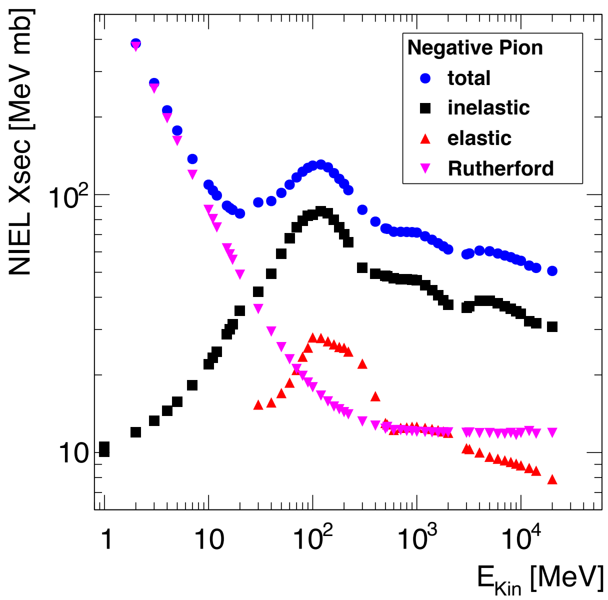

Figure 7.8.: Non-Ionising Energy Loss as a function of the kinetic energy of negative pions. The results are based on the FLUKA event generator for nuclear elastic and inelastic scattering and calculated Rutherford scattering. To get the non-ionising fraction, a parametrisation by Robinson [86] is applied.

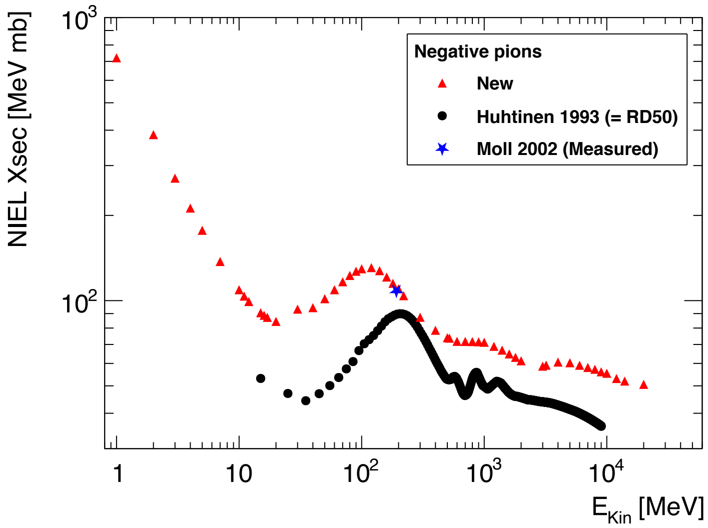

Figure 7.9.: Comparison between the new estimates of non-ionising energy loss from negative pions to the values used by RD50 [13], based on simulation outcomes. Additionally the outcome of a measurement from [85] is shown.

7.1.3. Deriving a normalisation for the 1 MeV neutron equivalent fluence

The 1 MeV neutron equivalent fluence is commonly used to normalise atomic displacement damage in silicon semiconductor devices [17]. Determining the average displacement damage caused by neutrons around 1 MeV in silicon is challenging due to the pronounced neutron cross section resonances in this energy range. Averaging over a narrow energy interval introduces variability that is sensitive to the selected upper and lower bounds. For the displacement damage at 1 MeV, this variability can lead to differences of up to 20 % [90]. To address this issue, the original method to define it, described in [17], can be employed. Based on this the the value of the new damage estimations at 1 MeV is re-evaluated to achieve a self-consistent normalisation, meaning that the same simulation tools for pions and neutrons are used.

The basic approach from [17] involves minimising χ^2

$$\chi^2 = \sum_i W(E_i)\Delta E_i \left[D'(E_i, A, B) - D(E_i)\right]^2 \tag{7.12}$$

with respect to the parameters A and B, where

$$D'(E_i, A, B) = A \cdot E_i \cdot \left(1 - e^{-\frac{B}{E_i}}\right). \tag{7.13}$$

The minimisation method employed here is in accordance with [17] and involves deriving two simultaneous equations by taking the partial derivative of χ^2 with respect to A and the partial derivative of χ^2 with respect to B. These equations are then solved numerically to determine the values of A and B.

At energy E_i, $D(E_i)$ denotes the NIEL cross section of the ith tabulated value and ΔE_i represents the local mesh size for the tabulation. In [17] $A = 124$ and $B = 1.49$. $W(E_i)$ is a representative neutron spectrum peaking around 1 MeV to take into account the NIEL cross section of neutrons in this particular energy range. It is shown in Fig. 7.10 and taken from [91].

Fig. 7.11 demonstrates the relationship between neutron energy and new displacement damage results in silicon. The parameters $A = 131.935$ and $B = 1.215$ were optimised to closely match the experimental results. These values are reasonably close to those reported in [17]. Additionally, the resulting displacement damage value $D(1\text{ MeV}) \approx 92.8$ MeV mb, agrees well with the commonly used value of 95 MeV mb. With this result, the new displacement damage values can be normalised consistently.

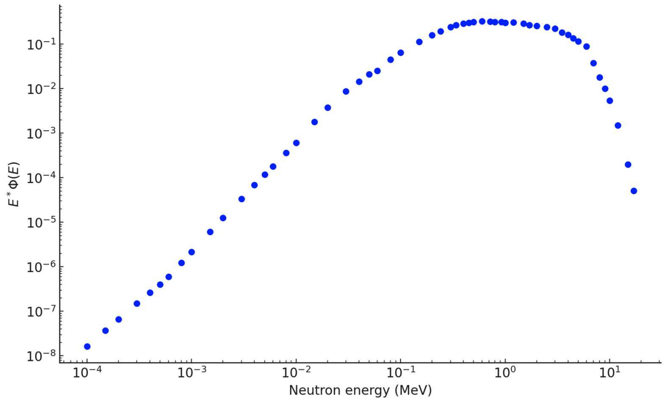

Figure 7.10.: Representative neutron spectrum peaking around 1 MeV. Taken from [91].

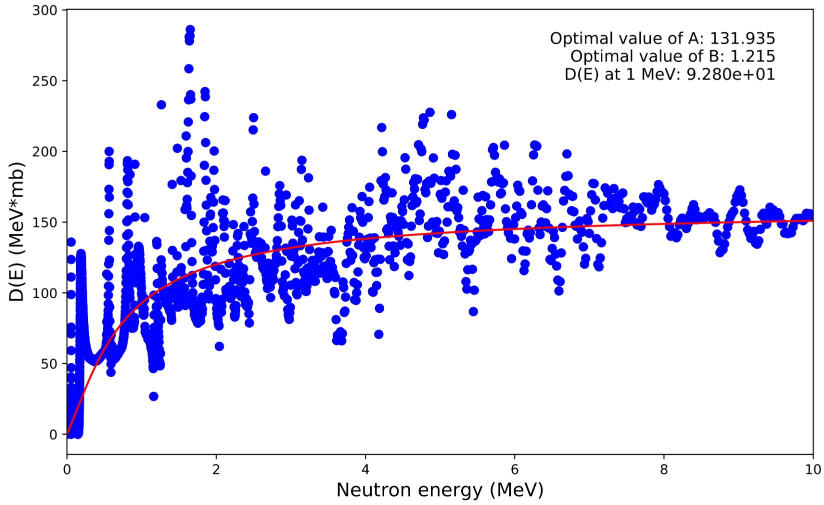

Figure 7.11.: Blue points show displacement damage results for neutrons. The red curve is based on the function $D(E) = A \cdot E \cdot \left(1 - e^{-\frac{B}{E}}\right)$ with optimised values A and B. According to [17] this curve is used to approximate the displacement damage of 1 MeV neutrons.

7.2. Impact of π^- and Other Particles Stopping in ATLAS Pixel Layers

An analysis of simulated proton-proton collisions occurring at LHC energies in the ATLAS geometry was conducted. The analysis involved estimating the $\Phi^{\mathrm{Si}}_{\mathrm{n_{eq}}}$ resulting from particles that stop within thin silicon sensors in the pixel detector [19]. FLUKA's transport routine KASKAD was used to identify particles that come to rest. Those with energies ≤ 1 eV were flagged as 'stopped' and their position and generation type (primary or secondary) were printed to a file. The number and distribution of these stopping particles within the pixel detector was recorded. Such was the location where these particles come to rest within the IBL and the Pixel layers 1-3.Apart from the discrepancy between data and simulation results, these layers are particularly interesting for this study, since their sensors are close to the IP, where low energy negative pions with the potential to stop, are abundant. Fig. 7.12 illustrates the counted negative pions that stopped in these layers. The results show that at low Z the majority of them are generation 1 particles, i.e. particles created in the p-p collision, if 0 cm $\leq z \leq$ 10 cm is considered. For larger Z, the amount of secondaries (particles of generation > 1) is dominant, increasing with Z, because with increasing Z, the number of interactions and thus secondary particles increases.

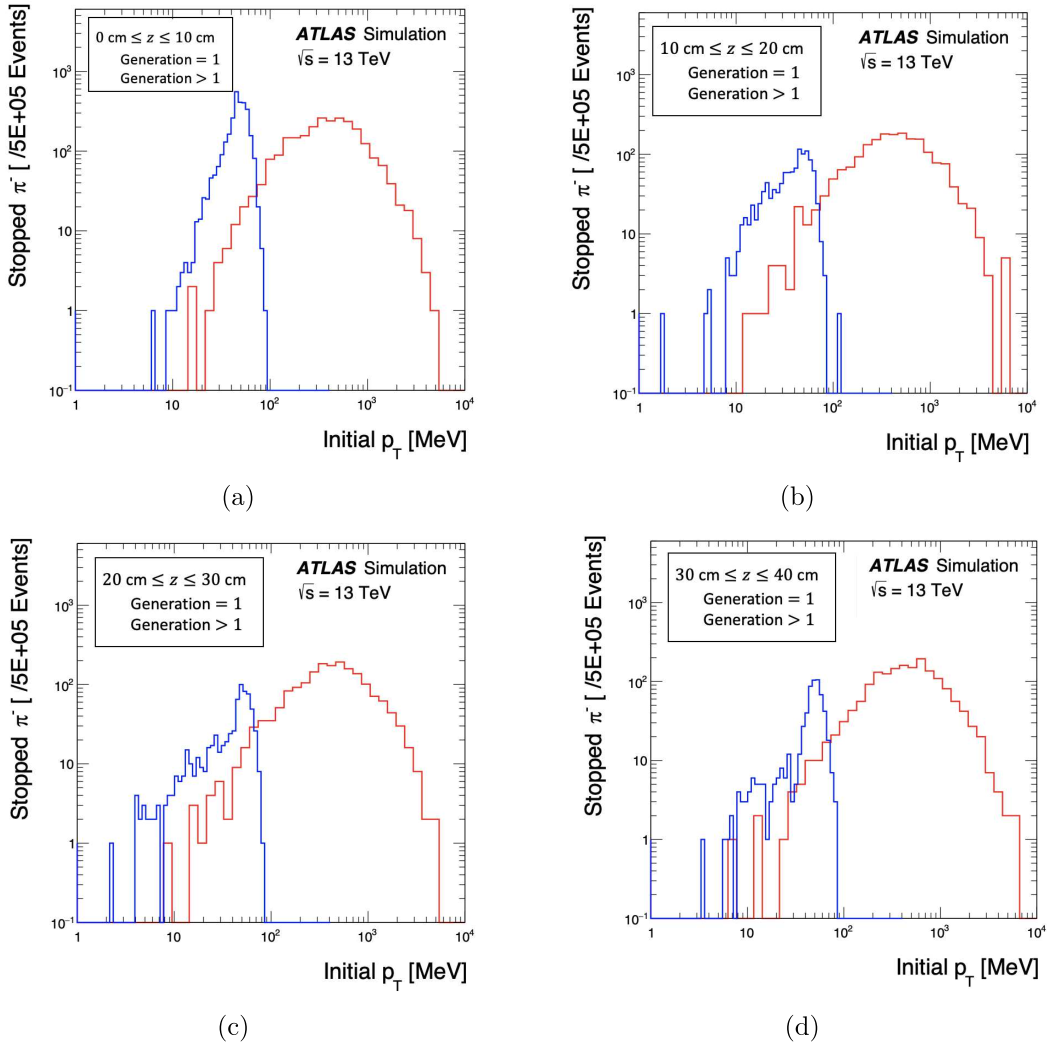

Figure 7.12.: p_T spectrum of stopping negative pions with 500,000 proton-proton collisions. The negative pions are distinguished in generation 1 and generation > 1, i.e. secondary particles. The values in the legend show the percentage of each generation group. The spectra are separated in 4 different z-regions as indicated in the legend.

The first generation particles that generate pions (generation > 1) that eventually stop, tend to exhibit higher initial p_T values throughout the observed z region. That is expected, since it is referred to the initial p_T. If the p_T of the actually scored generation, was plotted, these values would be lower.

Fig. 7.13 distinguishes negative pions that stop in the IBL and those that stop in the pixel layer 3. The majority of capture interactions in the IBL takes place at low Z. In Fig. 7.13a, depicting 0 cm $\leq z \leq$ 10 cm, a significant portion is captured in the IBL.

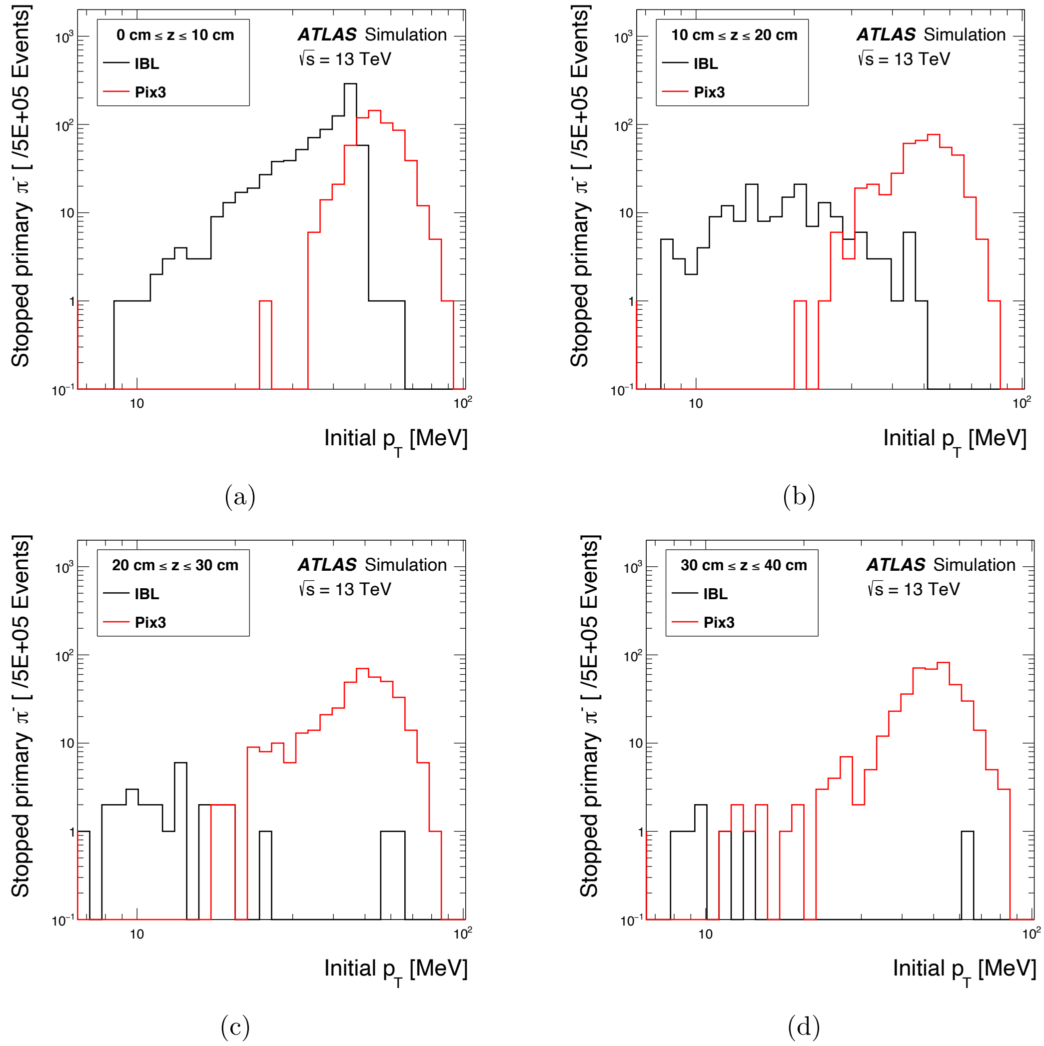

Figure 7.13.: p_T spectrum of stopping generation 1 negative pions with 500,000 proton-proton collisions. The pions are distinguished to those stopping in the IBL and those stopping in the pixel layer 3 (Pix3). The spectra are separated in 4 different z-regions as indicated in the legend.

That portion decreases with increasing Z, because with higher Z the momentum (and energy) is larger so the pions have a much larger range. Additionally the initial p_T, that the particles have immediately after the pp-collision, is lower for those stopping in the IBL at larger Z. The shifted peaks in Fig. 7.13a reveal a clear difference in p_T, required for the negative pions to either reach the IBL or the Pix3 before being captured. The spectrum of particles stopping in Pix3 is almost constant vs. z and shows similar fluences and p_T values for different z regions, in contrast to the IBL results. This is because to reach Pix3, a substantial amount of energy is required, making the crossing of individual silicon layers less significant causing a smearing out effect. The so far presented results already indicate, how the consideration of captured negative pions steepens the z-shape of the simulation results for the IBL, while keeping them constant around the Pix3.

7.2.1. Relating the Additional Contribution to Existing Damage Factors

Using FLUKA in combination with a user defined source routine, events of negative pions hitting silicon at different energies are generated. The fragments from each event are then fed into the Robinson formalism [86] to calculate the non-ionising contribution. The non-ionising energy deposition is presented for different pion energies in Fig. 7.14.

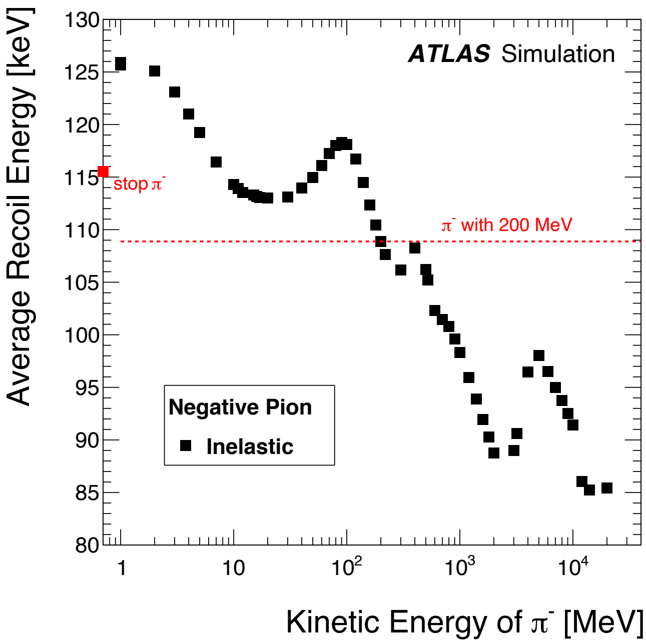

Figure 7.14.: Non-ionising energy deposition of negative pions in a quasi infinite silicon volume. Considered are only inelastic interactions. The energy deposition is simulated with FLUKA and the non-ionising fraction calculated with the Robinson formalism [86]. Since the x - axis is logarithmic, it does not include 0, but for the purpose of presenting a comparison to stopping negative pions, the value of zero kinetic energy is marked below 1 MeV with a red dot. Also the comparison to 200 MeV pions is illustrated with a red dashed line.

The results in Fig. 7.14 reveal that the nuclear fragments emitted upon pion capture, i.e. from stopping negative pions result in a similar non-ionising energy deposition per event as the fragments generated from reactions induced by 200 MeV pions. This finding is presented in more detail in Fig. 7.15, where the average recoil energy is plotted for recoils with $Z \geq 12$, $10 \leq Z \leq 11$ and $8 \leq Z \leq 9$ respectively. The average recoil energy summed over all Z is about 5 keV lower for 200 MeV than for stopping pions. Considering recoils of $8 \leq Z \leq 9$ the difference is similar. For recoils of $10 \leq Z \leq 11$ the stopping pions show an higher discrepancy by about 23 keV. For $Z \geq 12$ the order is reversed, and the 200 MeV pions surpass the stopping ones by about 20 keV.

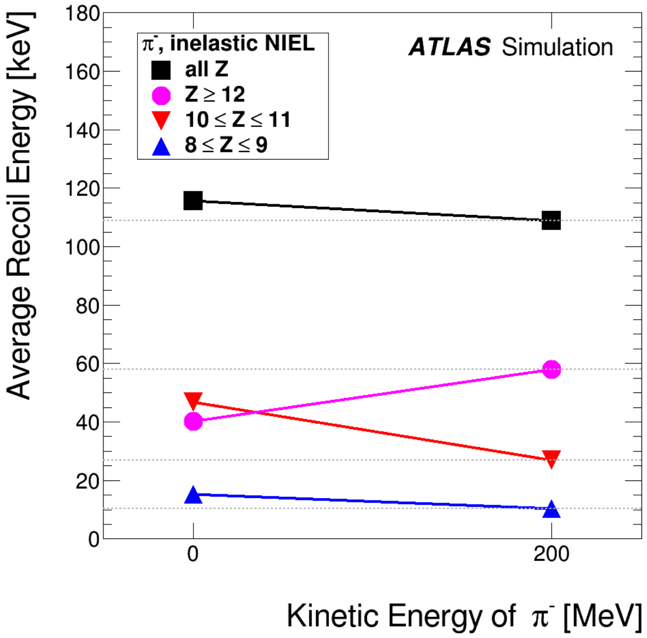

Figure 7.15.: Non-ionising energy deposition of negative pions in a quasi infinite silicon volume. Considered are only inelastic interactions. The energy deposition is simulated with FLUKA and the non-ionising fraction calculated with the Robinson formalism [86]. The values of 200 MeV pions and stopping ones (0 MeV) are compared for different recoils. The dashed lines mark the 200 MeV values.

Non-ionising energy deposition is given in MeV/event, while $\Phi^{\mathrm{Si}}_{\mathrm{n_{eq}}}$ is given in MeV mb. So in order to estimate the $\Phi^{\mathrm{Si}}_{\mathrm{n_{eq}}}$ of stopping negative pions, the cross section of 200 MeV negative pions in silicon can be considered, which corresponds to an inelastic interaction length of $\approx$ 30 cm [52]. With the ratio of the non-ionising energy deposition from 200 MeV over captured, i.e. 0 MeV negative pions the inelastic interaction length of 200 MeV pions can be weighted and thus, adopted for captured pions. Additionally to the weighting, it was considered that for captured pions only the inelastic contribution from Fig. 7.8 is relevant. Thus, a $\Phi^{\mathrm{Si}}_{\mathrm{n_{eq}}}$ value for stopping pions was obtained. In the next chapter, these findings are applied to the outcomes from Section 7.2, in order to re-evaluate simulation results, based on RD50 damage functions, where the $\Phi^{\mathrm{Si}}_{\mathrm{n_{eq}}}$ of captured pions was ignored.

7.2.2. Biasing Methods Used

Ultimately, the number of stopping particles in the silicon layers is small, necessitating numerous pp collision events in the FLUKA simulation to achieve results with sufficient statistical significance. Simulating all these events throughout the entire ATLAS cavern would be time-consuming, much of it spent unnecessarily, as our focus is solely on the results from the inner detector. Therefore, the black-hole material of the FLUKA code is employed to stop following particle tracks once they reach the hadronic calorimeters. Results were compared with a simulation involving the entire ATLAS geometry to ensure that the black-hole material in the hadronic calorimeters does not impact the results.

7.2.3. Results and Conclusions

The simulation results and data in Fig. 7.16 and Fig. 7.17 are normalised to one of the bins around $z = 0$ cm in order to compare only the shapes. The specific bins for the normalisation stand out due to their obviously exact agreement. The errors in the data are assumed to be fully correlated, resulting in their cancellation within the depicted ratio plots. Fig. 7.16 compares the z-variation of the IBL layer damage data with simulation results using RD48 factors (FLUKA built-in) labelled 'NIEL only', and the new factors that also consider stopping particles labelled 'NIEL + stopped'. From 0 cm $\leq |z| \leq$ 8 cm to 16 cm $\leq |z| \leq$ 24 cm the data drops by about 20 %; compared to about 9 % with the default FLUKA results and about 15 % with the new FLUKA results based on PYTHIA events (Fig. 7.16a). Thus, a significant improvement is evident through the modified FLUKA simulations. The sensor at 24 cm $\leq |z| \leq$ 32 is not considered, because it is based on a different (3D) technology and there are doubts if the leakage current measurements on planar and 3D sensors are comparable at this level. The simulation results in Fig. 7.16b based on EPOS events show a similar but somewhat inferior outcome, as they exhibit a slightly less pronounced z-dependence.

Unlike in the IBL layer, the available data-points of the sensors in the Pixel layers 1-3 are asymmetric with respect to $Z = 0$. Although, considering pp events within the symmetric detector, there should be perfect z-symmetry. Fig. 7.17a shows the results of the Pixel layer 1 based on PYTHIA events. From -15 cm $\leq z \leq$ 3 cm to -40.5 cm $\leq |z| \leq -20.5$ cm the data drops by about 14 %; in contrast, the default FLUKA results show a decrease of about 5 %, while the new FLUKA results display a reduction of around 10 %, again showing a significant improvement. The data, in Fig. 7.17 is inconsistent between positive and negative z. In Fig. 7.17a and Fig. 7.17b the negative z side of the data agrees better with the simulations than the positive one. At 3 cm $\leq |z| \leq$ 15 cm the data drops by about 13 %; compared to only about 1 % with the default FLUKA results and about 2 % with the new FLUKA results. The simulation results based on EPOS generally show weaker z-dependency; for the comparison to the sensor at -40.5 cm $\leq |z| \leq -20.5$ cm by about 2 %. Due to the poor performance of simulation results averaged around 3 cm $\leq |z| \leq$ 15 cm, the difference between PYTHIA and EPOS events is vanishingly small.
In Fig. 7.17c and Fig. 7.17d the positive z side of the data agrees better with the simulations. From -15 cm $\leq z \leq$ 3 cm to -40 cm $\leq |z| \leq -19$ cm the data drops by about 17.5 %; in contrast, the default FLUKA results even show an increase of about 1 %, while the new FLUKA results display a decrease of around 4.5 %. Relatively poor

agreement, but nonetheless, the modifications demonstrate a clear improvement. To 21 cm $\leq |z| \leq$ 40 cm the data drops by about 11 %; in contrast, the default FLUKA results again show an increase of about 1 % and a decrease about 4.5 % with the new FLUKA results. Also with respect to the results in this layer, the simulation results based on EPOS show less z-dependency.
In Fig. 7.17e and Fig. 7.17f the simulations show better agreement with the negative z side of the data. Again the NIEL with the consideration of sopped particles shows an improvement.
It can be concluded that the results in Fig. 7.16 and Fig. 7.17 are highly relevant for the radiation background studies of ATLAS. With the new considerations, the simulation results align significantly closer to the data, addressing a discrepancy that has been an ongoing puzzle for more than five years [20].

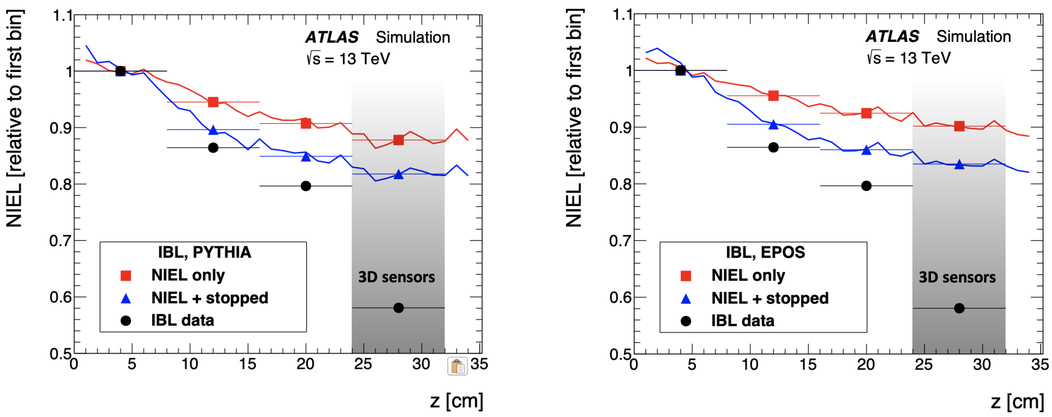

(a) (b)

Figure 7.16.: Simulation results of NIEL are compared to data from sensors in the IBL layer. Both the simulation and data values are plotted relative to the result of the sensor that is covering a region from 0 cm $\leq |z| \leq$ 8 cm. The horizontal lines across the black data marks indicate the range of averaging. Simulation results are represented using lines and are additionally marked to indicate the averaged $|z|$ coverage aligned with the data results. 'NIEL only' represents FLUKA results obtained with the default configuration, while 'NIEL + stopped' represents the results obtained with modified damage factors and the consideration of stopping particles. The values are plotted only for positive Z since they are symmetric around $Z = 0$ cm. The FLUKA outcomes are based on event files produced with PYTHIA in (a) and EPOS in (b). The data from the 3D sensor (marked with a black rectangle) is assumed to be not comparable.

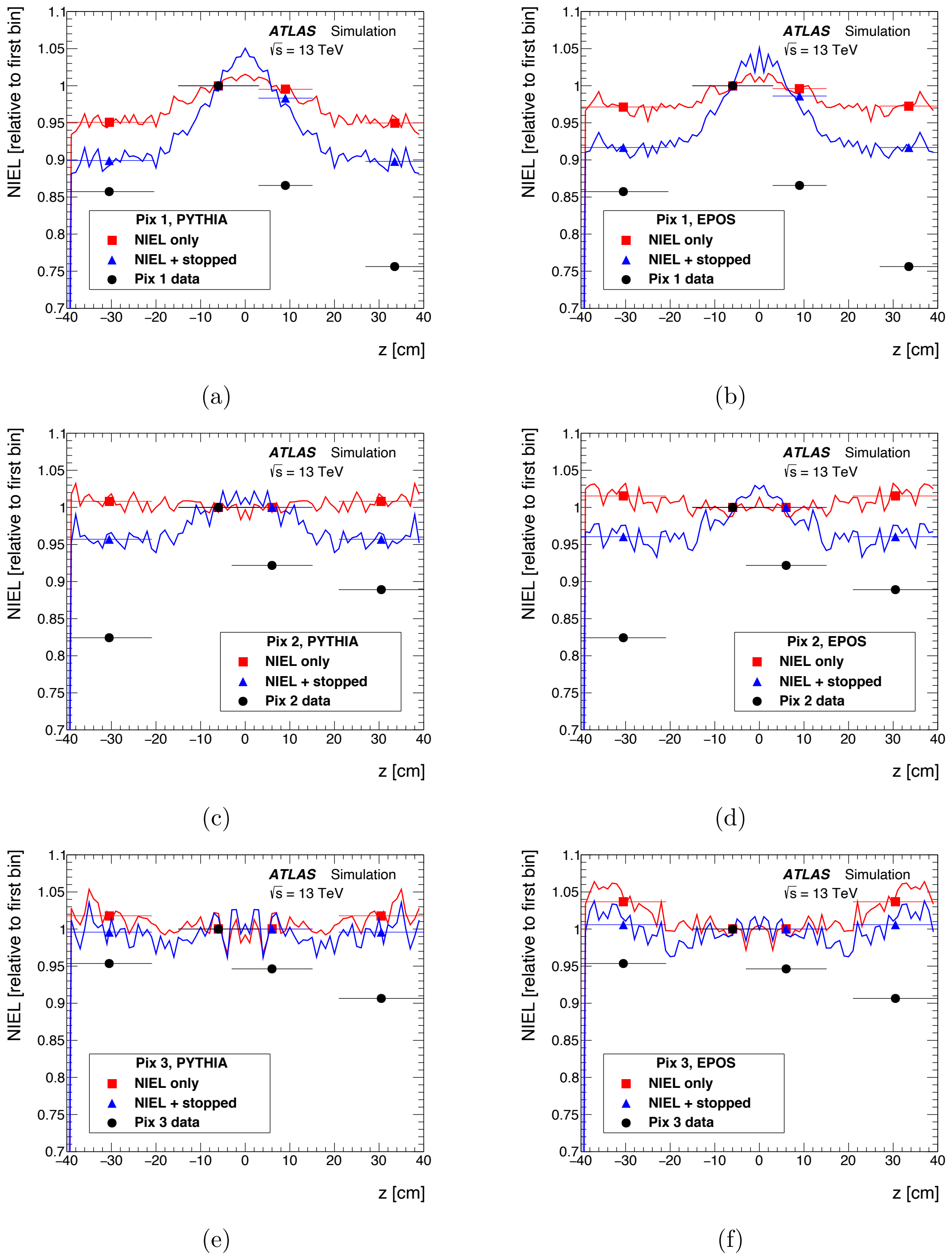

Figure 7.17.: Simulation results of NIEL are compared to data from sensors in the three Pixel layers. Both the simulation and data values are plotted relative to the result of the central sensor, covering a region from -15 cm $\leq z \leq +3$ cm. The horizontal lines across the black data marks indicate their coverage. Simulation results are represented using lines and are additionally marked to indicate the averaged Z coverage aligned with the data results. 'NIEL only' represents FLUKA results obtained with the default configuration, while 'NIEL + stopped' represents the results obtained with modified damage factors and the consideration of stopping particles. The FLUKA outcomes are based on event files produced with PYTHIA in (a) and EPOS in (b).

8. Summary and Conclusions

In this thesis, a comprehensive study of radiation shielding and displacement damage factors in the ATLAS detector at the LHC is presented. The research encompasses several different aspects, including the implementation of spatial binning in FLUKA for effective radiation background studies, exploration of neutron moderator configurations alongside other shielding concepts, and the reevaluation of displacement damage factors for negative pions based on a new approach.

The key outcomes of this thesis include the implementation of a spatial binning technique in the FLUKA code. This new recording approach allows the integration of simulation results into interactive webpages, facilitating the exploration of material composition, radiation quantities, and time dependent TID spectra of the detector. Looking ahead, the implemented spectrum binning techniques in FLUKA present an opportunity for enhancement. Integrating these techniques into FLUKA as a new input card would eliminate the need for double definitions with USRBIN. This improvement could be included in a future FLUKA upgrade, streamlining and enhancing its simulation capabilities.

To optimise the shielding of sensitive detector components, a simple toy model for effective moderator studies complements detailed investigations of radiation transport within the complex ATLAS geometry. The albedo of the plain electromagnetic calorimeter is investigated to establish a scale for moderator efficiency. Simulations with different boron content are conducted to assess the impact on thermal neutron fluence. Potential cross talk between different regions of the detector is studied by analysing neutron fluence direction cosines. The effect of reducing hydrogen density on neutron contribution to total equivalent fluence is examined, along with the effect of hydrogen reduction due to boron doping. From the results it's evident that transitioning from 5% to 1% boron content yields a marginal change compared to the shift from 1% to pure polyethylene. Therefore, for the Phase 2 upgrade of the inner detector, a boron-doped polyethylene moderator with a 5 cm thickness and 1% boron content proves optimal for both barrel and endcap positions.

Further, it was shown that the various concepts of the upgraded luminosity detector (LUCID 3) exhibit minimal differences concerning radiation damage.

A significant part of the research focused on the reevaluation of the displacement damage factors for negative pions. The study utilised Robinson's formalism [86] to reassess these factors. The new damage factors incorporate the contribution from stopping particles, a previously neglected aspect. Building on this, a long-standing mystery regarding the discrepancy between data from radiation sensors and simulation results in the pixel detector of ATLAS is now better understood.

Appendices

A. The FLUKA code

Since many of the findings in this thesis are based on FLUKA outcomes, this chapter introduces general concepts of the MC code, that have been relevant in setting up the simulations.

A.1. Geometry Description

FLUKA utilises a combinatorial geometry description, using bodies, zones, and regions. Bodies are basic geometrical objects placed somewhere in the coordinate system. Zones are defined by combining these bodies using Boolean operations such as union, intersection, and subtraction. Regions are created by combining different zones. They represent portions of space with uniform properties and material composition, typically corresponding to actual components. Fig. A.1 illustrates examples of how zones and regions can be defined using simple bodies.

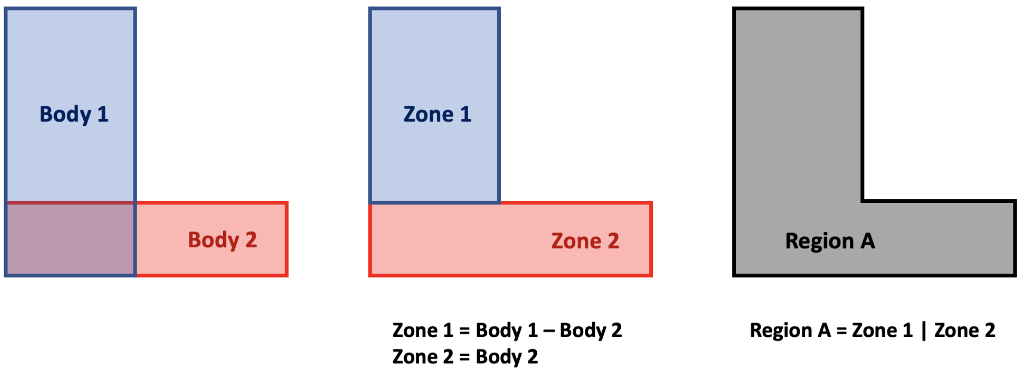

Figure A.1.: Illustration of the relationship between bodies, zones, and regions in FLUKA. Body 1 and Body 2 are geometric shapes used to define Zone 1 and Zone 2. Region A is then formed by the union of the zones, demonstrating how "complex" regions can be constructed from simple bodies through Boolean operations.

FLUKA further offers a lattice capability to describe repetitive geometric structures efficiently. This feature eliminates the need to repeatedly define the same bodies, zones, and regions in different positions, facilitating the implementation of symmetrical transformations such as rotation, translation, reflection, and their combinations between a prototype structure and its replicas. When the lattice option is activated, tracking occurs in two systems: the "real" system and the basic symmetry unit. The positions and directions of each particle are translated from their real values to their symmetric counterparts for physical transport within the prototype's regions and materials, and then translated back to the real-world coordinates.

A.2. Relevant Routines of the FLUKA code

This section briefly introduces user routines of FLUKA that are relevant for this thesis.

- FLUSCW allows the modification of scoring weights, enabling customised adjustments to the default behaviour of scoring estimators. It provides flexibility to apply user-specific criteria or corrections to the particle fluence, absorbed dose, or other quantities being scored.
- KASKAD is responsible for simulating the detailed cascade processes of hadron, muon, and heavy ion interactions. It handles the complex chain of particle collisions and decays, ensuring accurate modeling of particle transport and interaction phenomena within the simulation environment.
- USRSCO is the routine where the tracklength scoring is implemented.
- USRINI is responsible for initialising user-defined variables and parameters before the start of the simulation
- USROUT can be used to generate user-defined output alongside the default standard one

B. Locations of the Shielding Studies within ATLAS

This chapter provides illustrations of the components of the ATLAS experiment examined in Chapter 6 and shows their locations within the detector.

B.1. The Luminosity Detector and the Vacuum Equipment

The LUCID-2 detector of Run 3 is going to be upgraded and relocated. Prototypes of the new LUCID-3 detector, as well as the current LUCID-2 are depicted in Fig. B.1.

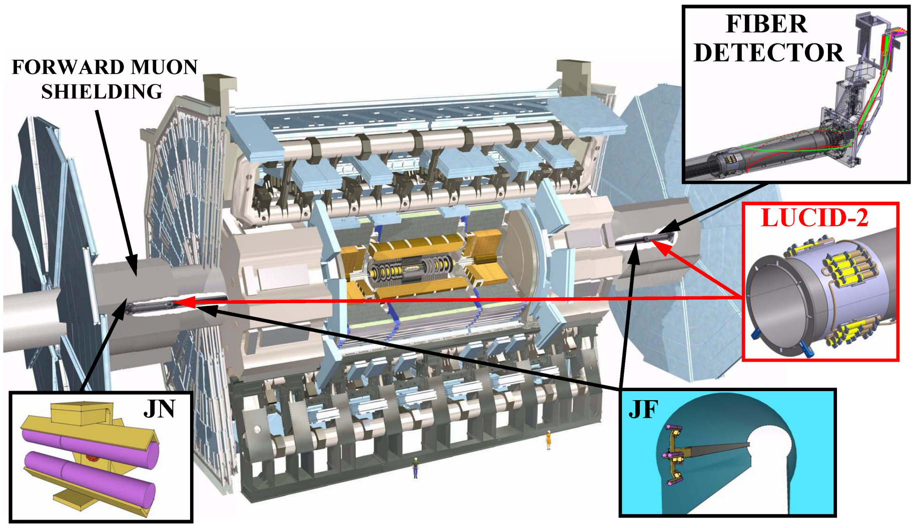

Figure B.1.: The location of the LUCID-2 detectors and the LUCID-3 prototype detectors in ATLAS. JF represents the LUCID-3 option attached to the forward muon shielding and Fiber Detector the option where it is attached to around the beampipe. From [92].

As decried in Section 2.2.8, the VAX equipment is going to be moved for the Phase 2 upgrade. The current Run 3 position as well as the future position are illustrated in Fig. B.2.

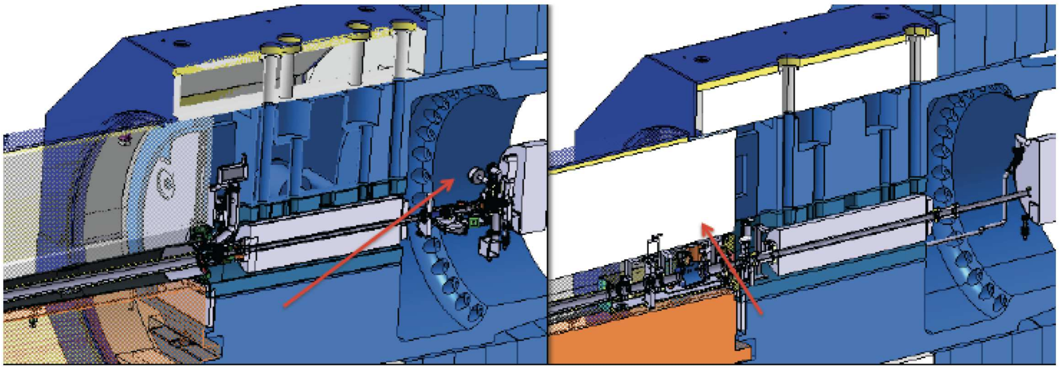

Figure B.2.: Illustration of the TAS collimator area where the LUCID-2 detector is installed.Red arrows point to the VAX equipment. On the left graph the current Run 3 position of the VAX equipment is shown. The right graph illustrates its position in the Phase 2 upgrade. Taken from [57].

B.2. Cooling Sensors

The cooling sensors are located on top of a water tank that sits on the ground floor of the cavern, depicted in Fig. B.3.The coordinates of the cooling sensors are $X = +1183\,\mathrm{cm}$, $Y = -933\,\mathrm{cm}$, $Z = +2081\,\mathrm{cm}$ and $X = -935\,\mathrm{cm}$, $Y = -933\,\mathrm{cm}$, $Z = -2365\,\mathrm{cm}$.

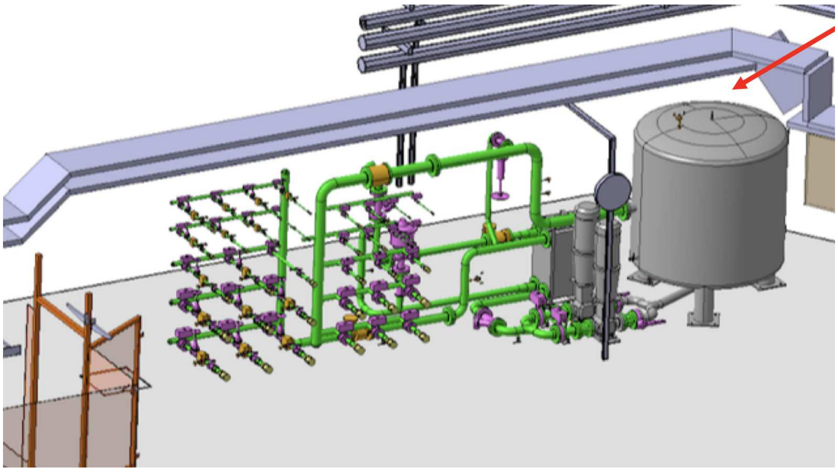

Figure B.3.: Illustration of the water tank and its nearby environment on the ground floor of the ATLAS cavern. On top of the tank the investigated sensor is located. The sensor is not visible, but its position is indicated by the red arrow.

Bibliography

[1] The ATLAS Collaboration. “The ATLAS Experiment at the CERN Large Hadron Collider”. In: Journal of Instrumentation 3.08 (2008), S08003–S08003. DOI: 10.1088/1748-0221/3/ 08/s08003.

[2] O. S. Bruening et al. LHC Design Report. CERN Yellow Reports:Monographs. Geneva: CERN, 2004. DOI: 10.5170/CERN-2004-003-V-1. URL: https://cds.cern.ch/record/782076.

[3] The ATLAS Collaboration. "Observation of a New Particle in the Search for the Standard Model Higgs Boson with the ATLAS Detector at the LHC", Phys. Lett. B, 716(1):1–29, 2012

[4] I. Dawson, S. Mallows. Simulation of radiation environments. CERN Yellow Reports:Monographs.Geneva: CERN, 2021. DOI: 10.23731/CYRM-2021-001.35

[5] Fluka Website, URL: https://fluka.cern, Accessed: 25.07.2023

[6] C. Ahdida et. al. New Capabilities of the FLUKA Multi-Purpose Code, Frontiers in Physics 9, 788253, 2022

[7] G. Battistoni et. al. Overview of the FLUKA code, Annals of Nuclear Energy 82, 10-18, 2015.

[8] G. Apollinari et al., “High-luminosity large hadron collider (HL-LHC): Technical design report v.0.1", Tech. Rep.,CERN-2017-007-M, Geneva, 2017.

[9] The ATLAS Collaboration. Technical Design Report for the ATLAS Inner Tracker Strip Detector. Tech. rep.Geneva: CERN, 2017. url: http://cds.cern.ch/record/2257755.

[10] The ATLAS Collaboration. LUCID-3: the upgrade of the ATLAS luminosity detector for High Luminosity LHC, Upgrade. Tech. rep. Geneva: CERN, 2022. url: https://cds.cern.ch/record/2837154/files/ATL-FWD-PROC-2022-007.pdf.

[11] A. Vasilesku, G. Lindstroem. Displacement Damage in Silicon, on-line compilation, Accessed: July 8, 2021 [Online]. Available: https://rd50.web.cern.ch/niel/

[12] G. P. Summers, E. A. Burke, P. Shapiro, R. J. Walters, and S. R. Messenger, “Damage correlations in semiconductors exposed to gamma, electron and proton radiations,” IEEE Transactions on Nuclear Science, Vol. 40,no. 6, pp. 1372–1379, 1993

[13] M. Huhtinen and P. Aarnio, “Pion induced displacement damage in Silicon devices,” Nucl. Instrum. Methods Phys. Res. A, Accel. Spectrom. Detect. Assoc. Equip., Vol. 335, no. 3, pp. 580–582, 1993

[14] P. J. Griffin, “SNL RML recommended. Dosimetry cross section com- pendium,” Sandia Nat. Lab., Livermore, CA, USA, Tech. Rep. SAND92- 0094, 1993

[15] A. Y. Konobeyev, Y. A. Korovin, and V. N. Sosnin, “Neutron displace- ment cross-sections for structural materials below 800 MeV,” J. Nucl. Mater., 1992, Vol. 186, no. 2, pp. 117–130

[16] Michael Moll. Displacement Damage in Silicon Detectors for High Energy Physics, IEEE Transactions on Nuclear Science, 2018, Vol. 65, No. 8

[17] A. Namenson, E. Wolicki, "Average Silicon Neutron Displacement KERMA Factor at 1 MeV*", IEEE Tranlsactions on Nuclear Science, Vol. NS-29, No. 1, 1982

[18] J. F. Ziegler, J. P. Biersack and U. Littmark.The stopping and range of ions in solids. Vol 1, Pergamon Press, New York, 1985.

[19] K. Potamianos. The upgraded Pixel detector and the commissioning of the Inner Detector tracking of the ATLAS experiment for Run-2 at the LargeHadron Collider. Tech. rep.Geneva: CERN, Aug. 2016. arXiv: 1608.07850.

[20] The ATLAS Collaboration, “Modelling radiation damage to pixel sensors in the ATLAS detector”, JINST 14 (2019) P06012, 2019.

[21] The CMS Collaboration. "Observation of a new boson at a mass of 125 GeV with the CMS experiment at the LHC", Phys. Lett. B, 716(1):30–61, 2012.

[22] The ATLAS Collaboration. "Measurements of the Higgs boson production and decay rates and coupling strengths using pp collision data at 7 and 8 TeV in the ATLAS experiment", Eur. Phys. J. C76, 2016

[23] W. Herr and B. Muratori. Concept of luminosity. 2006. doi: 10.5170/CERN- 2006-002.361. url: https://cds.cern.ch/record/941318.

[24] The ATLAS collaboration."Luminosity measurement at the HL-LHC with the ATLAS detector: Strategy and prototyping".ATLAS. Geneva: CERN,2023.URL:https://cds.cern.ch/record/2887999/

[25] Luminosity Public Results Run-2. Geneva, July 2019. URL: https://twiki.cern.ch/twiki/bin/ view/AtlasPublic/LuminosityPublicResultsRun2, Accessed: 09.08.2023

[26] “Linear accelerator 2”. In: (2012). url: https://cds.cern.ch/record/1997427.

[27] J. Vollaire et al. Linac4 design report. Ed. by Maurizio Vretenar. Vol. 6. CERN Yellow Reports: Monographs. Geneva: CERN, Sept. 2020. isbn: 978-92-9083-579-0, 978-92-9083-580-6. doi: 10.23731/CYRM-2020-006.

[28] "The Proton Synchrotron Booster". In: (2012). url: https : / / cds . cern . ch / record/1997372.

[29] "The Proton Synchrotron". In: (2012). url: https : / / cds . cern . ch / record / 1997189.

[30] "The Super Proton Synchrotron". In: (2012). url: https://cds.cern.ch/record/1997188.

[31] CERN Website, URL: https://home.cern/science, Accessed: 09.08.2023

[32] Esma Mobs. "The CERN accelerator complex - 2019. Complexe des accélérateurs du CERN - 2019". General Photo. url: https://cds.cern.ch/record/2684277.

[33] The ALICE Collaboration et al. "The ALICE experiment at the CERN LHC". In: Journal of Instrumentation 3.08 (2008), S08002–S08002. doi: 10.1088/1748-0221/3/08/s08002. url: https://doi.org/10.1088/1748-0221/3/08/s08002.

[34] The CMS Collaboration. "The CMS experiment at the CERN LHC". In: Journal of Instrumentation 3.08 (2008), S08004–S08004. DOI: 10.1088/1748-0221/3/08/s08004.

[35] The LHCb Collaboration. "The LHCb Detector at the LHC". In: Journal of Instrumentation 3.08 (Aug. 2008), S08005–S08005. DOI: 10.1088/1748-0221/3/08/s08005.

[36] "High-Luminosity Large Hadron Collider (HL-LHC): Technical Design Report V. 0.1". In: 4/2017 (2017). Ed. by G. Apollinari et al. doi: 10.23731/CYRM-2017-004.

[37] The ATLAS Collaboration. ATLAS inner detector: Technical Design Report, 1. Technical design report. ATLAS. Geneva: CERN, 1997. URL: https://cds.cern.ch/record/331063.

[38] E. Stanecka. The ATLAS Inner Detector operation, data quality and tracking performance. 2013. arXiv: 1303.3630 [physics.ins-det].

[39] M. Thomson. Modern particle physics. New York: Cambridge University Press, 2013. ISBN:978-1-107-03426-6

[40] The ATLAS Collaboration. ATLAS magnet system: Technical Design Report, 1. Technical design report. Geneva: CERN, 1997. URL: https://cds.cern.ch/record/338080.

[41] Veness, R. The ATLAS beam vacuum system. Particle Accelerator Conference 2009, Vancouver, Canada, 2009, pp.MO6RFP009

[42] The ATLAS Collaboration. The Silicon Microstrip Sensors of the ATLAS SemiConductor Tracker. Tech. rep. Geneva: CERN,Mar. 2007. DOI: 10.1016/j.nima.2007.04.157.

[43] E Abat et al. "The ATLAS Transition Radiation Tracker (TRT) proportional drift tube: design and performance". In: JINST 3 (2008), P02013. doi: 10.1088/1748-0221/3/02/P02013. url: https://cds.cern.ch/record/1094549.

[44] The ATLAS Collaboration.TrackReconstructionPerformance of theATLAS InnerDetector at $\sqrt{s} = 13$ TeV. ATL-PHYS-PUB-2015-018. 2015. URL: https://cds.cern.ch/record/2037683.

[45] M. Capeans et al. ATLAS Insertable B-Layer Technical Design Report. Tech. rep. Sept. 2010. URL: https://cds.cern.ch/record/1291633.

[46] The ATLAS Collaboration. "Operation and performanceof the ATLAS semiconductor tracker". In: Journal of Instrumentation 9.08 (Aug. 2014), P08009–P08009. ISSN: 1748-0221. DOI: 10.1088/1748-0221/9/08/p08009.

[47] The ATLAS Collaboration. "ATLAS liquid argon calorimeter: Technical design report". In: (Dec. 1996). url: https://inspirehep.net/literature/432394

[48] The ATLAS Collaboration. ATLAS tile calorimeter: Technical Design Report. Technical design report. ATLAS. Geneva: CERN, 1996. url: https://cds.cern.ch/record/331062.

[49] N Ilic. "Performance of the ATLAS Liquid Argon Calorimeter after three years of LHC operation and plans for a future upgrade". In: Journal of Instrumentation 9.03 (2014), pp. C03049–C03049. doi: 10.1088/1748-0221/9/03/c03049. url: https://doi.org/10.1088/1748-0221/9/03/c03049.

[50] Joao Pequenao. "Computer Generated image of the ATLAS calorimeter". 2008. url: https://cds.cern.ch/record/1095927.

[51] B. R. Martin. Nuclear and Particle Physics. John Wiley and Sons, Ltd, 2006, ISBN: 0-470-01999-9 (p. 29).

[52] R.L. Workman et al. (Particle Data Group), Prog. Theor. Exp. Phys. 2022, 083C01

[53] The ATLAS Collaboration. "ATLAS muon spectrometer: Technical design report". In: (June 1997).

[54] M. zur Nedden. "The LHC Run 2 ATLAS trigger system: design, performance and plans". In: Journal of Instrumentation 12.03 (Mar. 2017), pp. C03024–C03024. DOI: 10.1088/1748-0221/12/03/c03024.

[55] The ATLAS Collaboration. Expected tracking and related performance with the updated ATLAS Inner Tracker layout at the High-Luminosity LHC. Tech. rep. Geneva: CERN. url: https://atlas.web.cern.ch/Atlas/GROUPS/PHYSICS/PUBNOTES/ATL-PHYS-PUB-2021- 024/.

[56] The ATLAS Collaboration. Technical Design Report: A High-Granularity Timing

Detector for the ATLAS Phase-II Upgrade. Tech. rep. Geneva: CERN, 2020. url: https://cds.cern.ch/record/2719855.

[57] The ATLAS Collaboration, ATLAS Phase-II Upgrade Scoping Document, CERN-LHCC-G-166, https://cds.cern.ch/record/2055248/files/LHCC-G-166.pdf

[58] W. R. Leo. Techniques for nuclear and particle physics experiments. Heidelberg: Springer Berlin,1994. ISBN: 978-3-540-57280-0

[59] International Atomic Energy Agency, Website, https://www-nds.iaea.org/exfor/endf.htm, Accessed: 22.07.2023

[60] G. Aad et al., Beam-induced backgrounds measured in the ATLAS detector during local gas injection into the LHC beam vacuum, JINST 19 P06014, 2024

[61] R. Bruce et al., Collimation-induced experimental background studies at the CERN Large Hadron Collider, Phys. Rev. Accel. Beams 22, 021004, 2019

[62] J. Allison et al., Recent Developments in Geant4, Nucl. Instrum. Meth. A 835 186-225, 2016

[63] C. Bierlich et al., A comprehensive guide to the physics and usage of PYTHIA 8.3, SciPost Phys. Codebases 8, 2022

[64] T.Pierog et al.,EPOS LHC: Test of collective hadronization with data measured at the CERN Large Hadron Collider. Physical Review C, 92(3), 034906. https://doi.org/10.1103/PhysRevC.92.034906, 2015

[65] The ATLAS Collaboration, Software and computing for Run 3 of the ATLAS experiment at the LHC, arXiv:2404.06335,2024

[66] P. Skands, S. Carrazza and J. Rojo, Eur.Phys.J. C74 (2014) 8, 3024 [arXiv:1404.5630 [hep-ph]]

[67] S. Navin, Diffraction in PYTHIA, arXiv:1005.3894, 2010

[68] M. Deile et al., Diffraction and Total Cross-Section at the Tevetron and the LHC, arXiv:hep-ex/0602021v1, 2006

[69] The ATLAS Collaboration.The Pythia 8 A3 tune description of ATLAS minimum bias and inelastic measurements incorporating the Donnachie-Landshoff diffractive model. ATL-PHYS-PUB-2016-017. 2016. URL: https://cds.cern.ch/record/2206965/files/ATL-PHYS-PUB-2016-017.pdf

[70] V.D. Barger, R.J.N. Phillips, Collider Physics. Westview Press, 1996

[71] A. Capella et al., Phys. Rep 236,1994, 225, doi:10.1016/0370-1573(94)90064-7.

[72] A. Ferrari and P.R. Sala, The physics of high energy reactions, Proc. Workshop on Nuclear Reaction Data and Nuclear Reactors Physics, Design and Safety, Eds. A. Gandini, G. Reffo. World Scientific, Singapore, 1998, pp. 424–532, doi 10.1142/9789814530385, ATL-PHYS-97-113.

[73] A. Ferrari, P.R. Sala, A new model for hadronic interactions at intermediate energies for the FLUKA code, Proc. MC93 Int. Conf. on Monte Carlo Simulation in High Energy and Nuclear Physics Eds. P. Dragovitsch et. al. (World Scientific, Singapore 1994), pp. 277-288,doi:10.1142/9789814534833.

[74] A. Fassò et. al., FLUKA: performances and applications in the intermediate energy range, Proc.OECD / NEA Specialists' Meeting on Shielding Aspects of Accelerator, Targets and Irradiation Facilities, (OECD, Paris 1995), pp. 287-304.

[75] M. Huhtinen, The Radiation Environment at the CMS Experiment at the LHC, CERN, 1996

[76] International Atomic Energy Agency, Website, URL: https://www-nds.iaea.org/geant4, Accessed: 28.07.2023

[77] F.Hartmann. Evolution of Silicon Sensor Technology in Particle Physics. Springer Cham, 2017. ISBN: 978-3-319-64436-3

[78] Edward Petersen, Single event effects in aerospace, Wiley-IEEE Press, 2011.

[79] M. Huhtinen, F. Faccio, Computational method to estimate single event upset rates in an accelerator environment, Nucl.Instrum.Meth.A 450 (2000) 155-172, DOI:10.1016/S0168-9002(00)00155-8

[80] M.Cecchetto et al., Thermal Neutron-Induced SEUs in the LHC Accelerator Environment, IEEE TRANSACTIONS ON NUCLEAR SCIENCE, VOL. 67, NO. 7, 2020

[81] The ATLAS Collaboration. Interactive web pages for radiation environment exploration of ATLAS. ATL-SOFT-PUB-2020-003. Geneva: CERN, 2020

[82] J.R. Srour, C.J. Marshall, P.W. Marshall. Review of Displacement Damage Effects in Silicon Devices, IEEE Transactions on Nuclear Science, 2003, Vol. 50, No. 3, 653

[83] P. A. Aarnio et al., Damage observed in silicon diodes after low energy pion irradiation, Nucl. Instr. and Meth. A360, 521–531, 1995.

[84] S. J. Bates et al., Pion-induced damage in silicon detectors, Nucl. Instr. and Meth. A379, 116–123, 1996.

[85] M. Moll, E. Fretwurst, M. Kuhnke and G. Lindtroem, Relation between microscopic defects and changes in silicon detector properties after hadron irradiation,Nucl. Instr. and Meth. B186, 100-110, 2002.

[86] M.T. Robinson, "Basic Physics of Radiaiton Damage Production", Journal of Nuclear Materials 216 (1994)1-28, Oak Ridge National Laboratory, 1994

[87] E. Byckling,K. Kajantie, Particle Kinematics, John Wiley and Sons,1973

[88] P. Gombh. "Handbuch der Physik", ed. S. Fliigge, vol.XXXVI (Springer, Berlin, 1956) p. 109.

[89] J. Lindhard, V. Nielsen, V, and M. Scharff. Approximation Method in Classical Scattering by Screened Coulomb Fields.Mat.-Fys. Medd., 36: 31p(1968), Denmark

[90] V. Verbinski et al., "Simultaneous Neutron Spectrum and Transistor-Damage Measurements in Diverse Neutron Fields: Validity of DSi(En)," NRL Memorandum Report 3929, Naval Research Laboratory,Washington, D. C., 1979

[91] V. V. Verbinski et al., Simultaneous Neutron Spectrum and Transistor-Damage Measurements in Diverse Neutron Fields: Validity of DSi(En), NRL Memorandum Report 3929, Naval Research Laboratory, Washington, D. C., 1979.

[92] The ATLAS Collaboration, Photos and drawings of the LUCID-3 detector, https://lucid3.web.cern.ch/

List of Figures

List of Tables